



Dalton
Transactions

**The Chemical and Physical Properties of Tetravalent
Lanthanides: Pr, Nd, Tb, and Dy**

Journal:	<i>Dalton Transactions</i>
Manuscript ID	DT-PER-04-2020-001400.R1
Article Type:	Perspective
Date Submitted by the Author:	19-May-2020
Complete List of Authors:	Gompa, Thaige; Georgia Institute of Technology, School of Chemistry and Biochemistry Ramanathan, Arun; Georgia Institute of Technology, School of Chemistry and Biochemistry Rice, Natalie; Georgia Institute of Technology, School of Chemistry and Biochemistry La Pierre, Henry; Georgia Institute of Technology, School of Chemistry and Biochemistry

SCHOLARONE™
Manuscripts

ARTICLE

The Chemical and Physical Properties of Tetravalent Lanthanides: Pr, Nd, Tb, and Dy

Thaige P. Gomba,^{a†} Arun Ramanathan,^{a†} Natalie T. Rice,^{a†} and Henry S. La Pierre^{a,b*}

Received 00th January 20xx,
Accepted 00th January 20xx

DOI: 10.1039/x0xx00000x

The fundamental redox chemistry and valence electronic structure of the lanthanides in molecular complexes and extended solids continues to be a fertile area of research. The contemporary understanding of the accessible oxidation states of the lanthanide elements and the variability in their electronic structure is the result of several paradigm shifts. While the lanthanide elements have already found widespread use in technical and consumer applications, the continued reevaluation of basic redox properties is a central chemical concern to establish a more complete description of periodic properties. This fundamental understanding of valence electronic structure as it is derived from oxidation state and coordination environment is essential for the continued development of lanthanides in quantum information science and quantum materials research. This review presents the chemical and physical properties of tetravalent lanthanide ions in extended solids and molecules with a focus on the elements apart from cerium: praseodymium, neodymium, terbium, and dysprosium.

Introduction

The understanding of lanthanide oxidation states, valence electronic structure, and redox chemistry in condensed phases (molecular and extended solids) has been through waves of reconstruction (Figure 1). These paradigm shifts began when the lanthanides were first available in pure form and in significant quantities starting in the 1950's with Frank Spending's development of ion exchange purification methodologies.¹⁻⁹ Prior to this innovation, Klemm established an empirical model of systematic valences that rationalized the aqueous stability of trivalent lanthanides across the series along with exceptions for divalent Sm, Eu, and Yb ions and tetravalent Ce ions in solution.¹⁰ This framework also contended with the observed stability of tetravalent Pr and Tb in the solid state. The accessibility of non-trivalent oxidation states was rationalized on achieving (or approximately achieving) empty, filled, or half-filled shells (e.g. $4f^0$, $4f^{14}$, $4f^7$).

The emergence and rationalization of lanthanide oxidation states outside of Klemm's model can be traced to the work of John D. Corbett on solid-state lanthanide halides.¹¹ These studies guided the field from Klemm's empirically derived model of systematic valences of the lanthanides, to the classification of divalent lanthanide halides in insulating phases, $(R^{2+})(X)_2$, (R = rare-earth and X = halide) and semi-metallic phases $(R^{3+e^-})(X)_2$. The latter phases were proposed to have an electron delocalized in the conduction band. These dichotomous valence electronic structure models for divalent

lanthanides were refined through both the synthesis and characterization of solid-state and molecular systems to the contemporary nomenclature: insulating $4f^{n+1}5d^0$ and semi-metallic $4f^n5d^1$. This current model was built from the close relationship between solid-state and molecular practitioners.^{11, 12} In contrast to molecular transition metal chemistry, where biological inspiration has historically driven the field, molecular lanthanide redox chemistry has built on the materials, techniques, and analysis established for solid-state systems. With the advent of bioinorganic lanthanide chemistry, this synergy is evolving.¹³⁻²⁰ However, there are significant signposts in the solid-state literature to guide the further development of molecular lanthanide redox chemistry.

This intellectual approach has precedent. Corbett and Meyer mapped the phases of accessible divalent lanthanide halide and oxide-halide materials.²¹⁻³² The divalent lanthanide phases have yielded unique magnetic properties.³³ The identity of the products of these reactions were often governed by the equilibrium $M + MX_3 \rightleftharpoons 2MX_2$ which defined two synthetic targets for the molecular synthetic community: isolation of zero-valent and divalent complexes. Cloke and co-workers established molecular zero-valent complexes of the rare-earth elements (Sc, Y, and Ln = lanthanide)³⁴⁻³⁹ and established the framework for the analysis of mixed-valent magnetism (ground state population of the *f* and *d* shell).³⁶ Bocharov and co-workers employed the divalent iodide extended solids of Tm, Nd, and Dy to open the field of non-traditional divalent lanthanide complexes with the isolation of their ethereal adducts.⁴⁰⁻⁴³ These leads led to the consideration of organometallic divalent lanthanide complexes. Lappert and Evans built a complete series of lanthanide divalent anions, and, concurrently, a wide range of structural types for anionic divalent lanthanides and actinides were isolated.⁴⁴⁻⁷³ These

^a Department of Chemistry and Biochemistry, Georgia Institute of Technology, Atlanta, Georgia 30332-0400, USA. E-mail: hsl@gatech.edu

^b Nuclear and Radiological Engineering Program, Georgia Institute of Technology, Atlanta, Georgia 30332-0400, USA.

^c † These authors contributed equally.

ARTICLE

La	Ce	Pr	Nd	Pm	Sm	Eu	Gd	Tb	Dy	Ho	Er	Tm	Yb	Lu
m	m	m	m		m	m	m	m	m	m	m	m	m	m
s	s,m	s,m	s,m		s,m	s,m	s,m	s,m	s,m	s,m	s,m	s,m	s,m	s,m
s,m	s,m	s,m	s,m		s,m	s,m	s,m	s,m	s,m	s,m	s,m	s,m	s,m	s,m
s,m	s,m,g	s,m	s,g		s,m	s,m	s,m	s,m,g	s,g	s,m	s,m	s,m	s,m	s,m
0+	1+	2+	3+	4+	5+									

Figure 1. Known oxidation states for 4f elements and corresponding phase of isolation/identification: molecular (m), extended solid (s), and gas-phase (g).

methodological developments have even led to the isolation of neutral, non-traditional divalent lanthanide and actinide complexes, with some electrochemical evidence for a monovalent uranium complex.^{74, 75} The latter possibility is foreshadowed by the isolation of monovalent [LaI] and a monovalent Sc complex.^{76, 77} These results portend the development of lanthanide and actinide monovalent molecular chemistry.

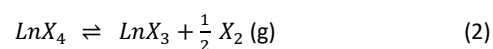
This perspective summarizes the thermochemistry, descriptive chemistry, spectroscopy (optical, core-level, and EPR) and physical properties (magnetism) of tetravalent lanthanides in extended phases, gas phase, solution, and as isolable molecular complexes. Where appropriate the chemistry of tetravalent Ce is included for the direct reference of the reader. However, several excellent reviews have covered high-valent Ce from the perspective of redox chemistry⁷⁸ and the isolation of metal-ligand multiple bond complexes.⁷⁹ This perspective focuses on the chemistry and physical properties of tetravalent Pr, Nd, Tb, and Dy.

2. Thermochemistry of Ln⁴⁺ in Binary and Ternary Phases

The last definitive review of lanthanide thermochemistry, published in 1976, focused primarily on trivalent and divalent lanthanide chemistry and provided a broad summary of the accessible tetravalent lanthanide phases established at the time.⁸⁰ Studies on the stability of tetravalent lanthanide ions in condensed phases were extended by Bratsch and Silber for binary systems employing an ionic model established to determine the enthalpy of formation of trivalent lanthanides.⁸¹ The ionic model involves the Born-Haber cycle as depicted in Figure 2. Based on the Born-Haber cycle, the enthalpy of formation of binary tetravalent lanthanides is given by Equation 1:

$$\Delta H_f^0 (Ln^{4+}X^-) = \Delta H_f^0 (Ln^{4+}) + \Delta H_f^0 (X_g^{1-}) - \Delta H_{lattice}^0 (LnX) \quad (1)$$

where, $\Delta H_f^0 (Ln_g^{4+})$ involves the sum of ionization energy and sublimation energy and $\Delta H_{lattice}^0 (LnX)$ is written as a function of ionic radii of the lanthanide and the ligand. In order to determine the stability of the binary tetravalent lanthanides, their enthalpies of formation are compared to the enthalpies of formation of the corresponding binary trivalent lanthanides via a decomposition reaction as shown below in Equation 2:



From this analysis, if the $\Delta H_{decomposition}^0$ is positive, the tetravalent lanthanide phase is stable with respect to decomposition to the trivalent phase. However, if it is negative, the tetravalent phase is expected to decompose to the binary trivalent lanthanide. Based on these calculations, CeO₂, CeF₄, PrO₂, PrF₄, TbO₂ and TbF₄ are stable. However, it should be noted here that the Ce⁴⁺ based binary compounds are significantly more stable than the corresponding Pr⁴⁺ and Tb⁴⁺ analogs. The order of stability of the binary tetravalent

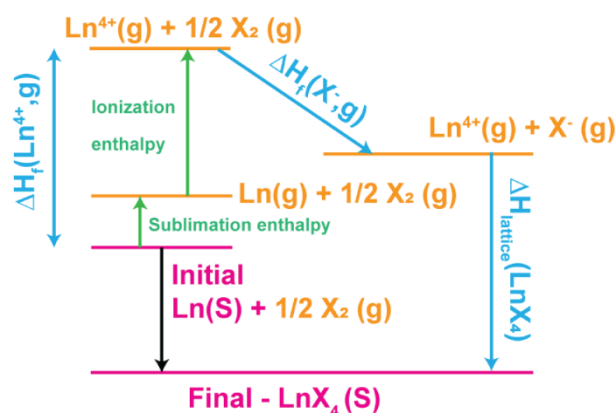


Figure 2. Born-Haber cycle for calculating the standard molar enthalpy of formation of binary tetravalent lanthanides as described in equation 1. Figure adapted from reference 81.

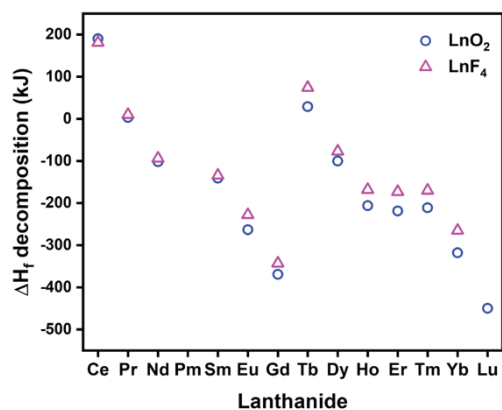


Figure 3. The enthalpy of decomposition of binary tetraivalent fluorides (LnF_4) represented by pink triangles and binary tetraivalent oxides (LnO_2) represented by blue circles plotted against corresponding lanthanide. Modified from reference 81.

lanthanides based on the predicted enthalpy of decomposition is CeO_2 (190 kJmol^{-1}) > CeF_4 (181 kJmol^{-1}) > TbF_4 (74 kJmol^{-1}) > TbO_2 (29 kJmol^{-1}) > PrF_4 (10 kJmol^{-1}) > PrO_2 (3 kJmol^{-1}) and has been plotted in Figure 3. Even though binary PrF_4 and PrO_2 are relatively less stable than their Ce or Tb analogs, Pr^{4+} is more stable in ternary fluoride and oxide lattices such as Na_2PrF_6 and Na_2PrO_3 , than Ce or Tb (*vide infra*). This increased stability in the ternary phase indicates that lattice contributions can compensate and stabilize the tetraivalent lanthanides in extended solids.

The enthalpy of formation of CeO_2 was determined experimentally using solution calorimetry by Holley and Huber in 1953⁸² and 1970⁸³ and by Kuznetsov in 1960.⁸⁴ Electromotive force (emf) measurements to determine the enthalpy of formation of CeO_2 were reported by Kuznetsov in 1961.⁸⁵ The average value of enthalpy of formation of CeO_2 based on these different techniques was found to be $-1090.4 \text{ kJmol}^{-1}$.⁸⁶ The enthalpy of formation of PrO_2 was studied using solution calorimetry by Eyring and Cunningham in 1957 and by Gramsch and Morss in 1995 and the corresponding values are $-949.3 \text{ kJ mol}^{-1}$ and $-959.1 \text{ kJmol}^{-1}$, respectively.^{87, 88, 89} The slight discrepancy is probably due to differences in substoichiometry of oxygen in PrO_{2-x} . The enthalpy of formation of TbO_2 was determined using solution calorimetry by Fitzgibbon and Holley⁹⁰ and by Stubblefield and Eyring.⁹¹ Since the maximum oxygen content achieved in TbO_x has been $x = 1.95$, the enthalpy of formation for TbO_2 was extrapolated by determining the enthalpy of formation for different non-stoichiometric Tb oxides. Based on the extrapolation, the enthalpy of formation for TbO_2 was found to be $-971.52 \text{ kJmol}^{-1}$.⁹⁰ These experimental values follow the same trend as the calculated values with stability decreasing in the order $\text{CeO}_2 > \text{TbO}_2 > \text{PrO}_2$.

Numerous studies have been carried out to determine the thermodynamic stability of tetraivalent lanthanide binary fluorides. The thermodynamic stability of the binary fluorides is calculated via the decomposition reaction in Equation 2. Gibson and Haire determined the thermodynamic stability of CeF_4 and

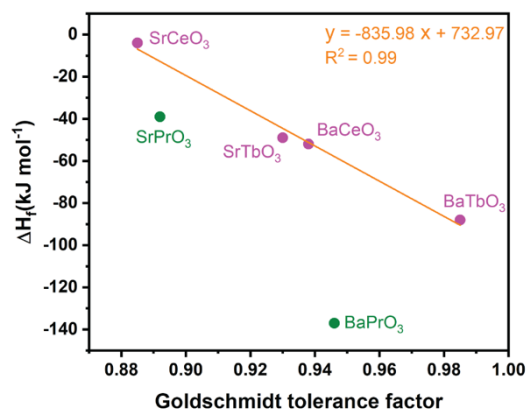


Figure 4. Standard molar enthalpy (equation 3) for the formation of $\text{M}'\text{LnO}_3$ ($\text{M}' = \text{Sr, Ba}$; $\text{Ln} = \text{Ce, Pr, Tb}$) perovskites plotted against Goldschmidt tolerance factor. Figure adapted from reference 89.

TbF_4 with high temperature decomposition studies in a Knudsen cell using a mass spectrometer to identify the decomposition products.⁹² The decomposition enthalpies thus determined for CeF_4 (242.6 kJmol^{-1}) and TbF_4 (83.58 kJmol^{-1})⁹³ are greater than the values predicted by Bratsch and Silber.⁸¹ The difficulty in preparation procedure of PrF_4 with decomposition around 363 K is in accordance with a small predicted enthalpy of decomposition by Bratsch and Silber.⁸¹

This empirical extrapolation of the predictions for binary tetraivalent lanthanide phases is supported by solution calorimetry of tetraivalent lanthanides in ternary oxide-based lattices of the type $\text{M}'\text{LnO}_3$ ($\text{M}' = \text{Sr, Ba}$; $\text{Ln} = \text{Ce, Pr, Tb}$). Deviation from the ideal cubic structure in perovskites is quantified using the Goldschmidt tolerance factor (t).⁹⁴ When $t < 1$, meaning a greater distortion, the enthalpy of formation of the perovskite becomes less negative indicative of a decrease in stability of the perovskite. With an 0.5 \AA size difference between Ba^{2+} and Pr^{4+} , BaPrO_3 is a highly distorted perovskite. However, the formation of BaPrO_3 has been found to be exothermic indicating that BaPrO_3 is unusually stable. Hence, studies were carried out using solution calorimetry to understand the thermodynamics of formation of SrPrO_3 and BaPrO_3 , and extended to the Ce and Tb analogs.⁸⁹

The solution calorimetry was performed by dissolving binary and ternary oxides of Pr^{4+} in suitable solvents. The molar enthalpy of formation of the perovskite oxide was calculated from the enthalpy of formation of $\text{M}'\text{O}$ ($\text{M}' = \text{Ba, Sr}$) and LnO_2 ($\text{Ln} = \text{Pr, Ce, Tb}$) for the following reaction:



A simple linear correlation between tolerance factor, t , and the molar enthalpy of formation of SrPrO_3 (-39 kJmol^{-1}), BaPrO_3 (-137 kJmol^{-1}), SrCeO_3 (-4 kJmol^{-1}), BaCeO_3 (-52 kJmol^{-1}), SrTbO_3 (-49 kJmol^{-1}), BaTbO_3 (-88 kJmol^{-1}) was derived as shown in Figure 4.⁸⁹ The deviation of SrPrO_3 and BaPrO_3 from a correlation to the

ARTICLE

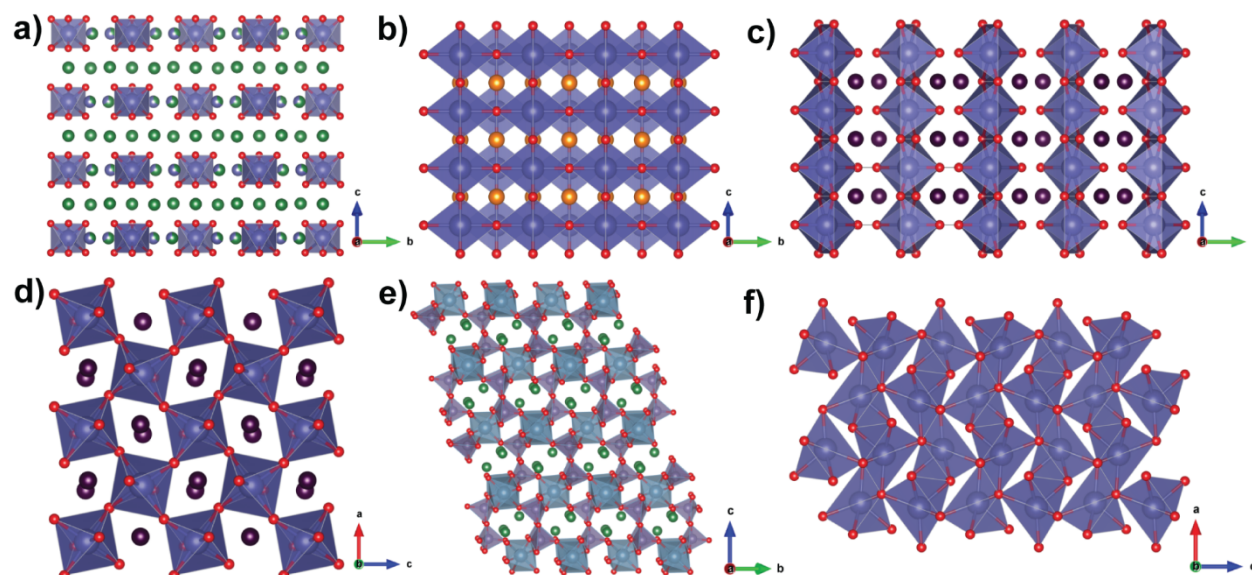


Figure 5. Structural representation of Na_2PrO_3 viewed along a direction to show the layered structure with layers stacked along the c direction and Na atoms between the layers.⁹⁵ b) Structural representation of Li_2PrO_3 viewed along a direction to show the connectivity between Pr octahedrons along b direction.⁹⁵ c) Structural representation of Sr_2PrO_4 viewed along a direction to show the layered structure with layers stacked along b direction and Sr atoms between layers.⁹⁶ d) Structural representation of SrPrO_3 viewed along b direction to show the cooperative tilting of Pr octahedrons.⁹⁷ e) Crystal structure of $\text{K}_2\text{TbGe}_2\text{O}_7$ viewed along a direction.⁹⁸ f) Structural representation of PrO_2 viewed along b direction.⁹⁹ Pr atoms are represented by dark blue octahedra in a, b, c, d and f, Tb (light blue octahedra in e), O (red), Na (green in a), Li (orange in b), K (light green in e), Sr (dark purple in c and d) and Ge (light purple in e). Figures generated using Vesta software using CIF files from ICSD.^{100,101}

tolerance factor suggests that another phenomenon is contributing to the lattice stabilization. It should be noted that SrPrO_3 deviates less from the ideal linear correlation when compared to BaPrO_3 . This difference could be attributed to the more distorted structure of the SrPrO_3 perovskite.

Other closed shell and open shell systems in AMO₃ perovskites with $\text{Th}^{4+}(5f^06d^0)$, $\text{Tb}^{4+}(4f^7)$, $\text{Pu}^{4+}(5f^4)$, $\text{Am}^{4+}(5f^2)$, and $\text{Cm}^{4+}(5f^6)$ fit the linear correlation with the tolerance factor.⁸⁹ Hence the unusual thermodynamic stability of SrPrO_3 and BaPrO_3 might not be from a structural origin but rather be due to the electronic structure of these perovskites, and multiple theories have been proposed.⁸⁹ The change from an eight-coordinate environment in PrO_2 for Pr^{4+} to a six coordinate in APrO_3 might be a driving force for the unusual stability.⁸⁹ It has also been proposed that an increase in covalency of $\text{Pr}^{4+}-\text{O}^{2-}$ bonds resulting in charge delocalization between cation $4f$ and anion $2p$ orbitals might offer extra stability to these perovskites.⁸⁹ There is some indirect support for this analysis from O K-edge XAS studies of the binary oxides, CeO_2 , PrO_2 , and TbO_2 (*vide infra*).¹⁰²

The enthalpy of formation of ALnO_3 ($A = \text{Sr}, \text{Ba}$; $\text{Ln} = \text{Ce}^{4+}, \text{Pr}^{4+}$, and Tb^{4+}) perovskites has been examined by a number of experimentalists. Ushakov and Navrotsky performed oxide-melt drop solution calorimetry to calculate the enthalpy of formation of BaLnO_3 ($\text{Ln} = \text{Ce}, \text{Pr}$) perovskite oxides based on the

reaction between BaO and PrO_2 in 2002.¹⁰³ The enthalpy of formation of BaPrO_3 was calculated to be -70 kJmol^{-1} , much less than the value calculated by Gramsch and Morss (-137 kJmol^{-1}).⁸⁹ However, this value is in agreement with the linear correlation between the Goldschmidt tolerance factor and enthalpy of formation. The enthalpy of formation of BaCeO_3 was calculated to be -51 kJmol^{-1} (oxide-melt solution calorimetry) in agreement with the value reported by Gramsch and Morss⁸⁹ (-52 kJmol^{-1}), Huntelaar¹⁰⁴ (-53.2 kJmol^{-1}), Fuger and Haire¹⁰⁵ (-52 kJmol^{-1}) using solution calorimetry. The enthalpy of formation of BaCeO_3 was also determined using mass spectrometry by Matsui (-74 kJmol^{-1}) and significantly deviated from the previous studies.¹⁰⁶ This discrepancy was attributed to the difference in sequence of calculation of enthalpy of formation. The enthalpy of formation of SrCeO_3 was also determined using solution calorimetry by Gramsch and Morss⁸⁹ (-4 kJmol^{-1}), in excellent agreement with the values provided by Huntelaar¹⁰⁴ (-7 kJmol^{-1}) and Fuger and Haire¹⁰⁵ (-5.6 kJmol^{-1}). The significantly increased thermodynamic stability of BaCeO_3 in comparison to SrCeO_3 can be attributed to the Goldschmidt tolerance factor since BaCeO_3 is much closer to the ideal perovskite structure than SrCeO_3 .⁸⁹ A similar analysis can be applied to Pr^{4+} compounds where BaPrO_3 is significantly more stable than SrPrO_3 . The enthalpies of formation of SrTbO_3 (-49 kJmol^{-1}) and

BaTbO₃ (-89 kJmol⁻¹) were determined using solution calorimetry by Fuger and Haire and follow a similar ordering.¹⁰⁵

Based on the thermochemistry of ternary tetravalent lanthanide oxides, Tb⁴⁺ and Ce⁴⁺ perovskites fall in line with the linear relationship between enthalpy of formation and Goldschmidt tolerance factor.⁹⁴ Pr⁴⁺ perovskites show a greater degree of stabilization with BaPrO₃ being the most stable ternary tetravalent oxide followed by SrPrO₃ (from solution calorimetry) and with SrCeO₃ the least stable.⁸⁹ This observed stability is in contrast with the thermochemistry of binary tetravalent lanthanide oxides and fluorides where Pr⁴⁺ is the least stable tetravalent lanthanide. Based on the enthalpy of formation of Pr⁴⁺ based perovskites and the enthalpy of decomposition of binary oxides/fluorides, it is evident that, strong lattice contributions are required to stabilize Pr⁴⁺. However, electronic stabilization might also play a key role in stabilizing Pr⁴⁺ (*vide infra*). Hence, the stability of Pr⁴⁺ materials may be driven by both the lattice and the electronic structure facilitated by strong coupling between the phonon density of states and electronic density of states.¹⁰⁷

3. Solid-State Ln⁴⁺ Chemistry

With the background solid-state thermochemistry of binary and ternary tetravalent lanthanide systems established, this section reviews the synthesis and physical properties of Pr⁴⁺, Tb⁴⁺, Nd⁴⁺, and Dy⁴⁺ in pure oxidation state and doped phases. These systems span binary and ternary oxides and fluorides and the recent preparation of more complex polynary phases. The materials included here are from an exhaustive ICSD search and include our best efforts to include unindexed early reports.¹⁰¹ The narrative, however, is focused on recent studies and modern characterization methods. The commercially available, mixed-valent oxides of Pr and Tb (nominally Pr₆O₁₁ and Tb₄O₇) are not included, since these materials have been described in detail previously.¹⁰⁸⁻¹¹² In general, mixed oxidation state materials are excluded from this discussion. All known Pr⁴⁺ and Tb⁴⁺ compounds in the solid state are summarized in Table 1 and Table 2, respectively.

Synthesis of LnF₄ (Ln = Ce, Pr, Tb). Ce, Pr, and Tb can be stabilized in tetravalent oxidation states as binary oxides and fluorides – LnO₂ and LnF₄. The fluorides can be prepared by a variety of methods: in 1934 Klemm and Henkel synthesized CeF₄ by reaction of anhydrous CeCl₃ with F₂ at room temperature.¹¹³ In 1940, Wartenberg synthesized CeF₄ by reaction of CeF₃ with F₂ gas in the temperature range 623-773 K.¹¹⁴ Longer times are required if F₂ gas is diluted with N₂/Ar. While TbF₄ is less stable than CeF₄, the synthetic conditions for the preparation of TbF₄ are similar to those for CeF₄. TbF₄ can also be prepared by treating TbF₃ or TbCl₃ with F₂ gas around 623 K.¹¹⁵ Kiselew *et al.*, reported an alternative route to the synthesis of phase pure TbF₄ and CeF₄ using XeF_n (n = 2, 4, 6) or KrF₂ as fluorinating agents.¹¹⁶ These reactions took place with TbF₃ or CeF₃ as starting materials in a nickel or Monel container. However, such a high temperature route is not feasible for the synthesis of PrF₄, since it decomposes at 363 K to PrF₃ and F₂,¹¹⁷ and is the

least stable tetrafluoride of the lanthanides. Klemm and Henkel in 1934 reported that the reaction between PrCl₃ and F₂ only yielded PrCl₃ and PrF₃.¹¹³ Efforts to synthesize PrF₄ using PrF₃ and Pr₆O₁₁ as starting materials yielded only PrF₃ as the final product even under high pressure and high temperature conditions.^{118, 119}

An indirect method has been successful for the synthesis of PrF₄ via the decomposition of Na₂PrF₆. In the process reported by Shamir *et al.*, Na₂PrF₆ is prepared from Na₂PrCl₅ under pressurized F₂ gas.¹²⁰ This product is then decomposed in liquid HF. This synthesis requires a rigorous experimental setup including the ability to distill anhydrous HF onto the intermediate compound. Specifically, Na₂PrF₆ was placed on a Teflon disc inside a Ni container and closed under an N₂ atmosphere. The container was then connected to an all metal vacuum line and evacuated. Anhydrous HF was then distilled onto the compound. The reaction proceeded by the decomposition of Na₂PrF₆ to PrF₄ and NaHF₂. However, the final product was found to be mixture of PrF₄ and PrF₃. Falconer *et al.*, in 1972 reported an alternative synthetic setup to isolated PrF₄ from the decomposition of Na₂PrF₆.¹¹⁷ This method involves heating intimate mixtures of NaF and PrF₃ under pressurized F₂ gas at 673 K for 4 hours. The resulting product was then washed with anhydrous HF. However, powder X-ray diffraction (PXRD) analysis of the product also indicates that the material generated by this method is not a single phase. Pure PrF₄, however, can be produced from its oxide precursor, Pr₆O₁₁, using KrF₂ as the oxidant based on the process reported by Kiselew *et al.*¹¹⁶ A less daunting synthesis for PrF₄ was reported by Mazej in 2002, which involved photodissociation of F₂.¹²¹ Pure PrF₄ can be synthesized at room temperature by the reaction of Pr₆O₁₁ in anhydrous HF with F₂ gas in the presence of ultraviolet light for 11 days.

Synthesis of LnO₂ (Ln = Ce, Pr, Tb). The binary oxides, CeO₂, PrO₂ and TbO₂ are less synthetically challenging to access than the binary fluorides. Ceria, CeO₂, is the most stable known dioxide of the lanthanides and finds wide-use in industry.¹⁰⁸⁻¹¹² CeO₂ can be prepared by decomposing corresponding hydroxide, nitrate, carbonate, oxalate, acetate, fluoride, chloride or sulfate in air. However, the final reactions have to be carried out at 1373 K to obtain phase pure stoichiometric CeO₂.¹²²

The dioxides of Pr and Tb can be prepared via dry or wet methods. The dry method for the synthesis of PrO₂, developed by Brinton and Pagel in 1929, involves heating Pr₆O₁₁ or mixtures of Pr₆O₁₁ and Pr₂O₃ under high pressures of oxygen in the temperature ranges of 473-673 K in a customized high-pressure furnace.¹²³ The process was later refined by McCullough in 1949 who replaced the high-pressure furnace with a sealed U-shaped quartz tube set up using NaClO₃ as the oxidizing agent (NaClO₃ was separated from the starting material by placing it on the other end of the U-shaped tube).⁹⁹ TbO₂ was later synthesized by Katz *et al.* in 1949 using a customized atomic oxygen furnace set up under reduced pressure and elevated temperature conditions using Tb₄O₇ as the starting material.¹²⁴ Katz also showed that this method

ARTICLE

Table 1. List of known Pr⁴⁺ compounds in the solid state with their lattice system/space group, Curie-Weiss constant (θ_{CW}), and effective magnetic moment (μ_{eff}).

Material	Structure	θ_{CW} (K)	μ_{eff} (μ_B)	Comments
Na ₂ PrO ₃ ^{95, 125 a}	<i>C2/c</i>	-15	0.99	Entropy recovered - $\sim 0.71R\ln 2$
Li ₂ PrO ₃ ⁹⁵	<i>Cmmm</i>	-32	1.75	Entropy recovered - $\sim 0.71R\ln 2$
SrPrO ₃ ⁹⁷	<i>Pbnm</i>	-----	1.57	No magnetic ordering down to 4.2K
BaPrO ₃ ^{126-130 a}	<i>Pnma</i>	-12	0.7	Exhibits a series of phase transitions at HT ($\chi_0 = 6.9 \times 10^{-4}$ emu/mol)
Sr ₂ PrO ₄ ^{96, 131, 132}	<i>Pbam</i>	-7.3	1.2	Entropy recovered - $\sim R\ln 2$ ($\chi_0 = 6.61 \times 10^{-4} \mu_B$)
Li ₈ PrO ₆ ^{133, 134}	<i>R$\bar{3}m$</i>	-----	0.505	Isolated octahedrons of Pr ⁴⁺ ($\chi_0 = 2.67 \times 10^{-4}$ emu/mol)
K ₂ PrO ₃ ^{135, 136 a}	<i>C2/c</i>	-140	2.4	Isostructural to Na ₂ PrO ₃
Cs ₂ PrO ₃ ^{137 a}	<i>Cmc2₁</i>	-101	3.54	-----
Rb ₂ PrO ₃ ^{135 a}	<i>C2/c</i>	-----	-----	-----
NaPrF ₅ ¹³⁸	Rhombohedral	-----	-----	Isostructural to NaPuF ₅
KPrF ₅ ¹³⁹	-----	-----	-----	-----
CsPrF ₅ ¹⁴⁰	Rhombohedral	-37	2.38	Colorless,
Li ₂ PrF ₆ ¹⁴¹	-----	-----	-----	Colorless, isostructural to Li ₂ ZrF ₆
Na ₂ PrF ₆ ^{140, 142}	<i>Immm</i>	-70	2.25	Colorless
K ₂ PrF ₆ ¹⁴⁰	-----	-62	2.24	Colorless
Rb ₂ PrF ₆ ¹⁴⁰	Hexagonal	-44	2.18	Colorless, isostructural to Rb ₂ UF ₆
Cs ₂ PrF ₆ ¹⁴⁰	Hexagonal	-130	2.14	Colorless
Na ₃ PrF ₇ ¹⁴¹	Cubic	-115	2.22	Colorless
K ₃ PrF ₇ ¹⁴¹	-----	-----	-----	Colorless, isostructural to (NH ₄) ₃ ZrF ₇
Cs ₃ PrF ₇ ¹⁴¹	Cubic	-97	2.21	Colorless
CdPrLi ₂ F ₈ ¹⁴¹	-----	-----	-----	Colorless, Scheelite type
BaPrF ₆ ¹⁴¹	-----	-----	-----	Colorless, isostructural to RbPaF ₆
PrF ₄ ^{117, 121, 142-144}	<i>C2/c</i>	-----	2.42	Colorless, isostructural to ZrF ₄
Rb ₂ CsPrF ₇ ¹⁴⁵	Cubic	-----	-----	Colorless
Cs ₂ RbPrF ₇ ¹⁴⁵	Cubic	-----	-----	Colorless
K ₂ RbPrF ₇ ¹⁴⁵	Cubic	-----	-----	Colorless
Rb ₂ KPrF ₇ ¹⁴⁵	Cubic	-----	-----	Colorless
Rb ₃ PrF ₇ ¹⁴⁵	Cubic	-----	-----	Colorless
CsRbKPrF ₇ ¹⁴⁵	Cubic	-----	-----	Colorless
Cs ₂ KPrF ₇ ¹⁴⁵	Cubic	-----	-----	Colorless
Rb ₂ Li ₁₄ Pr ₃ O ₁₄ ¹⁴⁶	-----	-----	-----	Isostructural to K ₂ Li ₁₄ Pb ₃ O ₁₄
PrO ₂ ^{147, 148}	<i>Pnma</i>	-105	2.32	Isostructural to CaF ₂

^a Polymorphs have been reported.

could be used to synthesize phase-pure PrO₂ from Pr₆O₁₁. Alternatively, Glocker and Rabideau demonstrated that phase pure PrO₂ can be synthesized by exposing Pr₆O₁₁ to ozone at room temperature for several days. The wet method involves a solvolytic disproportionation of the non-stoichiometric oxides. In 1966, Rao synthesized PrO₂ by suspending Pr₆O₁₁ in a 5% aqueous solution of acetic acid in the temperature range 320 – 350 K.^{147, 148} This reaction has been attributed to the selective dissolution/reaction of Pr³⁺. TbO_{2-x} was synthesized in a similar manner using Tb₄O₇ as the precursor. The reaction was deemed complete when the color of the solution turned green. It should

be noted that the maximum oxygen stoichiometry obtained for TbO_{2-x} is TbO_{1.95}.¹⁴⁸ All of the dioxides crystallize in a fluorite structure in the space group *Fm $\bar{3}m$* .¹⁴⁹ The crystal structure of PrO₂ is shown in Figure 5f.

There has been some speculation on the existence of Pr⁵⁺ in the solid-state. Prandtl and Rieder in 1938 reported the formation of YPrO₄ while heating mixtures of Pr₆O₁₁ and Y₂O₃ at 574 K in 15 atm of O₂.¹⁵⁰ Based on the ratio of atomic oxygen (in the final sample) to the oxygen present in Pr₂O₃, it was concluded that the Pr was pentavalent. However, efforts to reproduce the experiment by Marsh in 1946 lead to

ARTICLE

Table 2. List of known Tb⁴⁺ compounds in the solid state with their crystal structure, Curie-Weiss constant (θ_{CW}), and effective magnetic moment (μ_{eff}).

Material	Structure	θ_{CW} (K)	μ_{eff} (μ_B)	Comments
Na ₂ TbO ₃ ^{95, 125, 151, 152 a}	<i>C2/c</i>	-105	7.90	Entropy recovered - $\sim 0.71R\ln 8$
K ₂ TbO ₃ ^{136 a}	-----	-47	8.5	Isostructural to α -NaFeO ₂
Rb ₂ TbO ₃ ^{153 a}	-----	-57	7.9	Isostructural to α -NaFeO ₂
Cs ₂ TbO ₃ ^{153 a}	-----	-64	7.3	Isostructural to α -NaFeO ₂
SrTbO ₃ ¹⁵⁴	<i>Pnma</i>	-54.5	7.96	-----
BaTbO ₃ ^{154, 155}	<i>Pnma</i>	-52.8	7.96	-----
Li ₈ TbO ₆ ^{133, 134}	<i>R$\bar{3}m$</i>	-----	6.06	Isolated octahedrons of Tb ⁴⁺
Li ₂ TbF ₆ ¹⁵⁶⁻¹⁵⁹	<i>P12₁/c1</i>	-----	7.86	A rare example of Li in 5 coordination
Li ₄ TbF ₈ ¹⁶⁰	<i>Pnma</i>	-----	-----	-----
K ₂ TbF ₆ ¹⁵⁸	<i>C12/c1</i>	-----	4.44 ^b	K = [0.0074, 0, 0] magnetic structure
Rb ₂ TbF ₆ ¹⁵⁸	<i>C12/c1</i>	-----	6.27 ^b	K = [0.0104, 0, 0] magnetic structure
BaTbF ₆ ^{161 a}	<i>P$\bar{1}$</i>	-----	6.68 ^b	-----
CaTbF ₆ ^{162, 163}	<i>P4₂/m</i>	-----	-----	Undergoes a structural phase transition at 220K
KTbF ₅ ¹⁶⁴	<i>P$\bar{1}$</i>	-----	-----	T _N = 1.6K
CsTbF ₅ ¹⁶⁵	<i>Cmca</i>	-----	-----	No magnetic ordering down to 1.4K
RbTbF ₅ ¹⁶⁴	<i>P$\bar{1}$</i>	-----	-----	T _N = 1.4K
Cd ₂ TbF ₈ ¹⁶⁶	<i>I$\bar{4}$</i>	-----	-----	A 8 coordinate Terbium
Cs ₃ TbF ₇ ¹⁶⁷	<i>Fm$\bar{3}m$</i>	-----	-----	-----
K ₃ TbF ₇ ¹⁴⁵	Cubic	-----	-----	Colorless
Rb ₂ KTbF ₇ ¹⁴⁵	Cubic	-----	-----	Colorless
K ₂ RbTbF ₇ ¹⁴⁵	Cubic	-----	-----	Colorless
Rb ₃ TbF ₇ ¹⁴⁵	Cubic	-----	-----	Colorless
CsRbKTbF ₇ ¹⁴⁵	Cubic	-----	-----	Colorless
Cs ₂ KTbF ₇ ¹⁴⁵	Cubic	-----	-----	Colorless
Rb ₂ CsTbF ₇ ¹⁴⁵	Cubic	-----	-----	Colorless
Cs ₂ RbTbF ₇ ¹⁴⁵	Cubic	-----	-----	Colorless
CdTbF ₆ ¹⁶³	<i>P4₂/m</i>	-----	6.5 ^b	K = [$\frac{1}{2}$, $\frac{1}{2}$, 0] magnetic structure
SrTbF ₆ ¹⁶³	Orthorhombic	-----	-----	Undergoes a structural phase transition at 210K
LiTbO ₆ ¹⁶⁸	-----	-----	7.78	Brownish red
NaTbO ₆ ¹⁶⁸	-----	-----	8.03	Brownish red
KTbO ₆ ¹⁶⁸	-----	-----	7.96	Brownish red
Rb ₂ Li ₁₄ Tb ₃ O ₁₄ ¹⁶⁹	-----	-----	-----	Yellow single crystals, isostructural to K ₂ Li ₁₄ Pb ₃ O ₁₄
Cs ₂ Li ₁₄ Tb ₃ O ₁₄ ¹⁷⁰	-----	-----	-----	Orange single crystals, isostructural to K ₂ Li ₁₄ Pb ₃ O ₁₄
K ₂ GeTb ₂ O ₇ ⁹⁸	<i>C2/c</i>	-----	-----	Hydrothermal synthesis
TbO ₂ ^{147, 148, 171}	<i>Fm$\bar{3}m$</i>	-----	7.9	T _N = 3K
TbF ₄ ^{117, 121}	-----	-----	-----	-----

^a Polymorphs have been reported.

^b Ordered magnetic moments have been reported.

oxidation of Pr to only to the 4+ oxidation state.¹⁷² This discrepancy was attributed to the hygroscopic nature of Y₂O₃, and no adequate precautions were carried out by Prandtl and Rieder against exposure to atmospheric moisture.¹⁷² Later work by McCullough to oxidize Pr in the presence of other trivalent lanthanides also confirms the formation of Pr⁴⁺.⁹⁹ McCullough used the decrease in lattice constants for the solid solution in the Pr–Nd–O system from X-ray powder diffraction with

increase in oxidation state of Pr as evidence to support the tetravalent oxidation state of Pr.

Ternary Fluorides. Ternary fluorides of Ce⁴⁺ are the most stable amongst the fluorides with tetravalent lanthanides. A wide-range of ternary Ce⁴⁺ fluorides have been synthesized and a detailed accounting of these systems is not included here. The synthesis of ternary fluorides with Ce⁴⁺ such as K₃CeF₇ and K₂CeF₆ is relatively straightforward. Generally, phase pure compounds can be prepared by treating stoichiometric

mixtures of corresponding starting materials under a flow of F_2 gas diluted with N_2/Ar . The synthesis of ternary fluorides with Tb^{4+} is similar to Ce^{4+} in that it does not require high pressure fluorination. All known ternary fluorides with tetravalent Tb can be synthesized with F_2 gas (pure or diluted) employing $Tb_2O_3/Tb_4O_7/TbF_3/TbCl_3$ as starting materials.¹⁶⁷ The reactions are usually carried out in alumina boats if the temperature of the reaction is less than 773 K. Above 773 K, alumina reacts with F_2 generating AlF_3 . For reactions above 773 K, nickel boats are used with some risk of contaminating samples with Ni^{4+} . A proposed intermediate in the synthesis of ternary compounds is TbF_4 . Therefore care must be taken for reactions over 823 K, around which temperature TbF_4 decomposes eliminating fluorine and resulting in the formation of TbF_3 , which can react with remaining TbF_4 resulting in mixed valent compounds.¹⁷³ The synthesis of ternary fluorides of Pr^{4+} , however, requires high pressure fluorination.¹²²

Synthesis of $AlLnF_5$ (A = Na, K, Cs, Rb; Ln = Pr, Tb). $NaPrF_5$ was first reported by Hoppe in 1959.¹⁷⁴ However, this material is not completely structurally characterized. The formation of Pr^{4+} was confirmed with magnetometry and iodometry.¹⁷⁴ In 1961, Keenan and Asprey, synthesized $NaPrF_5$ by high pressure fluorination in the temperature ranges 473–673 K for several hours.¹³⁸ Stock solutions for Pr were made by dissolving corresponding oxide in hydrochloric acid. NaCl and Pr solutions were mixed in stoichiometric amounts and the mixture was evaporated to dryness, resulting in fine powders. The fine powders were ground and subjected to high-pressure fluorination. Based on PXRD and absorption spectroscopy, $NaPrF_5$ was found to contain only ~75% Pr^{4+} and the Pr^{3+} was attributed to reduction of Pr^{4+} by adventitious H_2O . Hoppe and Liebe in 1961 synthesized $CsPrF_5$ by treating stoichiometric mixtures of $CsCl$ and Pr_6O_{11} in a custom-built high-pressure fluorination furnace at 623 K.¹⁴⁰ There has been a report of the existence of $KPrF_5$ and $RbPrF_5$ however, definitive evidence has not been presented.¹³⁹

The Tb analogs were reported by Avignant in 1997.^{165, 175} The studies present the single-crystal X-ray structures of $KTbF_5$ and $CsTbF_5$ with 8 coordinate Tb^{4+} . It should be noted here that Hoppe and Rodder in 1961 had mentioned the existence of $KTbF_5$ and $CsTbF_5$ with unknown structures.¹⁷⁶ $RbTbF_5$ has been mentioned in literature and has been proposed to have the same crystal structure as $KTbF_5$.¹⁶⁷ $CsTbF_5$ crystallizes in the orthorhombic $Cmca$ space group with 20% edge shared and 80% corner shared polyhedrons of TbF_8 . $KTbF_5$ and $RbTbF_5$ crystallize in the $P\bar{1}$ space group with 50% corner and 50% edge shared polyhedrons of TbF_8 .

Synthesis of A_2LnF_6 (A = Li, Na, K, Cs, Rb; Ln = Pr, Tb). Li_2PrF_6 was synthesized by Hoppe and Feldner in 1983.¹⁴¹ Colorless powders of Li_2PrF_6 were determined to be in the hexagonal, $P\bar{3}1m$ space group. The synthesis and structural characterization of Na_2PrF_6 , K_2PrF_6 , Rb_2PrF_6 and Cs_2PrF_6 was reported by Hoppe and Liebe in 1961.¹⁴⁰ The synthesis involved treating stoichiometric mixtures of corresponding alkali chloride with Pr_6O_{11} at 763 K for Na_2PrF_6 , 723 K for K_2PrF_6 , 693 K for Rb_2PrF_6 , and 663 K for Cs_2PrF_6 . Na_2PrF_6 was characterized in a rhombohedral space group, while Rb_2PrF_6 and Cs_2PrF_6 were

characterized in a hexagonal space group. However, no structural information was available on K_2PrF_6 . Riesfeld revised the structural characterization Na_2PrF_6 to $Immm$ space group in 1967 yielding a cubic eight-fold coordination for Pr^{4+} .¹⁴² Tb^{4+} is only structurally characterized in Li_2TbF_6 , K_2TbF_6 , and Rb_2TbF_6 .¹⁷⁷ Synthesis involves treating stoichiometric mixtures of alkali fluoride and TbF_3 under a flow of F_2 gas at 773 K.¹⁷⁷ Li_2TbF_6 crystallizes in a $P2_1/c$ space group while K_2TbF_6 and Rb_2TbF_6 are isostructural to Li_2ZrF_6 and crystallize in the monoclinic $C2/c$ space group.^{157, 159, 178}

Synthesis of $M'LnF_6$ (M' = Ca, Ba, Cd, Sr; Ln = Pr, Tb). Within this class of compounds, Pr is only known in $BaPrF_6$.¹⁴¹ It has been reported to be isostructural to $RbPaF_6$ (orthorhombic $Cmma$).¹⁷⁹ However, for Tb^{4+} , four compounds are known with complete structural characterization. The Tb compounds were synthesized by treating stoichiometric mixtures of $M'F_2$ (M' = Ca, Sr, Ba, Cd) and TbF_4 under F_2 gas at 773 K – 993 K.¹⁶³ $SrTbF_6$ has been found to be isostructural to $BaPrF_6$ with edge sharing TbF_8 polyhedra resulting in linear TbF_6 chains linked by Sr^{2+} cations.^{163, 180} This motif is the most common structure type for $M'Ln^{4+}F_6$ compounds and is isostructural to $APaF_6$, $PbZrF_6$, $EuZrF_6$ and $SrZrF_6$ (A = NH_4 , K, Rb, Cs).¹⁸⁰ The structure of $CaTbF_6$ is closely related to $CaZrF_6$ and $CaUF_6$ – however, is not isostructural because of the difference in the coordination number of the tetravalent cations.¹⁶² The structure of $CdTbF_6$ based on X-ray and neutron diffraction appears to be isotopic to $CaTbF_6$. The Ca and Cd structures appear closely related to *anti*- $KSbF_6$ type anion-rich compounds. It should be noted here that while the structures of $CaTbF_6$ and $CdTbF_6$ have been solved using $P4_2/m$, there is some discrepancy due to the presence of unexplained superstructure peaks in their diffraction patterns. Ca and Cd compounds are reported to exhibit tetragonal distortion to isostructural $SrTbF_6$.¹⁸¹ The TbF_8 polyhedra share opposite orthogonal edges resulting in TbF_6 chains along the a-axis. CaF_6 and CdF_6 octahedra share corners with TbF_8 polyhedra from multiple chains. This difference in structure between $CaTbF_6$ and $SrTbF_6$ has been attributed to a slight rearrangement of the anion lattice to accommodate eight-coordinate Tb^{4+} cations.¹⁶²

$BaTbF_6$ was the first known tetravalent Tb fluoride with a polymorphic phase transition at high temperatures.¹⁸² The low temperature α - $BaTbF_6$ was first reported as an unknown structure by Feldner and Hoppe in 1983 and was later structurally characterized by Cousseins *et al.* in 1997 using single crystal X-ray diffraction (SC-XRD).^{141, 182} α - $BaTbF_6$ is found to be stable up to 823 K above which the high temperature β - $BaTbF_6$ begins to form. The structure of α - $BaTbF_6$ was solved in a triclinic $P\bar{1}$ space group and can be considered a triclinic distortion to isostructural $SrTbF_6$.¹⁸¹ The high temperature polymorph, β - $BaTbF_6$, is stable above 823 K. The structure of β - $BaTbF_6$ was solved by Avignant and found to be isostructural to $BaPrF_6$.

Synthesis of A_3LnF_7 (A = Na, K, Rb, Cs; Ln = Pr, Tb, Nd, Dy). A_3LnF_7 compounds are the only class of fluoride compounds with tetravalent lanthanides that are seven-coordinate. The Pr compounds with Na, K, Rb and Cs as the A site cation were synthesized in 1961 by Hoppe and Liebe using alkali metal

fluoride and PrF_3 as starting materials in temperature range of 663–883 K.¹⁴⁰ All four compounds were reported to be colorless and isostructural to $(\text{NH}_4)_3\text{ZrF}_7$.

In 1961 Hoppe and Rodder synthesized the first Tb^{4+} material in this class, Cs_3TbF_7 .¹⁷⁶ It was prepared from Tb_4O_7 and CsCl under F_2 gas at 663 K. There have been mentions of K_3TbF_7 and Rb_3TbF_7 in the literature which report them to be isostructural to Cs_3TbF_7 in the $(\text{NH}_4)_3\text{ZrF}_7$ setting.¹⁴⁵ The Nd^{4+} and Dy^{4+} materials are discussed separately (*vide infra*). Besides the major classes of ternary fluorides discussed above, two other Tb^{4+} fluorides have been reported: Cd_2TbF_8 and Li_4TbF_8 .^{160, 166}

Synthesis of Li_8LnO_6 oxides (Ln = Ce, Pr, Tb). Lithium rich oxides of the type Li_8MO_6 (M = Ce, Pr, Tb), isostructural to Li_8SnO_6 , were synthesized using Li_2O or Li_2O_2 as starting materials. The use of alternative sources for Li_2O like carbonates or nitrates did not yield the desired products. Methods to prepare single-crystal samples of the Pr^{4+} and Tb^{4+} materials were also reported.^{183, 184} Hoppe and Wolf in 1985 synthesized Li_8TbO_6 as bright yellow single crystals by heating an intimate, stoichiometric mixture of Tb_4O_7 and Li_2O_2 in a sealed silver tube at 853 K for 22 days.¹³⁴ Hoppe and Wolfe also reported the synthesis of pale-yellow single crystals of Li_8PrO_6 by heating stoichiometric mixtures of K_2PrO_3 and Li_2O_2 at 873 K in sealed Ag tubes for 20 days. Hoppe, Wolf, and Kroeschell in 1986 reported the synthesis of colorless single crystals of Li_8CeO_6 by treating stoichiometric mixtures of KCeO_2 and Li_2O_2 in Ag tubes at 923 K for 60 days.¹⁸³ The synthesis of powder samples of Li_8LnO_6 compounds was later reported by Hinatsu in 1996.¹³³ Hinatsu synthesized Li_8LnO_6 by heating stoichiometric mixtures of Li_2O (5% excess Li_2O was used) and corresponding lanthanide oxide (Pr_6O_{11} , Tb_4O_7 , and CeO_2) under an oxygen flow at 973 K. Li_8LnO_6 materials crystallize in the $R\bar{3}$ space group. The structure consists of isolated and slightly distorted LnO_6 octahedrons. Attempts to synthesize other alkali metal derivatives of Li_8LnO_6 type compounds were unsuccessful. Hoppe and Wolf in 1986 reported the synthesis of $\text{Li}_6\text{Tb}_2\text{O}_7$ (derivative of NaCl structure type with ordered vacancies in the anion lattice) by heat treating stoichiometric mixtures of Tb_4O_7 and Li_2O_2 at 1123 K for 22 days in gold tubes.¹⁶⁹

Synthesis of A_2LnO_3 oxides (A = Li, Na, K, Rb, Cs; Ln = Ce, Pr, Tb). Cubic NaCl derivatives of type A_2MO_3 are widely distributed across the periodic table. A_2MO_3 structure types can be considered as cation ordered derivatives of delafossites with structure type AMO_2 . A_2MO_3 structure types usually exhibit stable polymorphs at high temperatures.¹²² However, such polymorphs are found to be metastable with lanthanides and require quenching from high temperatures to capture the high-temperature modifications. A_2CeO_3 compounds are the most stable owing to the high thermodynamic stability of CeO_2 . It should be noted here that the synthesis of A_2LnO_3 requires the use of corresponding higher alkali metal oxides as starting materials (AO_x , $x > 0.5$). The use of alternative sources of AO_x like carbonates and nitrates has been proposed for the synthesis of transition metal based A_2MO_3 oxides. With lanthanides, such indirect methods are unsuccessful. However, in 2006 Hinatsu revised the synthesis of Li_2PrO_3 , by using

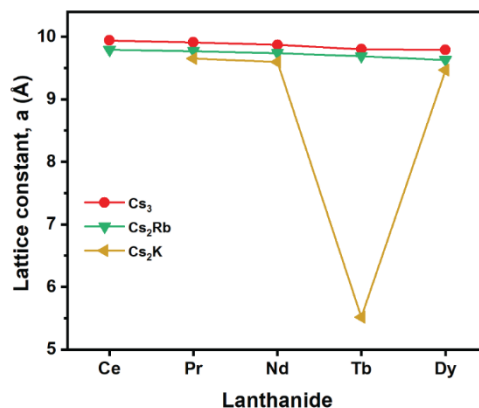


Figure 6. The lattice constants for cubic phase $\text{A}_2\text{A}'\text{LnF}_7$ (A = Rb, Cs; A' = Cs, Rb; Ln = Ce, Pr, Nd, Tb, Dy) plotted against corresponding lanthanide. It should be noted here that the lattice constants have not been plotted against ionic radii since the ionic radii of Nd^{4+} and Dy^{4+} are not well established. Figure adapted from reference 145.

stoichiometric mixtures of Li_2O and Pr_6O_{11} under an oxygen flow at 973 K for 12 hours.⁹⁵ In the same paper, a revised synthesis of Na_2LnO_3 was reported using stoichiometric mixtures of Na_2O_2 and corresponding lanthanide oxide (Pr_6O_{11} , Tb_4O_7 , and CeO_2) contained in gold tubes at 973 K for 12 hours under a flow of oxygen. In Li_2PrO_3 the PrO_6 octahedra are edge shared along c-axis and corner shared along the b-axis as shown in Figure 5b. In Na_2LnO_3 the LnO_6 and NaO_6 octahedra are edge shared forming 2D layers with Na atoms between the layers as shown in Figure 5a.

Synthesis of $\text{M}'\text{LnO}_3$ oxides (M' = Sr, Ba; Ln = Ce, Pr, Tb). $\text{M}'\text{BO}_3$ perovskites are widespread across the periodic table. Depending on the ratio of the ionic radii of A site and B site cation, given by the Goldschmidt tolerance factor, the perovskites deviate from the ideal cubic structure due to cooperative tilting of the BO_6 octahedron.⁹⁴ The cooperative tilting results in significant oxygen atom displacements and hence lowering the symmetry to either a trigonal or orthorhombic space group. Since Ce^{4+} and Pr^{4+} are closer in ionic radii compared to Tb^{4+} , Ce^{4+} and Pr^{4+} based perovskites exhibit similar structural features.

BaLnO_3 perovskites are synthesized by firing stoichiometric mixtures of BaCO_3 and CeO_2 ($\text{Pr}_2\text{O}_3/\text{Tb}_2\text{O}_3$) under a flow of oxygen at 1323 K for 48 hours twice. Hinatsu later reported the synthesis of BaPrO_3 and BaTbO_3 by treating stoichiometric mixtures of BaCO_3 and Pr_6O_{11} or Tb_4O_7 at 1573 K under a flow of oxygen.¹⁵⁵ BaPrO_3 and BaCeO_3 crystallize in orthorhombic $Pbnm$, while BaTbO_3 crystallizes in trigonal $R\bar{3}c$.¹⁸⁴ As expected, due to the decrease in ionic radii from Ce^{4+} to Tb^{4+} , the Goldschmidt tolerance factor increases from BaCeO_3 to BaTbO_3 , as shown in Figure 4. Since the ionic radius of Tb^{4+} is closer to the ionic radius of Ba^{2+} , the Goldschmidt tolerance factor is closer to unity, resulting in a higher symmetry space group for BaTbO_3 when compared to BaPrO_3 and BaCeO_3 .

However, the assignment of the BaTbO_3 space group is complex due to the difficulties in differentiating structural variations in these perovskites. This difficulty is likely due to variations in cooling rates, synthetic methods, and technical

developments in diffraction capabilities. Since its initial characterization by Hoppe and Paletta in 1966, the material has been solved in a range of space groups.^{136, 184-187} Most recently, high resolution neutron diffraction experiments across a wide range of temperatures by Ijdo *et al.* in 2004 showed that BaTbO₃ adopts an orthorhombic *Ibnm* below 280 K.¹⁸⁸ BaTbO₃ undergoes a phase transformation adopting a tetragonal *I4/mcm* above 280 K before adopting a cubic *Pm $\bar{3}$ m* space group above 623 K. A similar series of phase transformation has also been reported for BaCeO₃ and BaPbO₃.¹⁸⁹ SrLnO₃ perovskites can be synthesized using similar conditions as BaLnO₃ perovskites.¹⁸⁶ The room temperature structure of SrTbO₃ was solved using an orthorhombic *pnma* space group using neutron diffraction.¹⁸⁶ SrPrO₃ was reported to crystallize in an orthorhombic space group by Hinatsu *et al.*,⁹⁷ but later characterized using a monoclinic space group by Bukowski *et al.*¹⁹⁰ The crystal structure of SrPrO₃ is shown in Figure 5d.

Ruddlesden-Popper perovskites of the type $M'_{n+1}LnO_{3n+1}$ ($n=1$) are also known to stabilize lanthanides in the tetravalent oxidation state. However, only Sr₂CeO₄ and Sr₂PrO₄ have been isolated in this class of materials.¹⁹¹ Sr₂PrO₄ was synthesized by firing a stoichiometric mixture of Pr₆O₁₁ and SrCO₃ at 1273 K for 48 hours in a muffle furnace under ambient atmosphere.⁹⁶ Unlike the other Pr based oxides, Sr₂PrO₄ does not require a pure oxygen atmosphere. In Sr₂PrO₄, the PrO₆ octahedra form an edge shared chain along the b-axis as shown in Figure 5c.

Polynary phases. Besides the binary and ternary oxides and fluorides of tetravalent lanthanides, polynary systems can stabilize the lanthanide 4+ oxidation state. Kolis *et al.*⁹⁸ have described the synthesis of germanates that stabilize Tb⁴⁺ using hydrothermal conditions. In one such reaction, a KOH solution and Tb₄O₇ and GeO₂ as starting materials, were heated at 973 K under hydrothermal conditions. Two materials were isolated from the same reaction: Tb₁₃(GeO₄)₆O₇(OH) containing Tb³⁺ and K₂TbGe₂O₇ containing Tb⁴⁺. The crystal structure of K₂TbGe₂O₇ is shown in Figure 5e. Tb⁴⁺ has also been stabilized in germanate-based lattices using flux synthetic techniques. Zur Loye recently reported the synthesis of a mixed-valent Tb³⁺/Tb⁴⁺ material, Cs₈Tb₂³⁺Tb⁴⁺Ge₉O₂₇, using CsCl as a flux.¹⁹²

Tb⁴⁺ compounds have been stabilized in lattices using non-traditional solid-state techniques by making use of the ability to stabilize Tb⁴⁺ in aqueous solutions (like the hydrothermal method discussed above) in an appropriate ligand field. Ru-Dong *et al.*, in 1991, synthesized alkali Tb hexaiodate from basic aqueous solution using Tb³⁺ precursors and ozone as the oxidizing agent.¹⁶⁸ The Tb³⁺ precursor was synthesized by dissolving KIO₄ and KOH in distilled water followed by adding a Tb(NO₃)₃ solution dropwise. This colorless solution was oxidized using ozone until the solution changed color to a dark reddish-brown. The resulting solution was filtered, followed by addition of a saturated alkali nitrate solution to precipitate ATb⁴⁺IO₆ (A = Li, Na or K). These materials were characterized by magnetic measurements. There have also been reports of the existence of Pr⁴⁺ in polynary phases and these are listed in Table 1.^{145, 146}

Tetravalent Nd and Dy. Nd and Dy have also been isolated in their tetravalent oxidation states. The synthesis of Nd⁴⁺ and Dy⁴⁺ is often obscured due to competing reactions that result in

impure phases.¹⁹³ However, pure Nd⁴⁺ and Dy⁴⁺ compounds have been synthesized using high pressure fluorination.¹⁹³ So far, only six pure phases of Nd⁴⁺ and Dy⁴⁺ have been reported. All of the six compounds are of the type A₂A'MF₇ (A = Rb, Cs, A' = Rb, Cs, M = Nd, Dy). A₂A'MCl₆ was used as the starting material. Initially, the chloride was subjected to dilute fluorine gas (F₂: N₂ = 1:5) at ambient pressures in corundum containers at 673 K. These conditions resulted in a halogen exchange reaction leading to the formation of A₂A'MF₆. This fluoride compound was then subjected to high pressure fluorination in a Monel autoclave with 5 mL of liquid F₂ condensed into the autoclave at a pressure of 170 bar. The reaction was carried out at a temperature of 693 K for 2 hours. The heating rate was limited to ~35 K/min. After 2 hours, the autoclave was quenched from the furnace on to a stream of cold air followed by dipping in to liquid N₂.¹⁹³

All of the six compounds crystallize in a cubic phase with their lattice parameters co-plotted with their Ce, Pr, and Tb analogs in Figure 6. The lattice constants for A₂A'LnF₇ materials decrease monotonically due to a decrease in ionic radii from Ce⁴⁺ to Dy⁴⁺ confirming the tetravalent oxidation state of Nd and Dy (the anomalous lattice constant for Cs₂KTbF₇ is not explained in the literature). Kaindl (*vide infra*) later confirmed the tetravalent oxidation state of Nd and Dy in the materials using Ln L₃-edge, M_{5,4}-edge, and F K-edge X-ray absorption spectroscopy (XAS) studies. However, no magnetic measurements have been reported for either Nd⁴⁺ or Dy⁴⁺ materials. It should be noted here that A₂A'LnF₆ also crystallizes in a cubic space group. The final products were microcrystalline and were described as yellow/orange in color.¹⁴⁵

There have also been reports of the presence of Dy⁴⁺ in perovskite-based oxides. Brauer and Kristen in 1980 reported that BaCeO₃ was able to stabilize tetravalent Dy doped up to 5% loading.¹⁹⁴ However, Soderholm *et al.* in 1987 showed the dysprosium in the system was not tetravalent using Mossbauer spectroscopy.¹⁹⁵ Shinoda *et al.* in 2012 synthesized 20% Dy doped in BaZrO₃ lattice under an O₂ atmosphere at 1893 K.¹⁹⁶ A black pellet was obtained after the reaction and the phase purity was confirmed by X-ray diffraction. Under a reducing H₂ atmosphere, the pellet changed to white color. L₃-edge X-ray absorption near edge spectroscopy (XANES) was used as the primary technique to determine the oxidation state of the Dy. The L₃-edge XAS spectrum for the black pellet exhibits a multi-peak feature while the L₃-edge XAS spectrum for the white pellet exhibits a single peak feature analogous to Dy₂O₃. Hence, the authors concluded that the Dy in BaZrO₃ even under oxidizing atmospheres is mixed-valent with both Dy³⁺ and Dy⁴⁺.

Electronic Structure and Physical Properties of Ln⁴⁺ Phases.

Extensive studies have been carried out to understand the single-ion and bulk behavior of Pr⁴⁺ systems (PrO₂ and BaPrO₃). These studies were primarily motivated due to the anomalous behavior of Pr-doped YBa₂Cu₃O₇, a high temperature superconducting layered perovskite.^{126, 197} In this class of materials, the superconducting transition temperature is relatively insensitive to doping of Y with a trivalent lanthanide, except for Ce, Pr, or Tb. Pr, in particular, has a notable effect on

ARTICLE

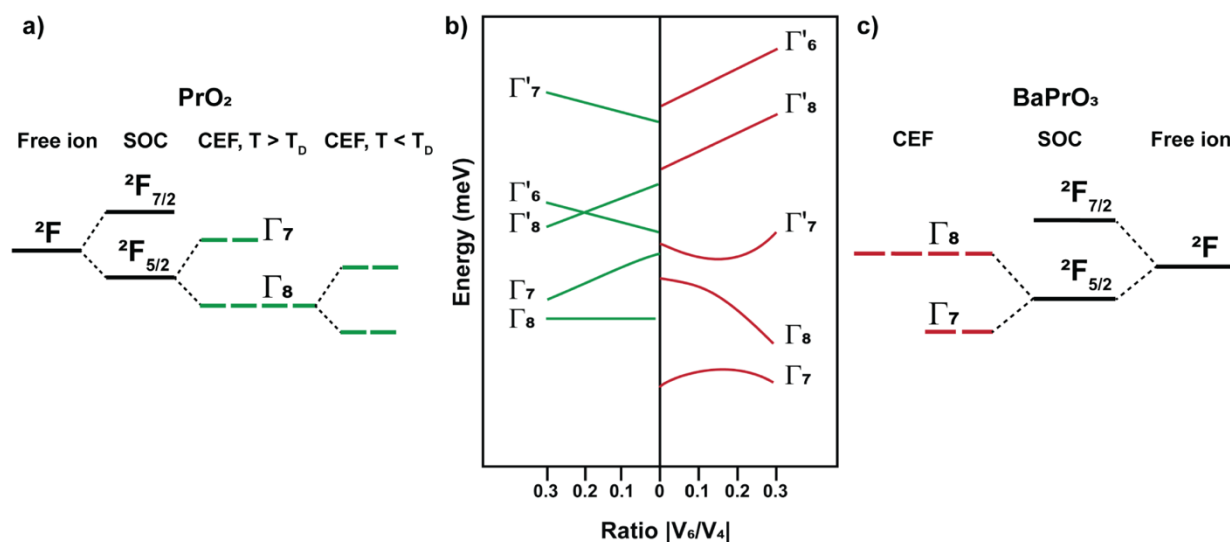


Figure 7. a) Crystal electric field (CEF) splitting diagram for PrO_2 above and below phase transformation (T_D). The black lines indicate splitting by spin orbit coupling (SOC), the yellow lines indicate splitting by a cubic CEF. b) CEF energy diagram for PrO_2 and BaPrO_3 plotted for different values of $|V_6/V_4|$. The irreducible representations in the excited state $J = 7/2$ manifold is indicated by primes. c) CEF splitting diagram for BaPrO_3 . The black lines indicate splitting by SOC, and the brown lines indicate splitting by O_h CEF. Figure 7b was adapted from reference 198.

the superconducting transition temperature, which decreases with increasing Pr concentration. Superconductivity is completely suppressed in the end member $\text{PrBa}_2\text{Cu}_3\text{O}_7$ which is an antiferromagnetic (AFM) insulator.¹⁹⁷

This observation suggests that accessibility of Pr^{4+} may affect the superconducting transition temperature. Several theories have been proposed to explain the suppression of superconductivity.¹⁹⁹⁻²⁰³ These explanations contend with the observation that the susceptibility χ vs T plot deviates strongly from expectation for a Pr^{3+} system. Additionally, Pr L_3 -edge XAS studies by Soderholm and co-workers indicate that Pr is mixed-valent in $\text{PrBa}_2\text{Cu}_3\text{O}_7$ at room-temperature.^{201, 204} Hence, studies on the behavior of Pr^{4+} ions in simpler phases such as BaPrO_3 and PrO_2 were used to examine the behavior of $\text{PrBa}_2\text{Cu}_3\text{O}_7$. It should be noted here that $\text{CeBa}_2\text{Cu}_3\text{O}_7$ and $\text{TbBa}_2\text{Cu}_3\text{O}_7$ also do not exhibit superconductivity, however, these materials are often accompanied by impurities like BaCeO_3 and BaTbO_3 during synthesis making it difficult to correlate the suppression of superconductivity with the doping of the parent material, $\text{YBa}_2\text{Cu}_3\text{O}_7$.²⁰²

PrO_2 has been used to understand the interplay between spin and unquenched orbital moments in $4f$ electrons leading to competing interactions including magnetoelastic coupling, Jahn-Teller distortion, crystal electric field states, and the phonon density of states.¹⁰⁷ PrO_2 is isostructural to CeO_2 , TbO_2 , UO_2 , NpO_2 , PuO_2 , and CmO_2 and crystallizes in a cubic fluorite

type lattice. As a result, it provides a model system to understand how small perturbations affect these competing interactions. One the consequences of these competing interactions is a phase change at 120 K for PrO_2 (*vide infra*). In the high temperature, paramagnetic regime, it offers a less complicated Hamiltonian since it is a $4f^1$ system.^{107, 205} However, among the three binary lanthanide oxides, LnO_2 ($\text{Ln} = \text{Ce}, \text{Pr}, \text{Tb}$), only Pr can display multipolar effects since Ce^{4+} is closed shell with a $4f^0$ ground state and Tb^{4+} is isotropic with a $4f^7$ ground state, and displays a quenched orbital moment. As a result, only PrO_2 presents a wide-range of interesting low temperature phenomena including a phase transition driven by hidden magnetic multipoles, coupling between magnetic multipoles, and a Jahn-Teller effect driven magnetoelastic interaction competing with crystal field effects.

A distinctive feature of the PrO_2 phase behavior is a quadrupolar phase transition (T_D) at 120K. This phase transition has been attributed to a cooperative static Jahn-Teller transition, very similar to UO_2 .^{206, 207} However, the transition temperature in UO_2 (30.8 K) is lower than PrO_2 (120 K). Below the transition temperature in PrO_2 , the oxygen atoms are displaced from their ideal positions, while the Pr sublattice remains unaffected resulting in a doubling of the unit cell along one crystallographic direction. PrO_2 then undergoes a second order AFM transition around 13.5 K. The magnetic structure of PrO_2 has been studied using neutron diffraction experiments.

The magnetic structure can be described using two components: 1) $k = [1, 0, 0]$ with an ordered magnetic moment of $0.65 \mu_B$, typical of a type 1 AFM transition and very similar to the magnetic structure of UO_2 , 2) $k = [1, \frac{1}{2}, 0]$ with an ordered magnetic moment of $0.35 \mu_B$.²⁰⁶

To understand the magnetoelastic coupling in PrO_2 and closely related UO_2 , NpO_2 , PuO_2 , and CmO_2 , and to explain the suppression of superconductivity in $PrBa_2Cu_3O_7$, it is essential to understand the crystal field states for a Pr^{4+} single ion. Pr^{4+} is isoelectronic to Ce^{3+} (and electronically related to Pa^{4+} , U^{5+} and Np^{6+}). Ce^{3+} is well understood from the LS coupling limit. Using the model established for Ce^{3+} , Pr^{4+} with $4f^1$ electronic configuration should exhibit a ${}^2F_{5/2}$ ground state with a ${}^2F_{7/2}$ excited state. In PrO_2 , the excited state J multiplet is 370 meV above the ground state. The ${}^2F_{5/2}$ multiplet is further split by crystal field into Γ_7 doublet and Γ_8 quartet states and the ground state is strongly determined by the point group symmetry at the metal ion. The ground state in PrO_2 is the Γ_8 quartet with a Γ_7 doublet excited state. The corresponding excited state for PrO_2 was measured at 130 meV using inelastic neutron scattering (INS).^{198, 205} It should be noted here that below T_D the Γ_8 splits into two doublets because of the change in the point symmetry at the metal center as shown in Figure 7a.²⁰⁸ The crystal electric field (CEF) for PrO_2 was modelled using the following Hamiltonian¹⁹⁸:

$$H_{CEF} = V_4\beta(O_4^0 + 5O_4^4) + V_6\gamma(O_6^0 - 21O_6^4) \quad (4)$$

where, β and γ are Stevens factors, O_m^n are factors related to spherical harmonic, $V_4 = A_4 \langle r^4 \rangle$, and $V_6 = A_6 \langle r^6 \rangle$, where $\langle r^n \rangle$ is the expectation value of f electrons. Since only one CEF transition was observed for PrO_2 , it was not possible to determine V_4 and V_6 independently. Hence, the CEF Hamiltonian was transformed with only one variable by assuming a value of 0.05 for the ratio V_6/V_4 . Figure 7b shows the CEF diagram for PrO_2 for different ratios of V_6/V_4 . With a ratio of 0.05, V_4 was calculated to be -66 meV for PrO_2 .¹⁹⁸ The V_4 value calculated for PrO_2 is significantly larger when compared to values of 10-15 meV for Pr^{3+} in metallic mononictides.²⁰⁹

The inelastic neutron spectra for PrO_2 acquired by several groups were more structured than anticipated.^{205, 208, 210} Below T_N , the spectrum shows a multitude of magnetic transitions not implicated by the CEF. Further investigations by Webster *et al.*, classified these transitions into 3 regions: 1) a broadband scattering above 10 meV which is independent of temperature and exists well above the Néel temperature (T_N) and T_D , 2) a broadband scattering above 35 meV independent of temperature, and 3) scattering below 35 meV which was dependent on temperature.²⁰⁸ This third region corresponds to the transition between the two doublets split from the Γ_8 quartet below T_D (estimated to be around ~ 21 meV). Regions 1 and 2 have been attributed to a continuum of vibronic scattering. Mean-field analysis by Jensen, as part of efforts to understand UO_2 and NpO_2 , predicts the first CEF to be around 100 meV.²¹¹ Jensen's model suggests that the discrepancy with

the experiment is the result of magnetoelastic coupling, which increases the CEF to 130 meV.

The magnetic structure was estimated using an Ising-like Heisenberg interaction Hamiltonian to model the spin wave feature observed in INS.²¹¹ However, the calculated ordered moment was 40% larger than the observed ordered moment. This Hamiltonian takes into account the coupling between the CEF states and phonon states which causes a reduction in the magnetic moment. However, this model was not sufficient to explain the observed magnetic moment.²¹⁰ Jensen suggested that these discrepancies between the observed and estimated magnetic moments could be due to multipolar effects.²¹¹ Even though the low symmetry structure below T_D is observed to have a doublet ground state, there could be some multipolar effects in play which might be crucial to understand these cubic binary oxide materials.^{212, 213}

As discussed in the thermochemistry section, $BaPrO_3$ has unique stability likely attributable to its electronic structure. Furthermore, since $BaPrO_3$ is a potential impurity in Pr doped $YBa_2Cu_3O_7$, an understanding of its underlying electronic structure is necessary to interpret the physical behavior of the related YBCO phases. $BaPrO_3$ undergoes AFM ordering at 11.5 K as evident from susceptibility measurements. The inverse susceptibility vs T curve shows a significant deviation from the Curie-Weiss law. Further studies have shown that there is a temperature independent paramagnetism (TIP) term associated with the susceptibility.^{126, 127, 130, 155} After TIP subtraction, the magnetic moment per Pr^{4+} was calculated to be in the range of 0.5-0.9 μ_B (based on the value chosen for TIP), much less than the value expected for ${}^2F_{5/2}$ ground state in a LS coupling scheme (e.g. ${}^2F_{5/2}$ is the ground state for Ce^{3+}). This divergence indicates that the crystal field has a significant effect on the behavior of Pr^{4+} . While $BaPrO_3$ undergoes long-range ordering, $SrPrO_3$ shows no magnetic ordering down to 2 K as seen from susceptibility data.⁹⁷ Again, to be noted is the deviation of inverse susceptibility vs T curve from the Curie-Weiss law. After a reasonable approximation of the TIP term, the magnetic moment per Pr^{4+} was calculated to be 1.57 μ_B , greater than the value calculated in $BaPrO_3$ but still less than the expected value for a ${}^2F_{5/2}$ ground state.⁹⁷ The difference of magnetic properties between $BaPrO_3$ and $SrPrO_3$ was attributed to changes in the $Pr^{4+}-O^{2-}-Pr^{4+}$ angles due to difference in the size of Ba^{2+} and Sr^{2+} cations.⁹⁷

Thermodynamic signatures for long range AFM ordering were observed in $BaPrO_3$ using specific heat measurements with the presence of a λ like feature centered around 11.5 K. However, no such measurements have been carried out in $SrPrO_3$.^{97, 126} To find the nature of the magnetic order in $BaPrO_3$, neutron diffraction experiments were performed. However, the magnetic scattering was weak, and the magnetic and nuclear Bragg peaks are coincident. With the help of a triple axis neutron instrument, a 1% intensity increase in the nuclear Bragg peaks below T_N was observed implying that the AFM structure is a $k = [0, 0, 0]$ structure.¹⁹⁷ Assuming a collinear magnetic structure, the thermally averaged ordered magnetic moment of Pr^{4+} in $BaPrO_3$ was calculated to be 0.35(5) μ_B . Magnetization studies on $BaPrO_3$ are indicative of a small ferromagnetic

component associated with magnetic ordering. It was hinted that the ferromagnetic component could be either associated with spin canting or to magneto structural transition across the T_N .¹²⁶

Hence it was crucial to observe the direction of magnetic moment in BaPrO₃. Rigorous neutron diffraction experiments using cold neutrons on BaPrO₃, show that the magnetic moment is aligned along the *a*-axis with a small ferromagnetic component aligned along the *z* direction (*c*-axis).¹²⁷ A significant assumption was made that the magnetic form factor for Pr⁴⁺ is the same as Pr³⁺. It should be noted here that, the low magnetic moment of Pr⁴⁺, poses significant challenges in using neutrons to probe the low temperature spin dynamics in these systems.^{127, 197} In BaPrO₃ the ground state J multiplet is split by the O_h crystal field into a Γ_7 doublet ground state and a Γ_8 quartet excited state (260 meV above the ground state) as seen in Figure 7c. Similar to PrO₂, the excited state J multiplet $^2F_{7/2}$ is separated from the ground state by 370 meV. The CEF for Pr⁴⁺ in BaPrO₃ was modeled using the same Hamiltonian as Equation 2. With the same ratio of 0.05 for V_6/V_4 , V_4 was calculated to be +119 meV, which is twice as large as the value calculated for PrO₂ ($V_4 = -66$ meV) with opposite sign. Figure 7b shows the CEF diagram for BaPrO₃ for different ratios of V_6/V_4 .¹⁹⁸ This figure could potentially be used as a guideline for future CEF predictions in other Pr⁴⁺ systems.

Several other Pr⁴⁺ systems have been examined in some detail. Li₂PrO₃ undergoes an AFM transition at 6.5 K.⁹⁵ Again, to be noted is the deviation of the inverse susceptibility vs T curve from the Curie-Weiss law. After TIP subtraction, the magnetic moment was calculated to be 1.75 μ_B . Specific heat measurements further confirm the long-range ordering at 6.5 K. Long range AFM ordering was observed in Na₂PrO₃ at 4.6 K.⁹⁵ Deviation from the Curie-Weiss law is also observed for Na₂PrO₃. Specific heat further confirms the long-range ordering in Na₂PrO₃. The magnetic entropy recovered due to the long-range ordering in A₂PrO₃ (A = Li, Na) and BaPrO₃ have been calculated by subtracting the phonon contribution at high temperature using diamagnetic analogs. The entropy recovered for an f^1 ion with a doublet ground state should be $R\ln 2$. However, in all the three Pr⁴⁺ compounds discussed above, there is a universal behavior that the entropy recovered is only 71% of $R\ln 2$. This behavior, and the origin of the TIP term remain open questions.

Similar to other Pr⁴⁺ oxides, in Sr₂PrO₄ the susceptibility deviates from the Curie-Weiss law. After a TIP subtraction, the effective magnetic moment of Pr⁴⁺ in Sr₂PrO₄ was calculated to be 1.20 μ_B . Specific heat measurements further confirm the long range ordering.¹³¹ However, unlike the other Pr⁴⁺ oxides, the Pr⁴⁺ ions in Sr₂PrO₄ recover 94% of $R\ln 2$, making it an outlier from the observed general behavior. Neutron diffraction measurements on Sr₂PrO₄ below T_N did not show any magnetic Bragg peaks and was attributed to the low ordered magnetic moment of Pr⁴⁺.¹³² For the lithium rich oxides of the type Li₈LnO₆ (Ln = Ce, Pr, Tb), no magnetic ordering was observed for Li₈PrO₆ down to 2 K and the susceptibility also deviates from Curie-Weiss behavior. After a TIP subtraction, the effective magnetic moment was calculated to be 0.503 μ_B . No specific heat

measurements were reported.¹³³ TIP terms along with Curie-Weiss constants and effective magnetic moments for a number of Pr⁴⁺ oxides and fluorides are listed in Table 1.

Magnetic measurements have also been carried out for oxides and fluorides containing Tb⁴⁺ ions. Na₂TbO₃, SrTbO₃, and BaTbO₃ (isostructural to the Pr analogs) exhibit long range AFM ordering at 38.3 K, 32.0 K and 33.4 K respectively.⁹⁵ Unlike the oxides of Pr⁴⁺, the susceptibility follows Curie-Weiss behavior down to T_N yielding a magnetic moment of 7.9 μ_B , 7.83 μ_B , and 7.88 μ_B for Na₂TbO₃, SrTbO₃ and BaTbO₃, respectively.^{151, 154, 155} The calculated μ_{eff} is slightly lower than the expected value for a $4f^7$ ion with a $^8S_{7/2}$ ground state (*LS* coupling limit). The small difference between the calculated and theoretical values has been attributed to an increased crystal field compared to Tb³⁺. Specific heat measurements have been carried out to confirm the long-range ordering in Na₂TbO₃. The entropy recovered saturates at 71% $R\ln 8$. This observation is reasonable if the ground state of Tb⁴⁺ is an octet.¹⁵¹ Curie-Weiss constants and effective magnetic moments for a number of Tb⁴⁺ oxides and fluorides are listed in Table 2.

4. Gas-Phase Chemistry

While this review is focused on the established solid-state and molecular chemistry of the tetravalent lanthanides, the gas-phase redox chemistry also provides important structural and thermodynamic insight into the stability of high-valent lanthanide complexes. In line with the relative instability of PrF₄ (in comparison to CeF₄ and TbF₄) as evidenced by its thermal decomposition at 363 K, its infrared spectrum in matrix-isolation studies was not known until 2015.²¹⁴ Subsequently, a complete study of the lanthanide fluorides across the series established that, in addition to the previously identified neutral tetravalent lanthanides – CeF₄, PrF₄, and TbF₄, NdF₄, and DyF₄ could be identified in matrix isolation studies (Ar or Ne matrix, 20-35 K) in the reaction of laser-ablated lanthanide metal and F₂ gas.²¹⁵ It should be noted that neither SmF₄ or HoF₄ were observed despite the fact that the fourth ionization energies of Sm and Ho are not substantially greater than that of Dy. The accessibility of tetravalent neutral fluorides is thus in accordance with observed tetravalent lanthanides characterized in the solid-state as their [LnF₇]³⁻ salts. Additionally, Riedel and co-workers predicted a similar Ho–F bond disassociation energy (BDE) in HoF₄ to that found for NdF₄ yet found no spectroscopic evidence for its existence under these conditions.

Andrews and Dixon described the observation of tetravalent Ce, Pr, and Tb as their neutral hydroxides in an argon matrix at 4 K from the reaction of hydrogen peroxide and laser ablated lanthanide metal ions.²¹⁶ The formation of terminal oxide tetravalent lanthanides in matrix isolation studies and mass spectrometry has been observed via the fragmentation of [Ln(NO₃)₄]¹⁻ to [LnO(NO₃)₃]¹⁻ and in the reaction of ablated lanthanide metal with oxygen difluoride to form [LnOF₂].^{217, 218} In these species, the oxide can be either mono- or dianionic. Based on quantum chemical calculations, hydrolysis kinetics, and the fourth ionization potentials of the lanthanides, Gibson and co-workers find that only Ce is truly tetravalent in

[Ln(NO₃)₃]¹⁻, and that Pr, Nd, and Tb have intermediate oxidation states, Ln^{4+/3+}, and that all other lanthanides are trivalent in these anions. Similarly, Andrews and co-workers find that Ce is tetravalent in [CeOF₂] and that Pr and Tb are intermediate between Ln³⁺ and Ln⁴⁺.

Remarkably, pentavalent Pr has been identified in gas-phase reactions both through matrix isolation and mass spectrometry. This finding has no precedence in either solution, molecular chemistry, or extended solids. While the possibility of Pr pentafluoride has been explored,²¹⁴ the first evidence of a pentavalent Pr ion was reported in 2016 by Zhou and co-workers in which the [PrO₂]⁺ ion was identified by both mass spectrometry and matrix isolation in conjunction with quantum chemical calculations.²¹⁹ The [PrO₂]⁺ was generated by the reaction of laser ablated Pr metal with O₂ seeded He in a supersonic expansion source. It should be noted that prior work identified [PrO₃]¹⁻ in laser ablation studies of Pr with O₂ in a solid-Ar matrix. Subsequent quantum chemical calculations indicate that the [PrO₃]¹⁻ is Pr⁴⁺ with a ligand radical.²²⁰ Dau, Gibson, and co-workers also identified [PrO₂]⁺ in the reaction of NO₂ and PrO⁺ in a quadrupole ion trap (QIT) as part of studies identifying pentavalent Bk and Cf.²²¹ This product was likely also identified previously by Bohme and co-workers in 2009 using a selected ion flow tube. Gibson and co-workers also observed Pr⁵⁺ in a gas-phase nitrate complex, [PrO₂(NO₃)₂]¹⁻ via low-energy collision induced dissociation (CID) in a QIT, through NO₂ elimination from their previously identified monooxo anion, [PrO(NO₃)₃]¹⁻.^{218, 222} This methodology has been extended to the identification of Cm⁵⁺, Bk⁵⁺, and Cf⁵⁺ nitrate complexes.²²³ Recently, through use of matrix-isolation infrared absorption (IR) spectroscopy and quantum chemical calculations both NPrO and [NPrO]¹⁻ were identified.²²⁴ Both of these are linear molecules, and the neutral complex is pentavalent. These high-valent lanthanide complexes identified in gas-phase reactions indicate that substantial new chemistry in condensed phases may be accessible through ligand and methodology development.

5. Solution Thermochemistry of Ln⁴⁺

To ground the discussion of the observation of tetravalent lanthanides in solution and the isolation of molecular complexes of tetravalent lanthanides, the experimental and theoretical aqueous thermochemistry of these ions is presented in condensed form. These studies have been reviewed in detail previously.⁸⁰ Table 3 contains the standard oxidation potentials E°(M³⁺→M⁴⁺) for the lanthanides. The only reversible couple observed in solution is that for Ce³⁺/Ce⁴⁺.^{225, 226} Derived experimental values are available for Pr, Nd, Tb, and Dy.²²⁶⁻²²⁹ Predicted values are derived from either consideration of free energies⁸⁰ or from the linear correlation of the *f-d* absorption band energy of the trivalent ions.²²⁹ These two models are remarkably consistent and correlate reasonably with the few experimental values available. Table 3 defines the experimental difficulty in observing tetravalent lanthanides other than Ce in aqueous media: all of them have oxidation potentials more positive than 3.1 V vs. the normal hydrogen electrode (NHE).

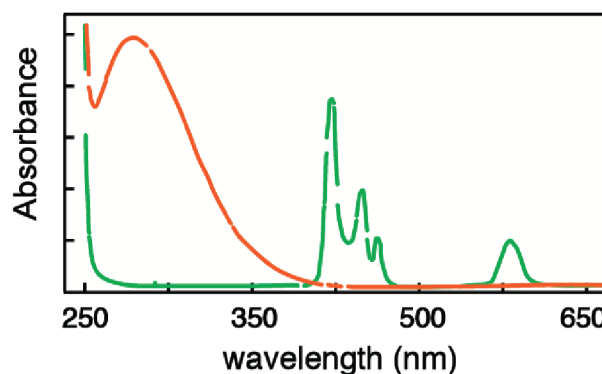


Figure 8. UV/vis spectrum of Pr³⁺ starting solution (green) and UV/vis of solution after oxidation to Pr⁴⁺ (orange). Figure adapted from 234.

6. Aqueous Chemistry

Tetravalent Pr and Tb are both exceptionally oxidizing ions to stabilize in aqueous media. However, the potential to isolate or observe these ions in solution has been pursued since at least 1963 when Pajakoff claimed the isolation of chloride, nitrate, and sulfate complexes of tetravalent Pr.²³⁰ These synthetic studies, which present minimal evidence of purity, were

Table 3. Ground state term, measured potential (V) (where applicable), and calculated Ln(3+/4+) oxidation potential (V) for the lanthanides.

Element Ln ³⁺	Ground State	Measured E° (V)	Calculated E° (V) ^{80 a}	Calculated E° (V) ^{229 b}
Ce	² F _{5/2}	1.74 ^{225, 226}	1.76	1.75
Pr	³ H ₄	3.2 ± 0.2	3.9	3.2
Nd	⁴ I _{9/2}	5.0 ± 0.4	4.9	4.4
Pm	⁵ I ₄	--	5.4	4.7
Sm	⁶ H _{5/2}	--	5.2	5.1
Eu	⁷ F ₀	--	6.2	6.3
Gd	⁸ S _{7/2}	--	7.4	7.9
Tb	⁷ F ₆	3.1 ± 0.2	--	3.1
Dy	⁶ H _{15/2}	5.2 ± 0.4	4.5	4.9
Ho	⁵ I ₈	--	5.7	6.0
Er	⁴ I _{15/2}	--	5.7	6.1
Tm	³ H ₆	--	5.6	6.1
Yb	² F _{7/2}	--	6.8	7.3
Lu	¹ S ₀	--	8.1	9.1

a. Values calculated based on free energy of formations for trivalent and tetravalent ions.

b. Values calculated based on correlation to first *f-d* absorption band energy.

accompanied by ultraviolet/visible (UV/vis) spectroscopy. These spectra, in light of later studies (*vide infra*), are suggestive that Pajakoff was able to at least partially oxidize Pr³⁺ to tetravalent Pr⁴⁺. However, contemporary authors disputed these claims and no later resolution of these synthetic approaches has been reported.^{231, 232}

Definitive spectroscopic evidence for aqueous tetravalent Pr and Tb was presented by Hobart and Peterson in 1980.^{233, 234} These studies reported UV/vis spectroscopic characterization of the ozonolysis and electrolysis of alkaline, carbonate solutions of TbCl₃ and PrCl₃. In the case of the spectroelectrochemical

characterization, a potential of +1.4 V (vs. saturated calomel electrode (SCE)) was applied to 0.1 M solutions of PrCl_3 and a potential of +1.3 V (vs. SCE) was applied to 0.1 M solutions of TbCl_3 (both experiments were conducted in 1 M KOH and 5.5 M K_2CO_3). In the case of Pr, the original pale green solution changed to a pale-yellow solution as evidenced by the UV/vis spectrum (Figure 8). For the Tb solution, the initially colorless solution changes to deep reddish-brown. In both cases, the color change is attributed to the onset of a strong ligand to metal charge transfer (LMCT) feature and, as evidence by UV/spectroscopy, the bleaching of $f-f$ features that are diagnostic for the trivalent ions. Similar results were obtained by bubbling ozone through the solutions and Pr^{4+} and Tb^{4+} . These solutions were found to be stable with carbonate in the range of 2 – 5 M. A subsequent study also documented the hydroxide concentration dependence of Tb^{4+} and found that under low concentration (0.15 to 0.3 M) Tb^{4+} precipitates at 1 M K_2CO_3 , while at 1 M K_2CO_3 it remains in solution and bleaches over an hour.²³⁵ At high concentration of KOH (0.5 M) and 5 M K_2CO_3 the Tb^{4+} solution is stable for weeks. The methods were extended to the study of tetravalent actinides in aqueous solutions.^{233, 236}

These *in-situ* oxidation studies with ozone were extended to acetonitrile solutions of $\text{M}(\text{NO}_3)_3 \cdot 6\text{H}_2\text{O}$ ($\text{M} = \text{Ce}, \text{Pr}, \text{and Tb}$) in the presence of two equivalents of either triphenylphosphine oxide or triphenylarsine oxide by Payne and Peterson.²³⁷ The ozonolysis of these solutions was performed for 1–24 h at 70 °C. In the case of Ce, the reaction produced a purple solution which turned brown on precipitation. For Pr and Tb, these reactions produced yellow solutions and yellow precipitates that were observed to be stable to air and moisture. UV/vis spectroscopy of the Pr reaction revealed bleaching of $f-f$ transitions diagnostic for Pr^{3+} and the growth of an intense feature at 352 nm assigned as a LMCT. This behavior is analogous to that observed for the carbonate ozonolysis reactions.

The chemical oxidation of Tb has been reported in aqueous solutions of tetrametaphosphate, phosphotungstates, pyrophosphates, tellurates, condensed phosphates, and highly concentrated potassium hydroxide.^{238–243} Li and co-workers presented a detailed concentration and temperature dependence study of the oxidation of Tb in tetrametaphosphate solutions. These oxidations were performed with ozone and demonstrated similar UV/vis spectroscopic features (broad feature at 365 nm) for the tetravalent Tb species in these solutions. This red-brown oxidation product was also quenched immediately upon the addition of hydrogen peroxide. The oxidation rate was found to be dependent on pH, temperature, and concentration of tetrametaphosphate. Qualitatively, these results are similar to the ozonolysis reactions in carbonate solutions.^{234, 235}

These studies demonstrate that the use of high concentrations of complexing, weak-field ligands can shift the oxidation potential of Tb and Pr sufficiently to be accessible in aqueous conditions. However, the stability of the oxidized products varies widely depending on the nature of the coordination sphere. These shifts in redox potential imply a difference in stabilities of the trivalent species and the

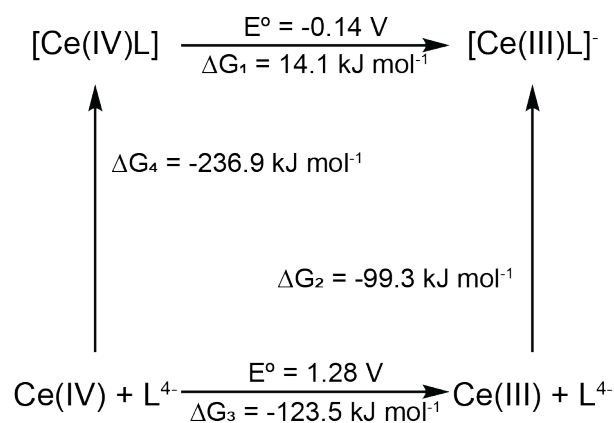


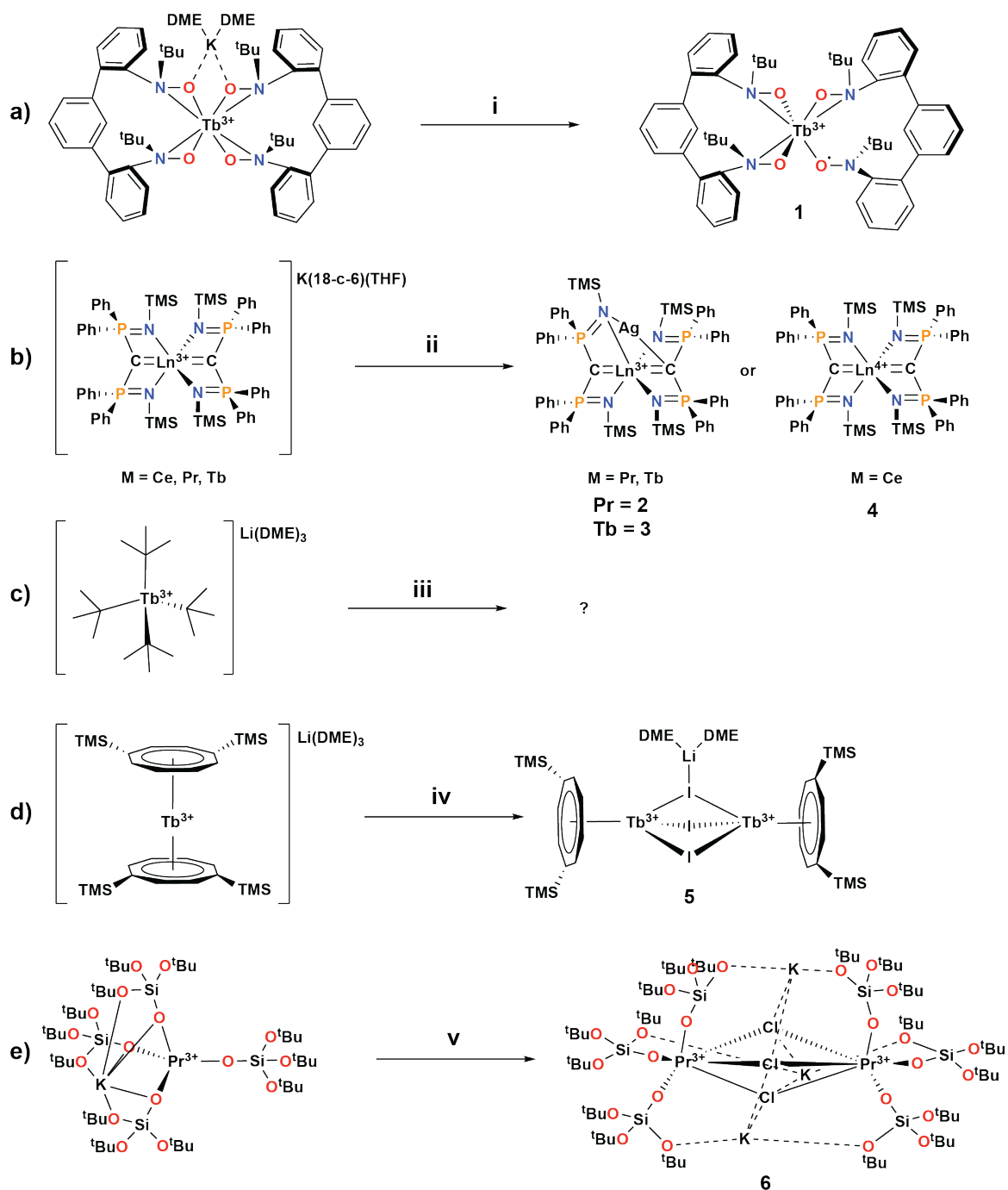
Figure 9. Thermodynamic cycle for the binding of 3,4,3-LI(1,2-HOPO) to Ce^{3+} and Ce^{4+} . Figure adapted from 245.

tetravalent species that is dependent on coordination environment and their effective concentration. Even for Ce, which is the most readily oxidizable lanthanide, oxidation in 1 M mineral acids is challenging, since the associated reduction potentials exceed the oxidation potential of water (1.23V vs. NHE). Expanding the scope of ligands beyond mineral acids to weak field, chelating ligands can shift the $\text{Ce}^{3+/4+}$ couple to a suitable range to stabilize the tetravalent ion in aqueous solution. For example, tetrakis(catecholate) Ce compounds, have a measured redox potential of -0.69 V vs. SCE, a shift of nearly 2.4 V from the free ion potential.²⁴⁴ If these chelating ligands are incorporated into a larger preorganized ligand, a larger shift is realized for the $\text{Ce}^{3+/4+}$ couple. Figure 9 depicts a thermodynamic cycle for an octadentate ligand system, 3,4,3-LI(1,2-HOPO).²⁴⁵ In the cycle, it is apparent the preference of the ligand for tetravalent cerium: the free energy change on complexation is -236.9 kJ mol^{-1} for the tetravalent versus only a change of -99.3 kJ mol^{-1} for the trivalent. The free energy of the reduction of free Ce^{4+} , ΔG_3 in Figure 9, can be calculated from the measured potential. Based on these values, the free energy of the reduction of complexed Ce^{4+} to complexed Ce^{3+} by Equation 5:

$$\Delta G_1 = \Delta G_3 - (\Delta G_4 - \Delta G_2) \quad (5)$$

From the free energy change, the expected shifted potential is calculated to be -0.14 V. The experimentally observed reduction potential for this specific system is -0.021 ± 0.010 V which is in relatively good agreement with the estimate. Based on this argument, it is reasonable to conclude that a strongly donating, oxidatively stable ligand can shift the redox potential through two modes: (1) by destabilizing the trivalent state, and in turn increasing ΔG_2 , and (2) by stabilizing the tetravalent state, resulting in a decrease in ΔG_4 . Although, the shift in oxidation potential with this macrochelate was unable to afford isolation of a tetravalent Pr or Tb complex from an aqueous environment, it was able to stabilize tetravalent Bk.²⁴⁶ The stability of Bk^{4+} in this coordination environment has been capitalized on to develop a redox-based separation method for Bk^{4+} .²⁴⁷

ARTICLE



Scheme 1. Documented synthetic attempts to form molecular Pr^{4+} and Tb^{4+} complexes. i) $[\text{Ag}][\text{OTf}]$ ($\text{OTf} = \text{triflate}$) in dichloromethane (DCM). ii) $[\text{Ag}][\text{BPh}_4]$ in toluene iii) O_2 , $[\text{Ag}][\text{acac}]$ ($\text{acac} = \text{acetylacetonate}$), $[\text{Ag}][\text{Cl}]$, $[1,1'\text{-dimethylFc}][\{3,5\text{-(CF}_3\text{)}(\text{C}_6\text{H}_3)\}_2\text{B}]$ ($\text{Fc} = \text{ferrocene}$) in diethyl ether (Et_2O) iv) $[\text{Ag}][\text{I}]$ in toluene/dimethoxyethane (DME) v) $[\text{N}(\text{C}_6\text{H}_4\text{Br})_3][\text{SbCl}_6]$ in acetonitrile (MeCN).

ARTICLE

Based on this design strategy, a terephthalamide macrocyclic ligand with pendant arms was developed that is selective for tetravalent ions.²⁴⁸ While this ligand binds Th⁴⁺ with high thermodynamic stability ($K_{\text{eq}} = 1054$, $\log\beta_{110} = 53.7(5)$), it has a preference for the smaller Ce⁴⁺ ion ($\log\beta_{110} = 61(2)$). This high affinity for Ce⁴⁺ leads to a selective binding of Ce⁴⁺ over Ln³⁺ by a factor of 10²⁹. Direct measurement of the Ce^{3+/4+} couple was only possible using a hanging mercury drop electrode, and Pr³⁺ was used a surrogate to measure the binding affinity of the ligand for a trivalent lanthanide. Based on the observed $E_{1/2}$ (-0.454 vs SHE) and solution thermodynamic behavior of Ce⁴⁺, the binding constant for Ce³⁺ was estimated to be $\log\beta_{110} = 28.6$ using a thermodynamic cycle similar to that shown in Figure 9. Based on the thermodynamic cycle for this ligand and Ce⁴⁺, the authors predict that this ligand should be able to stabilize Am⁴⁺ in aqueous solution. The aqueous reduction potential of Am^{4+/3+} is predicted to be 2.62 V.²⁴⁹

7. Molecular Ln⁴⁺ Chemistry

The *in-situ* oxidations observed in aqueous solution have inspired several approaches to the isolation of tetravalent Pr and Tb complexes in organic solvents and inert atmospheres. Some of these efforts focused on utilizing the design principles that yielded large shifts in oxidation potential for Ce through the preferential stabilization of tetravalent oxidation states and destabilization of trivalent oxidation state.⁷⁸ For example, Lewis basic polydentate ligands have been developed to isolate tetravalent lanthanide complexes. In 2016, Schelter and co-workers attempted the oxidation of an anionic, bidentate, bis-phenylnitroxide Tb complex $[\text{Tb}^{3+}(\text{arene-dINOx})_2][\text{K}(18\text{-c-6})(\text{py})_2]$ ((arene-dINOx) = 1,3-bis(2'-tert-butylhydroxylaminoaryl)benzene, 18-c-6 = 18-crown-6, py = pyridine) with silver triflate after electrochemical results suggested potential metal oxidation (Scheme 1a).²⁵⁰ While the oxidation proceeded and yielded silver metal, the complex that was isolated was a neutral Tb³⁺ complex bearing a ligand radical (**1**). Liddle and co-workers developed a similar strategy using the BIPM^{TMS} ligand (BIPM^{TMS} = $[\text{C}(\text{Ph}_2\text{PNSiMe}_3)_2]^{2-}$).²⁵¹ They prepared anionic bis-carbene lanthanide complexes supported by outer sphere potassium ions, $[\text{Ln}^{3+}(\text{BIPM}^{\text{TMS}})_2][\text{K}(18\text{-c-6})(\text{THF})_2]$ (where Ln = Ce, Pr, and Tb, THF = tetrahydrofuran), and examined their reactions with silver tetraphenylborate. While oxidation to the tetravalent state was successful for Ce to produce $[\text{Ce}^{4+}(\text{BIPM}^{\text{TMS}})_2]$ (**4**), the attempted oxidations at Pr and Tb instead formed an inner sphere silver adduct (Pr = **2**, Tb = **3**), $[\text{Ln}^{3+}(\text{BIPM}^{\text{TMS}})_2][\text{Ag}]$, and dropped $[\text{K}][\text{BPh}_4]$ (Ph = phenyl) (Scheme 1b).

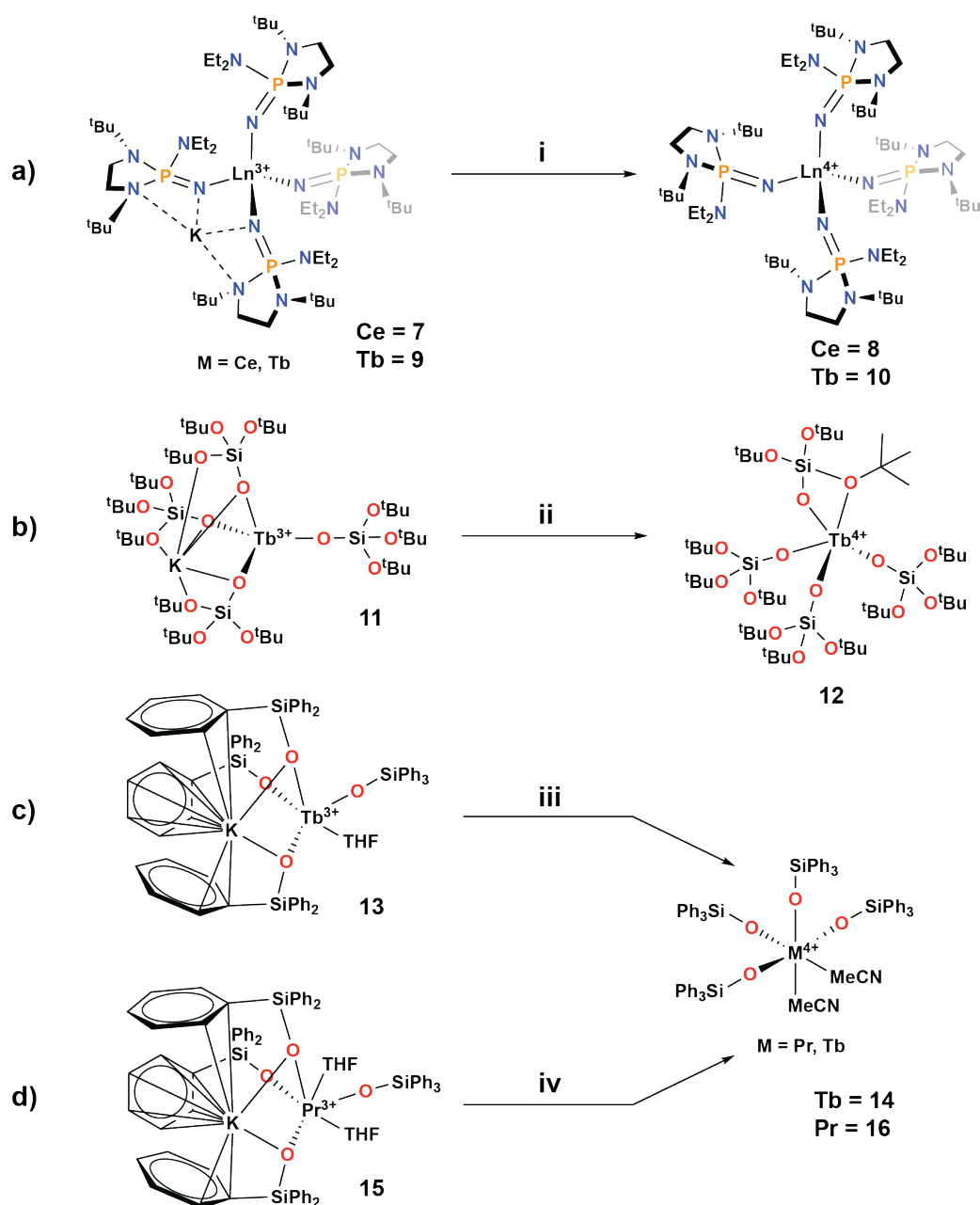
Attempts to isolate organometallic tetravalent Pr and Tb complexes have also been pursued. In 2007, Girolami and co-

workers attempted the oxidation of a tetrahomoleptic tetrakis-*tert*-butyl terbium complex, $[\text{Tb}^{3+}(\text{tBu})_4][\text{Li}(\text{DME})_3]$ (tBu = *tert*-butyl, DME = dimethoxyethane), with O₂, silver acetate, silver chloride, and 1,10-dimethylferrocenium tetrakis[3,5-bis(trifluoromethyl)phenyl]borate ($\{3,5\text{-}(\text{CF}_3)(\text{C}_6\text{H}_3)\}_4\text{B}$) (Scheme 1c).²⁵² In all cases, the colorless solutions of Tb³⁺ turned yellow upon addition of oxidant. Addition of O₂ resulted only in identification of *iso*-butene and *iso*-butane by ¹H NMR and gas chromatography and no isolation of a new metal complex. Addition of the one-electron oxidants did not afford any evidence of a new/tetravalent product by ¹H NMR or any isolable metal species.

The terbecene analogs of cerocene, uranocene, and plutonocene were also targeted (important analytes for examining multiconfigurational behavior, *vide infra*).²⁵³⁻²⁵⁷ Edlmann and co-workers attempted to make the terbecene derivative $[\text{Tb}^{4+}(\text{COT}'')_2]$ (COT'' = [1,4-bis(trimethylsilyl)cyclooctatetraene]²⁻), through the oxidation of $[\text{Tb}^{3+}(\text{COT}')_2][\text{Li}(\text{DME})_3]$ with silver iodide.²⁵⁸ While the solution turned yellow and a grey suspension was observed (Ag⁰), only a trivalent tris(μ -iodido)-bridged di-nuclear half sandwich complex, $[\text{Tb}_2(\mu\text{-I})_3(\text{COT}'')_2][\text{Li}(\text{DME})_2]$ (**5**) was isolated (Scheme 1d). These approaches are important benchmarks for the advancement of the field of molecular tetravalent lanthanides and help to build a thorough database of ligand types and synthetic methods necessary for the stabilization of molecular tetravalent lanthanide complexes.

In 2019, the first three isolable molecular Tb⁴⁺ complexes were reported, supported by weak-field ligand frameworks featuring N and O donors in the form of imidophosphoranes and siloxides, respectively. Leaning on the tunability of the Ln^{3+/4+} couple through ligand field, in each system, oxidation and isolation of a molecular tetravalent Tb complex is achieved through use of commercial oxidants demonstrating a much lower oxidation potential than the measured/calculated potential for a free Tb ion.²²⁹ The La Pierre group isolated a tetravalent Tb complex in a tetrahomoleptic imidophosphorane ligand field, employing the ligand $[\text{NP}^*]^{-1}$, $[(\text{NP}(1,2\text{-bis-}^t\text{Bu-diamidoethane})(\text{NET}_2))]^{-1}$. Imidophosphoranes are strongly donating, 1σ , 2π weak field ligands. The isolation of tetravalent Tb was anticipated based on the observed redox chemistry of the $[\text{Ce}(\text{NP}(\text{pip})_3)_4]$ complex (pip = piperidiny). With Ce in the imidophosphorane ligand field, $[\text{NP}(\text{pip})_3]^{-1}$, the oxidation potential for the Ce³⁺ complex, $[\text{K}(\text{Et}_2\text{O})_2][\text{Ce}(\text{NP}(\text{pip})_3)_4]$, was shifted to less than -2.64 V vs. Fc/Fc⁺ (Fc = ferrocene) and predicted to be -2.99 V, 3.5 and 3.9 V shifts, respectively, from that of the free ion. These theoretical values were validated through electrochemical measurements of the analogous, but more sterically encumbered complexes, $[\text{Ce}^{3+}(\text{NP}(1,2\text{-bis-}^t\text{Bu-}$

ARTICLE



Scheme 2. Successful syntheses of Tb^{4+} complexes and Pr^{4+} complex to date. i) $[\text{Ag}][\text{I}]$ in Et_2O ii) $[\text{N}(\text{C}_6\text{H}_4\text{Br})_3][\text{SbCl}_6]$ in THF iii) $[\text{N}(\text{C}_6\text{H}_4\text{Br})_3][\text{X}]$ where $\text{X} = \text{SbCl}_6^-$ or OTf^- in MeCN iv) $[\text{N}(\text{C}_6\text{H}_4\text{Br})_3][\text{SbCl}_6]$ in MeCN.

diamidoethane)(NEt_2) $_4$) (**7**) ($E_{\text{pc}} = -2.88$, $E_{\text{pa}} = -2.44$ V vs Fc/Fc^+ ($E_{\text{pc}} =$ cathodic peak, $E_{\text{pa}} =$ anodic peak) and $[\text{Ce}^{4+}(\text{NP}(1,2\text{-bis-}^t\text{Bu-diamidoethane})(\text{NEt}_2)_4)]$ (**8**) ($E_{\text{pc}} = -2.86$, $E_{\text{pa}} = -1.63$ V vs Fc/Fc^+).²⁵⁹ These $\text{Ce}^{3+/4+}$ couples are the most negatively shifted potentials from that of the free ion to-date (2.5 mM analyte, 0.1

M $[(^n\text{Bu})_4\text{N}][\text{PF}_6]$ ($^n\text{Bu} =$ normal-butyl) in THF, 200 mV/s scan rate).

The tetravalent, tetrahomoleptic Tb species was synthesized through oxidation of the anionic trivalent precursor, $[\text{K}][\text{Tb}^{3+}(\text{NP}(1,2\text{-bis-}^t\text{Bu-diamidoethane})(\text{NEt}_2)_4)]$ (**9**),

with silver iodide in diethyl ether (Scheme 2a). Electrochemical measurements demonstrate that the $Tb^{3+/4+}$ oxidation potential for the trivalent complex is $E_{pa} = -0.64$ V vs Fc/Fc^+ (200 mV/s, 3 mM analyte, 0.1 M [$^{n}Bu_4N$][PF_6] in THF, 200 mV/s scan rate), shifted 2.9 V from that of the free ion, while the $E_{pc} = -1.79$ V vs Fc/Fc^+ .²⁵⁹ The E_{pa} for the Tb^{4+} complex, [$Tb^{4+}(NP(1,2-bis-^tBu-diamidoethane)(NEt_2)_4)$] (**10**), was more negative at -0.95 V while the E_{pc} was -1.68 V vs Fc/Fc^+ (Table 4).

Mazzanti and co-workers have reported two tetravalent terbium complexes in siloxide ligand frameworks. The first reported complex was achieved through oxidation of [$K[Tb^{3+}(OSi(O^tBu)_3)_4]$] (**11**) with magic blue, [$N(C_6H_4Br)_3][SbCl_6]$], in acetonitrile to give [$Tb^{4+}(OSi(O^tBu)_3)_3(\kappa_2-OSi(O^tBu)_3)$] (**12**) (Scheme 2b).²⁶⁰ The second was achieved through oxidation of [$K[Tb^{3+}(OSiPh_3)_4(THF)]$] (**13**) with magic blue in acetonitrile to afford [$Tb^{4+}(OSiPh_3)_4(MeCN)_2$] (**14**) ($MeCN =$ acetonitrile).²⁶¹ Electrochemical measurements for **12** place the oxidation potential at $E_{pa} = 0.85$ V and the reduction potential $E_{pc} = -0.19$ V vs Fc/Fc^+ (2 mM analyte, 0.1 M [$^{n}Bu_4N$][$B(C_6F_5)_4$], 250 mV/s scan rate). Electrochemical measurements on the Tb^{3+} complex, **11**, were not reported. The tris-phenylsiloxide ligand framework stabilizes the tetravalent state to a larger degree than the *tert*-butoxy siloxide ligand framework. Electrochemical measurements for **13** place the E_{pa} at 0.44 V and the E_{pc} at -0.23 V vs Fc/Fc^+ (2 mM analyte, 0.1 M [$^{n}Bu_4N$][$B(C_6F_5)_4$] in THF, 250 mV/s scan rate).²⁶¹ Measurements for **14** place the oxidation potential at $E_{pa} = 0.49$ V and the reduction potential $E_{pc} = -0.99$ V vs Fc/Fc^+ . Both tetravalent complexes decompose in THF and characterization in THF is performed immediately after dissolution. In contrast, complexes **9** and **10** are stable in THF in anaerobic conditions.

Table 4. Peak potentials for isolated Tb and Pr complexes and their isostructural Ce complexes versus Fc/Fc^+ .

Compound	E_{pc} (V)	E_{pa} (V)
[$K[Ce^{3+}(NP(1,2-bis-^tBu-diamidoethane)(NEt_2)_4)]$, 7 ²⁵⁹	-2.88	-1.44
[$Ce^{4+}(NP(1,2-bis-^tBu-diamidoethane)(NEt_2)_4)$, 8 ²⁵⁹	-2.86	-1.63
[$K[Tb^{3+}(NP(1,2-bis-^tBu-diamidoethane)(NEt_2)_4)]$, 9 ²⁵⁹	-1.79	-0.64
[$Tb^{4+}(NP(1,2-bis-^tBu-diamidoethane)(NEt_2)_4)$, 10 ²⁵⁹	-1.68	-0.95
[$Ce^{4+}(OSi(O^tBu)_3)_3(\kappa_2-OSi(O^tBu)_3)$] ²⁶⁰	-1.72	-0.19
[$Tb^{4+}(OSi(O^tBu)_3)_3(\kappa_2-OSi(O^tBu)_3)$, 12 ²⁶⁰	-0.70	0.85
[$K[Ce^{3+}(OSiPh_3)_4(MeCN)_2]$] ²⁶¹	-1.84	-0.55
[$K[Tb^{3+}(OSiPh_3)_4(THF)]$, 13 ²⁶¹	-0.23	0.44
[$Tb^{4+}(OSiPh_3)_4(MeCN)_2$, 14 ²⁶¹	-0.99	0.49
[$K[Pr^{3+}(OSiPh_3)_4(THF)]$, 15 ²⁶²	-0.59	0.71
[$Pr^{4+}(OSiPh_3)_4(MeCN)_2$, 16 ²⁶²	-0.50	0.72

In 2020, Mazzanti and co-workers reported isolation of the first tetravalent Pr complex using the *tris*-phenylsiloxide ligand framework. The tetravalent complex was synthesized through oxidation of the anionic [$K[Pr^{3+}(OSiPh_3)_4(THF)_3]$] (**15**) with magic blue in acetonitrile (Scheme 2c).²⁶² The tetravalent product, [$Pr^{4+}(OSiPh_3)_4(MeCN)_2$] (**16**) is brown. Isolation of this complex,

however, proved more technically difficult than that of the Tb complex. The product could only be isolated if, immediately after addition of oxidant, the volatiles were removed under vacuum and then fresh acetonitrile added to the residue. The *tert*-butoxy siloxide ligand, used previously to isolate tetravalent Tb by the authors, proved incapable of stabilizing tetravalent praseodymium and only the decomposition product, [$\{Pr^{3+}(OSi(O^tBu)_3)_3\}_2(\mu-Cl)_3(\mu-K)_3$] (**6**) could be isolated (Scheme 1e).²⁶²

Cyclic voltammetry of the Pr^{4+} complex, **16**, demonstrated that the E_{pc} and E_{pa} were -0.50 V and 0.72 V, respectively, vs Fc/Fc^+ (2 mM analyte, 0.1 M [$^{n}Bu_4N$][$B(C_6F_5)_4$] in THF, 250 mV/s scan rate). Electrochemical measurements of the Pr^{3+} complex, **15**, placed the E_{pc} and E_{pa} at -0.59 and 0.71 V vs Fc/Fc^+ under the same conditions, showing little change in the reduction potential as a result of the counteraction (Table 4).²⁶² These oxidation potentials are very close to the reported $E_{1/2}$ for magic blue (0.67 V vs Fc/Fc^+ in $MeCN$). The oxidation potential for the Pr^{3+} complex was 0.27 V more positive than that of the analogous Tb^{3+} (0.44 V) complex in line with the predicted difference, ~ 0.2 V, in oxidation potentials for trivalent Pr and Tb.²²⁹ Similar to the two tetravalent Tb siloxide complexes, **16** readily decomposes in THF and all characterization in THF was performed immediately after dissolution.

Electrochemical potentials of Ce in the identical ligand environments as those of isolated Pr and Tb compounds provide an avenue for predicting what existing trivalent Pr and Tb compounds could potentially be oxidized or even isolated in the tetravalent oxidation state. For example, in the La Pierre group's Ce^{4+} imidophosphorane system, **8**, the E_{pc} and E_{pa} are -2.86 and -1.63 V vs Fc/Fc^+ (2.5 mM analyte, 0.1 M [$^{n}Bu_4N$][PF_6] in THF, 200 mV/s scan rate).²⁵⁹ For the Ce^{3+} complex, **7**, the E_{pc} and E_{pa} are -2.88 and -1.44 V vs Fc/Fc^+ under the same conditions. Although less negative but still greatly shifted from that of the free ion, the Ce compound, [$Ce^{4+}(OSi(O^tBu)_3)_3(\kappa_2-OSi(O^tBu)_3)$], analogous to the Tb^{4+} system, **12**, by Mazzanti and co-workers has an $E_{pc} = -1.72$ and $E_{pa} = -0.19$ V vs Fc/Fc^+ (2 mM analyte, 0.1 M [$^{n}Bu_4N$][$B(C_6F_5)_4$] in THF, 250 mV/s scan rate).²⁶⁰ In the phenyl siloxide ligand field for [$K[Ce^{3+}(OSiPh_3)_4(MeCN)_2]$], the E_{pc} and E_{pa} were measured to be -1.84 and -0.55 V vs Fc/Fc^+ (2 mM analyte, 0.1 M [$^{n}Bu_4N$][$B(C_6F_5)_4$] in THF, 250 mV/s scan rate). Thus, we expect that complexes with very negatively shifted redox potentials at Ce, could have observable redox events at Tb using the same ligand field and possibly even lead to isolable complexes.

For example, for **4**, mentioned earlier, the E_{pc} and E_{pa} are approximately -1.9 and -1.4 V vs Fc/Fc^+ respectively (2 mM analyte, 0.1 M [$^{n}Pr_4N$][$\{3,5-(CF_3)_2(C_6H_3)_4\}B$] ($^{n}Pr =$ normal propyl) in THF, 200 mV/s scan rate (exact E_{pa} and E_{pc} values not reported and taken as estimate from graphical representation).²⁵¹ The reported value for the redox event is $E_{1/2} = -1.63$ V. While silver tetraphenylborate did not prove itself a fruitful reagent in the case of [$Pr^{3+}(BIPM^{TMS})_2$][$K(18-c-6)(THF)_2$] and [$Tb^{3+}(BIPM^{TMS})_2$][$K(18-c-6)(THF)_2$], more oxidizing reagents could potentially prove useful in this case. Additionally, Hayton and coworkers' Ce^{4+} hexahomoleptic ketimide complex, [$Li_2[Ce(N=C^tBuPh)_6]$], has an irreversible reduction event at $E_{pc} =$

-2.16 V vs. Fc/Fc⁺ (2 mM analyte, 0.1 M [(ⁿBu₄)N][BPh₄] in THF, 200 mV/s scan rate).²⁶³ Diaconescu and co-workers' have two similar Ce⁴⁺ complexes, employing Schiff base ligands with a ferrocene backbone, which have exceptionally negative redox potentials.²⁶⁴ The complex [Ce⁴⁺(L')(O^tBu)₂] (L' = 1,10-Di(2,4-bis-tert-butyl-salicylimino)ferrocene) has an E_{pc} = -2.07 and E_{pa} = -1.01 V vs Fc/Fc⁺ (1.5 mM analyte, 0.5 M [(ⁿPr₄)N][{3,5-(CF₃)(C₆H₃)₂}]₄B] in THF, 100 mV/s scan rate). At more negative potentials, the complex [Ce⁴⁺(L'')(O^tBu)₂] (L'' = 1,10-di(2-tert-butyl-6-diphenylphosphiniminophenol)ferrocene) has an E_{pc} = -2.39 and E_{pa} = -1.70 V vs Fc/Fc⁺. And lastly, Schelter and co-workers' nitronyl nitroxide Ce⁴⁺ complex, [Ce(2-(^tBuNO)py)₄] (^tBuNO)py = N-tert-butyl-N-2-pyridyl nitroxide) has very negative peak potentials of E_{pc} = -2.09 and E_{pa} = -1.80 for a reported E_{1/2} = -1.95 V vs Fc/Fc⁺ (0.1 M [(ⁿPr₄)N][{3,5-(CF₃)(C₆H₃)₂}]₄B] in DCM (DCM = dichloromethane)).²⁶⁵ We suggest that Tb complexes of these ligands may, at the very least, present observable redox features by cyclic voltammetry. This prediction, however, will not necessarily hold true for every Ce/Tb isostructural pair even with sufficiently negative redox potentials at Ce. For example, despite the negatively shifted potentials for the Ce complex, [Ce⁴⁺(arene-diNOx)₂], oxidation of [Tb³⁺(arene-diNOx)₂][K(18-c-6)(py)₂] with a relatively mild oxidant of [Ag][OTf] resulted in ligand oxidation and rearrangement to form **1**.²⁵⁰ This observation indicates an important point: oxidation potential of the isostructural Ce complex is not the sole criterion for the observation of an oxidation of trivalent Pr and Tb complexes. Features of ligand architecture are also likely important including the architecture to minimize rearrangement during oxidation, the relative donor properties, and the absence of ligand redox events.

We expect that the above tetravalent Ce compounds, and likely more than those explicitly mentioned here, with oxidation potentials more negative than -0.2 V vs Fc/Fc⁺ as observed by CV, may have analogous Tb complexes that have observable redox events within the organic solvent window by CV.²⁶⁶⁻²⁶⁸ The accessibility of a Tb oxidation event is, in turn, defined by the oxidation potential of the chemical oxidant and the reagent's compatibility with the solvent. To-date, magic blue is the strongest oxidant employed. Conceivably, the suggested E_{pa} cut-off value could be pushed to 0 V vs Fc/Fc⁺ but would require stronger oxidants such as [NO][BF₄], which is known to react with ethereal solvents.²⁶⁹

This guideline is based on the observed difference between the oxidation potentials for the two Ce and Tb pairs for the imidophosphorane and *tert*-butoxy siloxide ligand fields. Specifically, the difference in E_{pa} for the imidophosphorane Ce and Tb complexes was 0.68 V vs Fc/Fc⁺ while for the *tert*-butoxy siloxide, it was 1.0 V. Thus, estimating the oxidation potential of Tb to be 1.0 V from that of the analogous Ce⁴⁺ complex is a reasonable estimate for the Tb⁴⁺ oxidation potential. With more Tb⁴⁺ complexes likely on the verge of discovery, this range can be further refined. Although most of the complexes discussed here are neutral Ce⁴⁺ complexes, we would argue that for anionic trivalent Ce complexes, analysis by cyclic voltammetry is likely more insightful as those potentials would take into account cation effects which can have a large impact on the

driving force for oxidation.^{259, 270, 271} While the shift in oxidation potential at Tb is important to ensure it is accessible with chemically compatible oxidants, merely shifting the oxidation potential within a reasonable window does not guarantee an isolable or bench stable complex.

The physical characterization of these novel molecular complexes of Pr⁴⁺ and Tb⁴⁺ included SC-XRD, magnetometry, and UV/vis/NIR, EPR, and L₃-edge spectroscopies. The structural comparison of the tetravalent complexes is described here and the other characterization modalities are broken out in subsequent sections to facilitate comparison to solid-state data. Changes in M-L bond length upon changes in metal oxidation state are generally well correlated with the size difference of the ionic radius of the metal in each oxidation state. In the lanthanides, changes in ionic radii can be quite large in comparison to the transition metals. Thus, changes in Ln-L bond lengths are direct indicators of redox events at a lanthanide ion. The ionic radius for Ce⁴⁺ is 0.87 Å, 0.14 Å smaller than Ce³⁺, the ionic radius for Pr⁴⁺ is 0.85 Å, 0.14 Å smaller than Pr³⁺, and the ionic radius for Tb⁴⁺ is 0.76 Å, 0.16 Å smaller than Tb³⁺.²⁷² Thus a 0.14 – 0.16 Å contraction is expected on oxidation. It should be noted that Ce⁴⁺ and Pr⁴⁺ are significantly larger than Tb⁴⁺ by 0.09 – 0.11 Å, thus the structural chemistry of tetravalent Ce is not necessarily a direct model of Tb⁴⁺ structural phenomena.

The Tb³⁺ complex, **9**, is pseudotetrahedral with an inner sphere potassium atom which is 4-coordinate and bound by two of the imidophosphorane ligands.²⁷³ The largest structural rearrangement upon oxidation is in the contraction of the Tb-N bond distances by 0.13 Å and 0.16 Å for the potassium bound and terminal ligands, respectively, consistent with a change in metal oxidation state from Tb³⁺ to Tb⁴⁺. The tetravalent complex, **10**, is also four-coordinate with S₄ symmetry. This change in Ln-N bond length is echoed in the isostructural Ce complexes. Upon oxidation, the Ce-N bond lengths contract by 0.14 Å and 0.08 Å for the potassium bound and terminal ligands respectively, consistent with the change in ionic radius from Ce³⁺ to Ce⁴⁺.²⁵⁹

Since the **8** and **10** are homoleptic and isotopic, a Voronoi-Dirichlet Polyhedra (VDP) analysis was pursued to quantify the changes in the coordination sphere introduced by the 0.11 Å difference in metal ion size between Ce and Tb.^{259, 274, 275} This analysis revealed that the secondary coordination sphere – the alkyl hydrogens – is much less accessible to the metal in the Tb complex than in the Ce complex. This finding emphasizes that ligand interactions with the metal and in the second coordination sphere are important considerations for the isolation of molecular Ln⁴⁺ complexes.

The analysis of Tb⁴⁺ siloxide complexes is a bit more complex, since the coordination numbers change in the redox process and complexes are heteroleptic. Nonetheless, similar trends are seen in the Tb-O bond length contractions that were seen with the imidophosphorane complex. In the trivalent terbium complexes with siloxide ligand fields, the coordination number is four in the trivalent oxidation state for **11**²⁶⁰ and five for **13**²⁶¹ (four ligands and one solvent molecule). Upon oxidation, **11** undergoes a structural rearrangement and one of the *tert*-butoxy arms of the *tert*-butoxy siloxide coordinates to

the metal ion for a total coordination number of five and a distorted trigonal bipyramidal geometry. The average Tb–O distance in **11** is 2.130(2) Å for the three potassium bound ligands and 2.103(3) Å for the terminal ligand. Upon oxidation and release of the potassium ion, the average Tb–O bond length is 2.044(3) Å in **12**, a 0.09 Å and 0.06 Å contraction in bond length for the potassium bound ligands and terminal ligand, respectively. These contractions are smaller than expected based on the change in ionic radii, but consistent with the change in oxidation state to Tb⁴⁺. In the case of **13**, the one THF molecule is replaced by two acetonitrile molecules for a total coordination number of six in **14** and a distorted octahedral geometry. The bond length shortening in **14** is on average 0.13 Å and 0.08 Å from 2.194(2) and 2.140(2) for the bound and terminal ligands respectively to 2.060(5) Å, consistent with the increase in oxidation state.

Similarly, the solid-state characterization of the Pr complexes by SC-XRD agrees well with the assignment of Pr⁴⁺. The trivalent complex, **15**, is six-coordinate (four ligands, two THF molecules) while **16** is also six coordinate and both have distorted octahedral geometries.²⁶² The average Pr–O bond lengths are 2.292(8) Å and 2.258(8) Å for the potassium bound and terminal ligands respectively. The average Pr–O bond distance in **16** is shortened to 2.104(4) Å a difference of 0.19 Å and 0.15 Å for the potassium bound and terminal ligands respectively. This contraction is slightly but consistent with the change in ionic radius from Pr³⁺ to Pr⁴⁺.

What is clear from a comparison of the potentials for existing Pr and Tb compounds is that the shift of the M^{3+/4+} couple to an oxidatively achievable window alone is not sufficient to ensure bench stability of tetravalent complexes. A number of factors must be considered in order to isolate stable Ln⁴⁺ complexes. These factors include, shift of the metal redox potential from that of the free ion (which is affected by the ligand donor properties), the degree of ligand reorganization upon oxidation, and the oxidative stability of the ligand.

8. Core-Level Spectroscopy

XAS is an element specific technique and provides direct evidence for oxidation state via XANES, metal-ligand bond covalency via ligand K-edge XAS, and the coordination environment and bond lengths of the atom of interest via X-ray absorption fine structure (XAFS). Most germane to our discussion of electronic structure are metal L- and M-edge XAS and ligand K-edge XAS techniques.

Lanthanide L-edge XANES. L-edge XANES can provide direct evidence for lanthanide oxidation state, particularly when the absorbing atom is within a conserved coordination environment. When the latter requirement is met, the absorption edge energy increases with increasing formal oxidation state since the nucleus is less shielded and has a higher effective charge. Thus, as the metal oxidation state is increased, from Ln²⁺ to Ln³⁺ to Ln⁴⁺, within a conserved coordination environment, the absorption edge moves to higher energy.⁵⁵ The step from divalent to trivalent is typically 7–8 eV and the step from trivalent to tetravalent is 1–2 eV.^{259, 271, 273, 276–278} This pattern holds true except for the comparison of

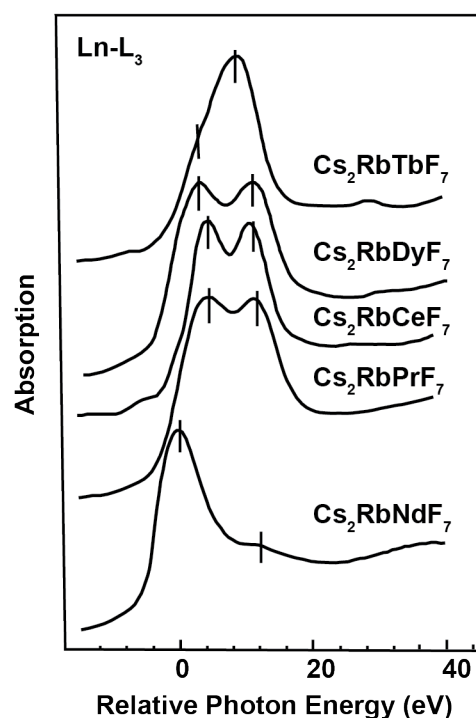


Figure 10. L₃-edge XANES spectra for extended solids Cs₂RbLn⁴⁺F₇ (Ln=Tb, Dy, Ce, Pr, Nd) exhibiting doublet white line features. Figure adapted from reference 293.

the L₃-edge spectra of trivalent lanthanides and non-traditional divalents.⁵⁵ As described in the introduction, non-traditional divalents take on a 4fⁿ5d¹ ground state. As a result, the non-traditional divalent ions have an absorption edge nearly identical to that of their trivalent counterpart. This insensitivity of the excitation energy (0.2–1.9 eV) to the change in valence has been attributed to limited sensitivity of the core 2p orbitals to the occupation of the 5d.⁵⁵ On the other hand, the energy of the 2p orbitals are strongly sensitive (7–8 eV) to changes in the occupation of the 4f orbitals (Ln³⁺, 4fⁿ vs. Ln²⁺, 4fⁿ⁺¹).

In addition to a change in the relative energy of the white line, the shape of the white line changes upon oxidation to a tetravalent ion. While the absorption spectra of Ln²⁺ and Ln³⁺ complexes are characterized by single white line features, those of Ln⁴⁺ complexes are defined by multi-peak white line features, usually in the form of a white line doublet. Additionally, spectra of tetravalent ions typically have a weak pre-edge feature, which has been attributed to a quadrupole allowed 2p_{3/2} → 4f transition, and has been described as a consequence of the emergence of covalent bonding between orbitals of p character in the ligand and 4f character in the lanthanide.^{279–281} It should be noted that, to-date, no molecular series has been evaluated across all three oxidation states in similar or identical ligand fields.

L₃-edge spectra have been used to unequivocally confirm the tetravalent oxidation state of Ce,^{279, 282–296} Pr,^{286, 293, 295–297} Nd,²⁹³ Tb,^{293–296, 298} and Dy^{193, 293} compounds in the solid state and Ce^{253, 254, 265, 271, 276, 278, 299–301} and Tb²⁷³ in molecular complexes. In all cases, a white line doublet (or higher order) feature is observed and confirms the existence of the tetravalent oxidation state. However, a notable difference

ARTICLE

Table 5. n_f values and fitting peak energies for the L_3 -edge XANES spectra of selected Ce, Pr, and Tb compounds.

Ln^{4+} Compound	n_f	$4f^{n+1}$ (eV)	$4f^n$ (eV)
$[\text{Ce}^{4+}(\text{NP}(\text{pip})_3)_4]^{271}$	0.38(2)	5728.91(8), 5725.67(3)	5735.96(3)
$[\text{Ce}^{4+}(\text{NP}(1,2\text{-bis-}^t\text{Bu-diamidoethane})(\text{NEt}_2)_4)]^{259}$	0.40(4)	5730.44(9), 5726.45(8)	5736.57(6)
$[\text{Ce}(\text{trop})_4]^{299}$	0.50(3)	5728.2(3)	5736.0(3)
$[\text{CeCl}_6]^{2-276}$	0.51(5)	5720-5734 (3 peaks, n.d.)	5734-5742 (2 peaks, n.d.)
$[\text{Ce}(\text{acac})_4]^{299}$	0.51(3)	5727.9(3)	5735.9(3)
CeO_2^{296}	0.56(4)	5728.0(1)	5736.2(2)
$[\text{Ce}(\text{tmtaa})_2]^{299}$	0.59(3)	5726.8(3)	5735.6(3)
$[\text{Ce}(\text{C}_8\text{H}_8)]^{254}$	0.82(3)	5725.0(3)	5736.5(3)
$[\text{Tb}^{4+}(\text{NP}(1,2\text{-bis-}^t\text{Bu-diamidoethane})(\text{NEt}_2)_4)]^{273}$	0.39(4)	7520.30(3)	7528.50(3)
TbO_2^{296}	0.42(4)	7518.9(1)	7526.1(1)
PrO_2^{296}	0.64(4)	5968.4(1)	5977.7(2)

n.d. stands for not defined in the original text

between some compounds is in the shape and peak splitting of the white line doublet. For example, in $\text{Cs}_2\text{RbLn}^{4+}\text{F}_7$ ($\text{Ln} = \text{Ce}, \text{Pr}, \text{Nd}, \text{Dy}, \text{Tb}$), the shape of the spectra for Nd and Tb diverge from the rest (Figure 10).^{293, 298} While the two peaks appear to be about a 50/50 contribution in the white line feature for Ce, Pr, and Dy, in the Tb spectrum, the lower energy feature of the white line doublet has a much lower intensity when compared to the higher energy feature and vice versa for Nd. This decreased intensity has also been observed in L_3 -edge spectra of TbO_2 and TbF_4 .^{286, 294-296} Additionally, in molecular complexes of Ce this variability in peak structure has been observed over a large range of complexes and relative peak intensities (Table 5).^{253, 254, 265, 271, 276, 278, 299-301}

Two competing hypotheses for the origin of the doublet white line feature for tetravalent complexes have been advanced: either a ground state or a final state effect. The dipole allowed transition probed at the L_3 -edge is from the metal $2p$ orbitals to unoccupied states with metal $5d$ character, $2p^6 4f^n 5d^0 \rightarrow 2p^5 4f^{n+1} 5d^1$, where n corresponds to the number of f electrons in the ground state. The ground state theory invokes the existence of two ground states, both the $\text{Ln}^{4+} 2p^6 4f^n 5d^0 \text{L}$ and an $\text{Ln}^{3+} 2p^6 4f^{n+1} 5d^0 \underline{\text{L}}$ (where L is a full ligand orbital and $\underline{\text{L}}$ is a ligand hole), which have the final states $2p^5 4f^{n+1} 5d^1 \text{L}$ and $2p^5 4f^{n+1} 5d^1 \underline{\text{L}}$, respectively resulting in the multipeak feature. The other scenario suggests that a single ground state exists, $2p^6 4f^n 5d^0 \text{L}$, and that the peak splitting observed in the white line feature is a result of transitions to the unoccupied $5d$ states, which are split by the crystal field.

Numerous studies have sought to answer this question on the origin of the white line multipeak feature. Pressure dependence studies on PrO_2 in 1994 show that with increasing pressure, the intensity of the $2p^5 4f^{n+1} 5d^1 \underline{\text{L}}$ (Pr^{3+}) contribution to the white line doublet increases.²⁹⁷ The authors claim that is a

result of increased covalency between the $2p$ and $4f$ orbitals at higher pressures. If the lower energy feature were one of mixed valent origins, this change in relative intensity would not be observed, therefore confirming a multiconfigurational ground state. These results were similar to those observed in CeO_2 in 1988.²⁸⁴ More recent studies explain the multiconfigurational ground state through a complementary approach on Ce^{4+} complexes. Magnetic susceptibility studies have been performed on cerocene ($[\text{Ce}^{4+}(\text{C}_8\text{H}_8)_2]$), $[\text{Ce}^{4+}(\text{acac})_4]$, $[\text{Ce}^{4+}(\text{trop})_4]$, and $[\text{Ce}^{4+}(\text{tmtaa})_2]$ and show that these four formally $4f^0$ complexes exhibit TIP with $\chi_0 > 0$.^{254, 299} Additionally, for $[\text{Ce}^{4+}(\text{acac})_4]$, $[\text{Ce}^{4+}(\text{trop})_4]$, and $[\text{Ce}^{4+}(\text{tmtaa})_2]$, Complete Active Space Self-Consistent Field (CASSCF) calculations demonstrate that the TIP behavior is correlated to the small energy difference between the ground state (open shell singlet, $f^1 \underline{\text{L}}$) and the first excited state (open shell triplet, $f^1 \text{L}$).²⁹⁹ Further studies of cerocene at the Ce $M_{5,4}$ -edges and configuration interaction (CI) calculations to model the spectra also provide evidence for a multiconfigurational ground state, discussed below in the M-edge section.³⁰²

In light of these studies demonstrating multiconfigurational behavior at tetravalent Ce, the L_3 -edge spectra of tetravalent lanthanides may be fit to determine the relative contribution of each configuration to the ground state. In particular, weighting the $2p^5 4f^{n+1} 5d^1 \underline{\text{L}}$ intensity to the total observed intensity is described by an n_f value, which provides a quantitative measure to compare between different systems. Using the common two-peak model, the n_f value is defined in Equation 6:

$$n_f = \frac{A_{\text{Ln}^{3+}}}{A_{\text{Ln}^{3+}} + A_{\text{Ln}^{4+}}} \quad (6)$$

where $A_{\text{Ln}^{3+}}$ is the intensity of the $2p^5 4f^{n+1} 5d^1 \underline{\text{L}}$ contribution and $A_{\text{Ln}^{4+}}$ is the intensity of the $2p^5 4f^n 5d^1 \text{L}$ contribution to the white

ARTICLE

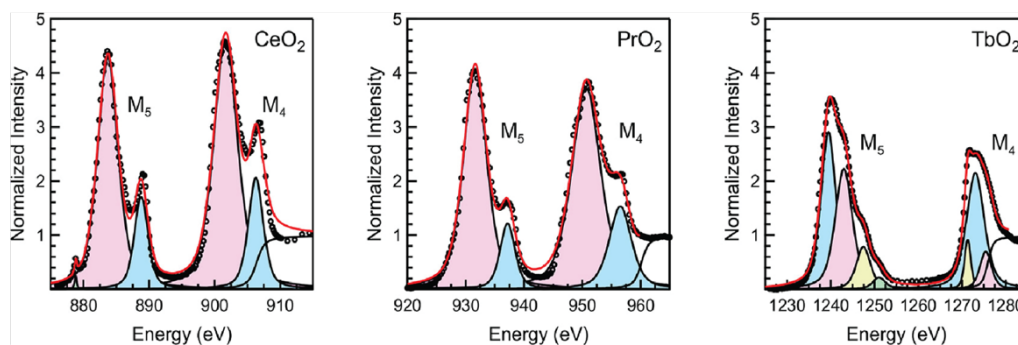


Figure 11. Curve fit Ln $M_{5,4}$ -edge spectra for binary oxides of Ce, Pr, and Tb. Reprinted with permission from S. G. Minasian, E. R. Batista, C. H. Booth, D. L. Clark, J. M. Keith, S. A. Kozimor, W. W. Lukens, R. L. Martin, D. K. Shuh, S. C. E. Stieber, T. Tyliczszak and X.-d. Wen, *J. Am. Chem. Soc.*, 2017, **139**, 18052-18064. Copyright 2017 American Chemical Society (Ref.296).

line doublet. Thus, lower n_f values have a smaller $2p^54f^{n+1}5d^1L$ contribution to the ground state and vice versa.

However, in some cases, a two-peak model has proven to be insufficient. Compounds such as $[\text{CeCl}_6]^{2-}$, **8**,²⁵⁹ $\text{Cs}_2\text{RbDyF}_7$ and Cs_2KDyF_7 ,¹⁹³ PrO_2 ,²⁹⁷ and likely others all require the inclusion of more than two peaks to arrive at satisfactory fits. In cases such as these, comparison to the established two-peak model have been made by summing intensities of lower or higher energy features, although there is no physical basis established for this grouping. Additionally, there is some variability in the literature in the placement of the step-function which limits the ability to make quantitative comparisons between independent investigations. For example, ceria has been reported to have n_f values of 0.58(3)²⁹⁹, 0.56(4)²⁹⁶ and 0.5.²⁹⁵ However, keeping these factors in mind, n_f values are still useful for comparison.

The reported n_f value of Ce^{4+} complexes spans the range of 0.38(2) to 0.82(3) (Table 5). The range spans from **8**²⁵⁹ at 0.38(2), CeO_2 at 0.56(4), to cerocene at 0.82(3). Andersen, Booth, and co-workers note an important trend in the decrease of n_f value with the increasing electronegativity of the ligating atoms $\text{C} > \text{N} > \text{O}$. This trend holds true for most Ce complexes, however, does not appear to hold true for imidophosphorane complexes which have n_f values lower than complexes with O donor atoms. In the same work, it is noted that complexes with the lowest n_f value and χ_0 values have the highest energy peak maxima for the $2p^54f^n5d^1L$ transition (*i.e.* the Ln^{4+} contribution) which they attribute to a high degree of covalency. The reported n_f values for Tb systems are limited to TbO_2 , 0.42(4), and **10**,²⁵⁹ 0.39(4). Since cerocene has the largest component of trivalent character of any Ce complex studied to-date, terbocene is therefore an important target to investigate multiconfigurational behavior in lanthanides beyond Ce and as an important benchmark for the behavior of other tetravalent lanthanide complexes.^{253, 254, 303, 304} Theoretical studies predict that terbocene has a significant $4f^8$ contribution to the ground

state and L_3 -edge studies would be an important component of this investigation.³⁰⁵ See Table 5 for a list of selected Ce, Tb, and Pr n_f values.

The emergence of molecular Ln^{4+} complexes beyond Ce provides a new opportunity to investigate multiconfigurational behavior via L_3 -edge XAS. Through varying both the energy and radial extent of the metal valence orbitals, by changing the metal identity, a more complete understanding of the multiconfigurational behavior in lanthanide complexes can be achieved. Additionally, the physical basis of the spectral features can be further developed through the use of high energy resolution fluorescence detection (HERFD) XANES, which provides better resolution of multiplex features.^{277, 306-312}

Lanthanide M-edge XANES. M_4 - ($3d_{3/2} \rightarrow 4f_{5/2}$) and M_5 - ($3d_{5/2} \rightarrow 4f_{7/2}$ and $3d_{5/2} \rightarrow 4f_{5/2}$) edge spectroscopy provides unique insight into lanthanide materials by probing $4f$ valency at lanthanide ions.^{293, 298, 313-320} Multiplet structure and branching ratios in $M_{5,4}$ -edge spectra (*vide infra*) are valuable for characterizing orbital occupancies in $4f$ elements.³²¹⁻³²⁸ Features in these spectra show all allowed transitions from core-level $3d$ orbitals to unoccupied states containing $4f$ character. Kaindl and co-workers assembled an exhaustive set of the accessible tetravalent lanthanide fluorides of the general form A_2LnF_7 ($\text{A} = \text{Cs, Rb}$; $\text{Ln} = \text{Ce, Pr, Nd, Tb, Dy}$) to investigate through $M_{5,4}$ -edge XAS.²⁹³ These studies interrogated the ground state electronic configuration through the expected final state, *i.e.* a $4f^n$ ground state from a $3d4f^{n+1}$ (where $3d$ represents a $3d$ hole) final state. For $\text{Cs}_2\text{RbCeF}_7$, the typical multiplet expected for a $4f^0$ ion was observed with a dominant 3D_1 feature and a much smaller 3P_1 satellite feature 4.9 eV below the main peak. The dominant feature was 2.5 eV higher in energy than the analogous feature in CeF_3 , a trivalent fluoride counterpart.

This energy shift of the dominant peak is in contrast to the shift in energy observed for CeO₂ from Ce₂O₃ by Minasian co-workers.^{296, 329} In the oxides, the dominant feature is only 1.7 eV higher in energy. This difference in the peak shift from the fluorides to the oxides implies stronger ionic character for Ce⁴⁺ in the fluoride materials when compared to the oxides. A similar trend is seen with Cs₂RbTbF₇, where the dominant feature of the M_{5,4}-edge spectra is 2.4 eV higher in energy than the trivalent fluoride, in comparison to a difference of 1.2 eV in the equivalent oxides. Pr follows suit with an increase in the dominant peak of 2.5 eV in the fluorides versus 1.7 eV in the oxides.

For the stable dioxides (CeO₂, PrO₂, and TbO₂), M_{5,4}-edge spectroscopy provides evidence for Ln–L bond covalency and corroborates the covalency measured by ligand K-edge XAS studies (*vide infra*).²⁹⁶ Due to relatively large spin-orbit coupling in the lanthanides, both M₅ and M₄-edges are split into a more intense main feature and a higher energy satellite feature for all three dioxides (Figure 11). Analysis of the first and second derivatives of the M_{5,4}-edge spectra support the use of four pseudo-Voigt functions to fit the spectra of CeO₂ and PrO₂. Due to the complexity of the multiplet splitting for TbO₂, more functions are required to obtain a satisfactory fit. To quantify the effect of splitting, a branching ratio is defined, or the ratio of total peak intensity associated with the M₅ transition to the total peak intensity associated with both M₅ and M₄ transitions. This value is 0.44(5) for CeO₂ and PrO₂ and 0.65(7) for TbO₂. It is important to note that since final states are 3d⁹4fⁿ⁺¹ and 3d⁹4fⁿ⁺², the branching ratio is not suitable for investigating the amount of 4fⁿ⁺¹ that may be present in the ground state of the materials. The values of the branching ratios are consistent with expected trends for these three lanthanides; the ratios approach one as the series is traversed, because the probability of transitions to 4f_{5/2} state decrease as the *f*-orbitals are filled.

Configuration interaction (CI) calculations were performed to determine the origin of spectral features and assign how ground and final state mixing between Ln 4*f* orbitals and O 2*p* orbitals contribute to observed M_{5,4}-edge spectra. These calculations showed that using simply a purely trivalent or tetravalent model for Ce and Pr did not agree well. In particular satellite features are not modelled accurately. A more satisfactory model is obtained through a charge-transfer model using two ground-state configurations, 3d¹⁰4fⁿ and 3d¹⁰4fⁿ⁺¹, and the corresponding final-state configurations, 3d⁹4fⁿ⁺¹ and 3d⁹4fⁿ⁺². Both ground- and final-state are defined by the difference in charge-transfer energy, which can be benchmarked to experimentally observed LMCT feature in UV/vis spectra. The calculated ground states for CeO₂ and PrO₂ were similar. CeO₂ was calculated to be 70% 3d¹⁰4f⁰ and 30% 3d¹⁰4f¹, with a LMCT energy of 3.2 eV (experimental value is 3.1 eV³³⁰). PrO₂ was calculated to be 71% 3d¹⁰4f¹ and 29% 3d¹⁰4f², with a LMCT energy of 2.2 eV (experimental value is 2.4 eV³³¹). Although the amount of ligand hole character in the ground state for each of these materials is smaller than the amount determined from L₃-edge spectroscopy on the same materials, it does provide additional evidence for mixing between Ln 4*f* orbitals and O 2*p* orbitals in the ground-state.

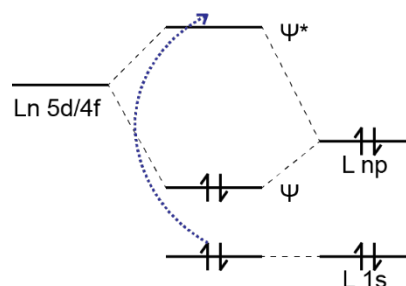


Figure 12. General depiction of transition from ligand 1s orbital to molecular antibonding orbital containing ligand *np* character. Figure adapted from 276.

M_{5,4}-edge XAS can also provide evidence of 4*f* occupation. However, this measurement is perturbed by the differences in formal oxidation state between analytes. Changing oxidation state affects the magnitude of the branching ratio and introduces satellite features for tetravalent complexes. For example, the spectra of molecular Ce⁴⁺ complexes differ from those of La³⁺ complexes, even though both ions are formally 4f⁰. Considering the most likely final state of 3d⁹4f¹, it is expected that there would be a singular peak for each the M₅- and M₄-edge. This structure is observed in La³⁺ spectra.³²³ However, the spectra of Ce(C₈H₈)₂, CeRh₃, and CeCl₆²⁻ contain the expected intense feature along with weaker satellite features.^{276, 296, 302, 332} These spectra are similar in shape to spectra of CeO₂.^{296, 324, 333, 334} However, the energy of the main features varies for each compound. The main features for [Ce(C₈H₈)₂] (882.0 and 900.0 eV) and CeRh₃ (882.6 and 900.1 eV) are lower in energy than in [CeCl₆]²⁻ (883.7 and 901.6 eV) and CeO₂ (883.7 and 901.7 eV). The former resembles the energy scale observed for formally trivalent Ce compounds such as [CeCl₆]³⁻ (882.3 and 900.0 eV) and [Ce(C₈H₈)₂]⁻ (882.4 and 900.2 eV). This similarity is suggestive that there may be correlation between peak energy in M-edge XAS and the *n_f* measured by L₃-edge XAS.

In this context, the branching ratio for the trivalent and tetravalent molecular hexachlorides can be used to compare, relatively, the 4*f* occupancy in the ground state.²⁷⁶ Since Ce³⁺ has one more 4*f* electron than its tetravalent counterpart, it is expected that Ce³⁺ would have a higher branching ratio than Ce⁴⁺. For the hexachlorides, the branching ratios are 0.50(3) and 0.48(2) for Ce³⁺ and Ce⁴⁺, respectively. Although the trivalent branching ratio is slightly higher, once error is considered, the values are essentially equal. This is similar to what is seen for PrO₂ and CeO₂²⁹⁶ (*vide supra*) and implies that the sensitivity of the technique may not be enough to easily distinguish between a 4f¹ and a 4f⁰ material.

Ligand K-edge XAS. Since ligand K-edge XAS probes bound-state, dipole-allowed 1*s* → *np* transitions from ligand-based orbitals, transitions to molecular orbitals with ligand *p*-character can be observed.^{102, 276, 296, 329, 335-358} Figure 12 depicts a generalized form of transitions from ligand based 1*s* orbitals to a molecular orbital containing ligand *p*-character. Measurement of the intensity of pre-edge features can allow for a quantitative measurement of orbital mixing, or metal-ligand covalency – *i.e.* the amount of mixing between ligand-based *p*-orbitals with metal-based *d*- and *f*-orbitals.

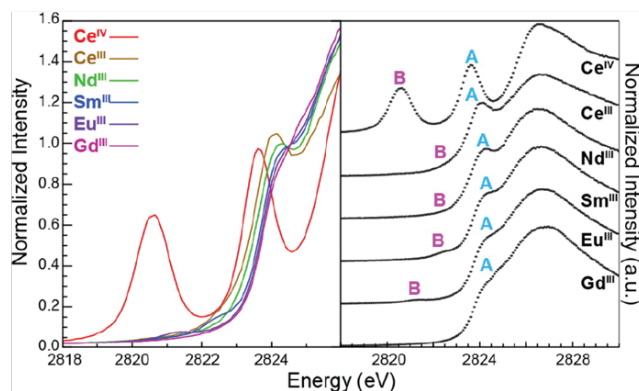


Figure 13. Overlay of Cl K-edge spectra for $[\text{CeCl}_6]^{2-}$ and $[\text{LnCl}_6]^{3-}$ ($\text{Ln} = \text{Ce}, \text{Nd}, \text{Sm}, \text{Eu}, \text{Gd}$). Reprinted with permission from M. W. Löble, J. M. Keith, A. B. Altman, S. C. E. Stieber, E. R. Batista, K. S. Boland, S. D. Conradson, D. L. Clark, J. Lezama Pacheco, S. A. Kozimor, R. L. Martin, S. G. Minasian, A. C. Olson, B. L. Scott, D. K. Shuh, T. Tyliczszak, M. P. Wilkerson and R. A. Zehnder, *J. Am. Chem. Soc.*, 2015, **137**, 2506-2523. Copyright 2015 American Chemical Society (Ref.276).

In Cl K-edge XAS studies of molecular hexachlorides, $[\text{LnCl}_6]^{3-}$ and $[\text{LnCl}_6]^{2-}$, Kozimor and co-workers challenged the conventional purely ionic description of lanthanide bonding.²⁷⁶ For the formally Ce^{4+} compound, $[\text{CeCl}_6]^{2-}$, two large pre-edge features were observed (Figure 13). The first feature (A) was near the onset of the rising edge at 2823.6 eV and the second feature (B) was lower in energy at 2820.6 eV. The two features were of comparable peak intensity, 0.84(8) and 0.70(7), respectively. When a similar analysis is applied to the formally trivalent compounds, $[\text{LnCl}_6]^{3-}$, a several differences are observed. Feature A is still present in each compound; however, it is located on the rising edge of the spectra (higher in energy) instead of just at the onset of the rising edge. Analysis of feature A suggests that the peak intensity for the Ln^{3+} complexes systematically decreases as atomic number increases in the lanthanides, from 0.93(9) for Ce to 0.48(5) for Gd. Feature B, on the other hand, is greatly diminished when compared to that of the Ce^{4+} compound for all Ln^{3+} Cl K-edge spectra. Furthermore, feature B becomes broader and lower in energy as you move down the series until it is undetectable in the spectra of $[\text{GdCl}_6]^{3-}$.

Assignment of these features was supported by time dependent density functional theory (TD-DFT) calculations and spectral simulation. The higher energy features (feature A) were largely associated with excitations from Cl 1s orbitals to 5d π -orbitals (t_{2g}^* set) while excitations to 5d σ -orbitals (e_g^* set) were hidden underneath the rising edge. Feature B was attributed to overlapping excitations to molecular orbitals containing Ln 4f character (t_{1u}^* and t_{2u}^* sets). Quantification of covalency in Ce–Cl bonds in $[\text{CeCl}_6]^{2-}$ indicates that the percentage of Cl 2p character is 11(1)% and 9.9(9)% for the 5d and 4f orbital sets, respectively. This result is in contrast to that for $[\text{CeCl}_6]^{3-}$, where Cl 3p character is 13(1)% and 1(1)% for the 5d and 4f orbital sets, respectively.

From these results, a few conclusions can be drawn about the nature of Ln–Cl bonds in these compounds. First, covalent mixing of Cl 2p orbitals and Ln 5d orbitals is prevalent in the trivalent lanthanides and the extent of this mixing decreases

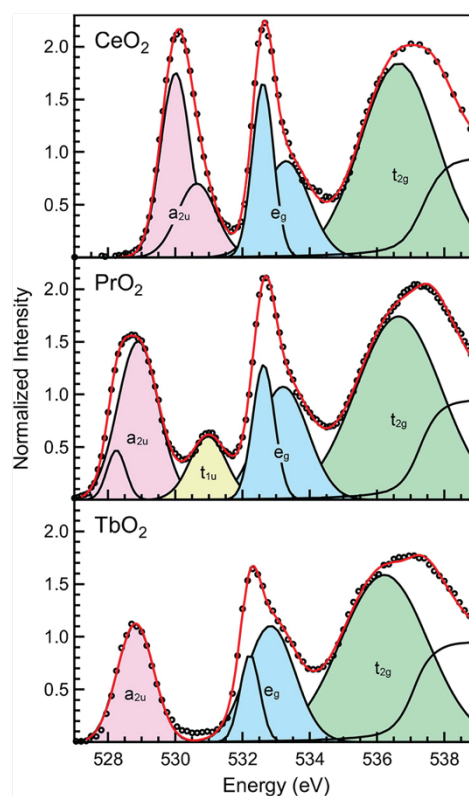


Figure 14. Curve fit pre-edge features of O K-edge spectra for Ln binary oxides of Ce, Pr, and Tb. Reprinted with permission from S. G. Minasian, E. R. Batista, C. H. Booth, D. L. Clark, J. M. Keith, S. A. Kozimor, W. W. Lukens, R. L. Martin, D. K. Shuh, S. C. E. Stieber, T. Tyliczszak and X.-d. Wen, *J. Am. Chem. Soc.*, 2017, **139**, 18052-18064. Copyright 2017 American Chemical Society (Ref.296).

with increasing Z. In a similar vein, Cl 3p mixing with Ln 4f orbitals is only marginal in the formally Ln^{3+} hexachlorides investigated in this study. Upon oxidation, in the case of Ce however, substantial 4f mixing ($t_{1u}^* + t_{2u}^*$) is observed with little to no effect on the 5d mixing observed in the trivalent analog. As a result, it is apparent tetravalent lanthanides can be regarded as more covalent as increased 4f mixing with ligand orbitals is observed with little effect on the 5d mixing.

This observation is further rationalized through the consideration of the radial extent of the 4f orbitals in Ln^{3+} versus Ln^{4+} . According to calculations for trivalent lanthanides, the valence 4f orbitals are eclipsed by the [Xe] core in the bonding region.³⁵⁹⁻³⁶⁴ However, these Cl K-edge results suggest that, upon oxidation, there is differential compression of the core orbitals versus the valence orbitals. As a result, the 4f orbitals are able to participate in covalent bonding.

Comprehensive O K-edge XAS studies have been performed by Minasian and co-workers on the entire series of trivalent lanthanide sesquioxides³²⁹ as well as the stable tetravalent dioxides, CeO_2 , PrO_2 , and TbO_2 .²⁹⁶ Utilizing pre-edge features in the O K-edge spectra for the sesquioxides, the covalent mixing between O 2p orbitals and Ln 5d/4f/6p orbitals was investigated. As seen in the Cl K-edge XAS studies of $[\text{LnCl}_6]^{3-}$, little 4f mixing is observed and there is a substantial amount of ligand 2p – Ln 5d/6p mixing.²⁷⁶ Furthermore, 2p – 5d mixing is further resolved to explicit σ - and π -symmetry. While π -

symmetry mixing remains relatively constant across the series, σ -symmetry mixing is maximized for La, Gd, Tb, Dy, Ho, and Er. In these cases, the covalent part of the Ln–O bond can best be described as an O $2p \rightarrow 5d$ charge transfer since there are no $4f^n$ or $4f^{n+1}$ states in the gap between filled O $2p$ and Ln $5d^1$ states. Reduced mixing in the other elements can be ascribed to $4f/5d$ hybridization (such as in the case with Ce, Pr, and Nd) and better energy parity between O $2p$ and Ln $4f$ orbitals which enhanced the amount of $2p \rightarrow 4f$ charge transfer possible.

For the stable dioxides, O K-edge XAS elucidates the magnitude at which the O $2p$ orbital participates in σ -symmetry mixing with lanthanide $4f$ and $5d$ orbitals and π -symmetry mixing with lanthanide $5d$ orbitals.²⁹⁶ Each spectrum (shown in Figure 14) contains large, distinctive pre-edge features below 540 eV, which are indicative of mixing between O $2p$ and Ln $5d$ and $4f$ orbitals. More specifically, each spectrum of the tetravalent dioxides contains a broad feature centered around 537 eV (t_{2g} set) and a sharper feature near 533 eV (e_g set). Ce and Tb each have a single additional sharp feature at 530.2 and 528.8 eV (a_{2u} set), respectively. Pr has two features in this region at 528.8 (a_{2u} set) and 531.0 eV (t_{1u} set).

Fitting of these pre-edge features allows for a direct comparison of O $2p$ mixing in Ce, Pr, and Tb through peak intensity. Oxygen $2p$ mixing with Ln $5d$ (both σ - and π -symmetry) remains relatively similar between the three elements and is a significant contributor to the covalent nature of Ln–O bonds in these dioxides. For the $1s \rightarrow e_g$ transitions, the peak intensities are 2.9(2), 3.1(2), and 2.9(2) for Ce, Pr, and Tb, respectively. Similarly, the intensities of the $1s \rightarrow t_{2g}$ transitions are nearly equivalent for the three elements: 5.2(5), 5.5(6), and 5.2(5) for Ce, Pr, and Tb, respectively. The larger $1s \rightarrow t_{2g}$ peak intensities are due to greater orbital overlap of the O $2p$ in σ -bonds than in π -bonds. The invariance of transitions to mixed $5d$ states is expected since the $5d$ orbital energies do not decrease in energy significantly across the series. However, the $4f$ orbital energies decrease across the lanthanide series.^{276, 365} When considering O $2p$ mixing with Ln $4f$, some variance is observed. As such, peak intensities for $1s \rightarrow a_{2u}$ transitions are 3.0(2), 2.6(2), and 1.5(2) for Ce, Pr, and Tb, respectively. PrO_2 also contains a unique $1s \rightarrow t_{1u}$ transition that is not present in the other two oxides and with a peak intensity of 0.8(1). Therefore, considering the relative invariance in σ - and π -type mixing of $5d$ orbital sets for these three elements and the hierarchy of $4f$ mixing, total covalency can be ranked as $\text{TbO}_2 < \text{CeO}_2 \leq \text{PrO}_2$.

F K-edge XAS was performed by Kaindl and co-workers to investigate covalency in Ln–F bonds.²⁹³ Trivalent fluoride materials, such as CeF_3 , contain only a singular broad peak superimposed on the rising edge, which is attributed to F $3p$ character hybridized with lanthanide $5d$ orbitals in unoccupied states. In tetravalent CeF_4 , a new feature appears ~ 2 eV below the main feature seen in CeF_3 , which also is attributed to a F $3p/\text{Ln } 5d$ hybrid state. Additionally, a new pre-edge feature is observed about 5.7 eV below the main feature. This pre-edge feature is attributed to a transition from F $1s$ to a $2p/4f$ hybrid state. The energy difference between the transition associated with $2p/4f$ state and the transition associated with $3p/5d$ state

is comparable to the energy difference between $4f$ and $5d$ bands observed in optical reflectivity measurements. In Cs_3CeF_7 , a pre-edge feature is observed at the same energy as was seen in CeF_4 , despite the difference in structure. An increase in the secondary main feature (2.4 eV below main feature) is observed. This is compared to CsF and assigned to be related to Cs–F bands. Because of this competing interaction, the pre-edge feature is comparatively small when looking at the edge jump and primary features. In Cs_3PrF_7 , a very similar spectral profile to that of Cs_3CeF_7 ; the primary difference is the pre-edge feature for Cs_3PrF_7 is centered 1.3 eV lower in energy than in Cs_3CeF_7 . The energy for this transition is the same for $\text{Cs}_2\text{RbTbF}_7$ but the peak intensity for the Tb compound is greatly decreased. This change in intensity is indicative of a reduced amount of $2p/4f$ mixing in Tb versus Pr and Ce.

Pre-edge features in C K-edge XAS studies provide evidence for mixing between Ce $5d/4f$ orbitals with the π system of cyclooctatetraenediide $[\text{COT}]^{2-}$ in $[\text{Ce}(\text{C}_8\text{H}_8)_2]$.³⁰² Furthermore, these results are contextualized through comparison with C K-edge studies of tetravalent actinides, $[\text{Th}(\text{C}_8\text{H}_8)_2]$ and $[\text{U}(\text{C}_8\text{H}_8)_2]$.³⁴⁸ Analogous to what is observed in Th and U, two main pre-edge features are observed for Ce at 284.2 and 286.7 eV. Similar to other ligand K-edge XAS studies, the peak intensities of these transitions are weighted and used to evaluate C $2p$ and Ce $4f/5d$ mixing in $[\text{Ce}(\text{C}_8\text{H}_8)_2]$.

Calculations are used to deconvolute overlapping transitions in the pre-edge region. TD-DFT was used to calculate absolute energy and oscillator strengths of singular transitions. From the calculated spectrum, the lowest energy feature at 284.2 eV was assigned to a transition from a C $1s$ orbital to a molecular antibonding $2e_{2u}$ (δ -type $4f$). The second feature was shown to be two overlapping transitions at 286.6 eV, corresponding to transitions to the antibonding $2e_{3u}$ and nonbonding $1e_{3g}$ sets.

The peak intensities of these features are weighted by the relative amount of C $2p$ to evaluate the extent of atomic orbital mixing between C and Ce. Despite convolution of features due to overlapping transitions of similar energy, patterns emerging from DFT calculations support qualitative comparisons extracted from the observed spectra. Notably, the $1s \rightarrow 2e_{2g}$ (σ -type $5d$) transition was not observed clearly in the obtained spectra for Ce but was composed of 22% C $2p$ and 76% Ce $5d$. This weighting is equivalent to the models of the resolved features for the $2e_{2g}$ set in $[\text{Th}(\text{C}_8\text{H}_8)_2]$ and $[\text{U}(\text{C}_8\text{H}_8)_2]$. The $1e_{3u}$ (5% C $2p$ and 95% Ce $4f$) and $2e_{3u}$ (89% C $2p$, 7% Ce $4f$) are described as non-bonding Ce and C-based orbital sets. This bonding pattern is similar to that observed in $[\text{U}(\text{C}_8\text{H}_8)_2]$. In $[\text{Th}(\text{C}_8\text{H}_8)_2]$, however, substantial ϕ -type mixing occurs.^{348, 366} The pre-edge feature at 284.2 eV in the C K-edge spectra is attributed to transitions to δ -type antibonding orbitals of the $2e_{2u}$ set (24% C $2p$ and 76% Ce $4f$). These orbitals are the counterpart to the bonding $1e_{2u}$ set (72% C $2p$ and 25% Ce $4f$). The extent of metal character of these orbitals is greater in $[\text{Ce}(\text{C}_8\text{H}_8)_2]$ than in $[\text{Th}(\text{C}_8\text{H}_8)_2]$ and similar to that in $[\text{U}(\text{C}_8\text{H}_8)_2]$. These results provide concrete evidence that the increase in $4f$ electron density in $[\text{Ce}(\text{C}_8\text{H}_8)_2]$ is a result of increased δ -type mixing.

It should be noted that Autsbach and co-workers have proposed an alternative interpretation of the C K-edge spectra of $[\text{Th}(\text{C}_8\text{H}_8)_2]$ and $[\text{U}(\text{C}_8\text{H}_8)_2]$ based on an *ab initio* multireference, restricted active space (RAS) approach.³⁰³ These calculations indicate that the experimental C K-edge XAS spectra do not indicate the involvement of ϕ -5f orbitals in ground state bonding for $[\text{Th}(\text{C}_8\text{H}_8)_2]$, and that for $[\text{U}(\text{C}_8\text{H}_8)_2]$ there is ligand to metal ϕ -bonding in the excited state. However, the multiconfigurational character of the wavefunction prevents the assignment of bonding interactions.

9. Optical Spectroscopy

Optical spectroscopy probes available transitions which are inherently tied to a specific oxidation state and electronic configuration. Similar to *d-d* electronic transitions in transition metals, *f-f* transitions in the lanthanides are forbidden based on selection rules. However, unlike transition metals, *f-f* transitions are not usually broadened or gain intensity through molecular vibrations and crystal field effects, which results in sharp transitions. On the other hand, *f-d* transitions in lanthanides are not orbital-forbidden and are relatively intense, especially in the case of Ce^{3+} and Tb^{3+} which have very intense transitions.

Optical spectroscopy has been carried out by Asprey and Varga to identify the free ion levels of Dy^{4+} and Nd^{4+} in Cs_3LnF_7 .^{367, 368} The presence of Dy^{3+} and Nd^{3+} impurities was evident from the optical spectra. The optical spectra of Nd^{4+} and Dy^{4+} were compared to their isoelectronic trivalent counterparts, Pr^{3+} and Tb^{3+} respectively. The observed optical spectra were fit to a function with spin-orbit coupling parameter (ζ) and Racah parameters E^1 , E^2 , and E^3 which are a function of the Slater radial integrals F_2 , F_4 and F_6 to determine the *f* energy levels for the corresponding free ions.

In Cs_3NdF_7 , all transitions (7 *f-f*) up to $^1\text{D}_2$ level at 487.8 nm (20500 cm^{-1}) were assigned using absorption spectra. Fluorescence spectra for Cs_3NdF_7 showed two sets of transitions at 350–380 nm (28571.4 – 26315.7 cm^{-1}) and 270–280 nm (37037 – 35714 cm^{-1}), the former was assigned to transitions from $^3\text{P}_1$, $^3\text{P}_0$ and $^1\text{D}_2$ (upper *f-f* transitions) and the latter to Nd^{3+} impurities or charge transfer. However, the transitions in the 350–380 nm region were broad and their origin was dubious. These transitions could be from the charge transfer band associated with orange/yellow color of Cs_3NdF_7 . Since *f-d* transitions were so high in energy, they were not observed in either the absorption or the fluorescence spectra.³⁶⁷

In Cs_3DyF_7 , six new transitions (*f-f*) between 3891 nm (2570 cm^{-1}) and 1333.3 nm (7500 cm^{-1}) were observed in the absorption spectra when compared to Cs_3DyF_6 . A broad absorption band with a maximum at 400 nm (25000 cm^{-1}) was observed and assigned as a charge transfer band giving rise to the orange/yellow color of Cs_3DyF_7 . With fluorescence, two more *f-f* transitions were observed at 525 nm and 630 nm. These transitions were assigned by comparison of the spectrum to isoelectronic Cs_3TbF_6 . Again, no *f-d* transitions were observed.³⁶⁸

In Cs_3TbF_7 no excitation was observed in either the fluorescence or the absorption spectra, hence putting a lower

limit on the first *f-f* transition at 303 nm (33000 cm^{-1}). Such high energies for *f-f* transitions in Tb^{4+} are reasonable because Gd^{3+} with the same electron configuration ($4f^7$) has the first *f-f* transition ~ 312.5 nm (32000 cm^{-1}). However, the first *f-f* transition for Tb^{4+} is higher in energy than Gd^{3+} due to less effective screening of the nuclear charge in tetravalent lanthanides. Asprey and Varga did not comment on the charge transfer band in Cs_3TbF_7 even though Tb^{4+} compounds are known have bright colors. Again, no *f-d* transitions were observed.³⁶⁸

Asprey and Reisfeld reported one *f-f* transition as expected for a $4f^1$ Pr^{4+} in Na_2PrF_6 and PrF_4 around 3466 nm (2885 cm^{-1}) corresponding to a $^2\text{F}_{5/2} \rightarrow ^2\text{F}_{7/2}$ transition.¹⁴² The authors did not comment on the charge transfer band in Pr^{4+} fluorides. Again, there were no observable *f-d* transitions. While the study by Asprey and Reisfeld reported only one *f-f* transition for Pr^{4+} , Popova *et al.*, reported five *f-f* transitions in the optical spectrum of BaPrO_3 .³⁶⁹ The observation of five *f-f* transitions is in stark contrast to the expectation for a $4f^1$ system. However, the five *f-f* transitions are a result of comparable energy scales of CEF and SOC in tetravalent lanthanides. Two excitations were observed in the energy range of 900–2500 nm (11111 – 4000 cm^{-1}) and were assigned to excitations to Γ_8' and Γ_6 states based on a cubic symmetry first approximation as shown in Figure 7. Electric dipole transitions between different CEF levels are forbidden but transitions to Γ_7' and Γ_8' are magnetic dipole allowed. The optical excitation at 1449 nm (6900 cm^{-1}) was assigned as a Γ_7 to Γ_6 vibronic transition. The optical excitation at 1887 nm (5300 cm^{-1}) was assigned to a Γ_7 to Γ_8' transition. The transition corresponding to Γ_7 to Γ_8' is asymmetric, probably due to the splitting of the quartet into two Kramer's doublets due to a lower CEF symmetry (a cubic CEF was a first order approximation). Further investigation of the optical spectroscopy on BaPrO_3 resulted in the observation of two transitions, a two-peak feature at 4968 nm (2013 cm^{-1}) and 4885 nm (2047 cm^{-1}) and a single maximum at 3182 nm (3143 cm^{-1}).³⁷⁰ The transition at 3182 nm is assigned to a Γ_7 to Γ_7' transition. The excitations at 4968 nm and 4885 nm correspond to Γ_7 to Γ_8 transitions (where Γ_8 is a quadruplet split into two Kramer's doublets due to a lower CEF symmetry). For a Pr^{4+} free ion the first *f-d* transition is situated at 86.9 nm (115052 cm^{-1} , measured in the gas phase).³⁷¹

The one *f-f* transition observed in PrF_4 and Na_2PrF_6 corresponds to a transition between two different J manifolds, $J = 5/2$ and $J = 7/2$ with $7\zeta/2 = 2885$ cm^{-1} resulting in $\zeta = 824$ cm^{-1} . In BaPrO_3 the transition between Γ_7 with predominantly $J = 5/2$ character to Γ_7' with predominantly $J = 7/2$ character can be considered as the first *f-f* transition between the two different J manifolds. Crystal field calculation on BaPrO_3 by Popova *et al.*, provides a $\zeta = 840$ cm^{-1} . Both the reported values of SOC parameters are less than the SOC parameter for a Pr^{4+} free ion (865 cm^{-1}).³⁷¹ This discrepancy could be attributed to the effect of the ligand fields on Pr^{4+} .³⁷⁰

Corresponding ζ values for 3+ and 4+ lanthanides are plotted in Figure 15. It is evident that the spin-orbit coupling parameter for tetravalent lanthanides is greater than the trivalent lanthanides. It should be noted that, in Ln^{3+} , there is a break in

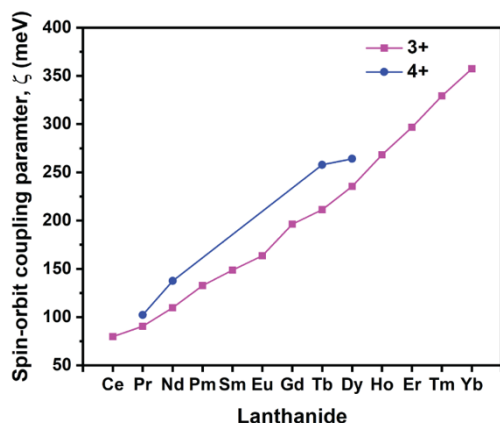


Figure 15. Spin orbit coupling (SOC) parameter, ζ for Ln^{3+} (pink trace) and Ln^{4+} (blue trace) plotted against corresponding lanthanide. Figure adapted from reference 368.

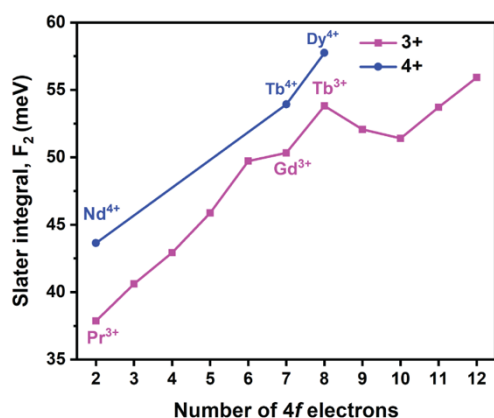


Figure 16. Slater integral term, F_2 for Ln^{3+} (pink trace) and Ln^{4+} (blue trace) plotted against corresponding electron configuration. Figure adapted from reference 368.

the spin-orbit coupling parameter at Gd^{3+} with $4f^7$ electron configuration, however, in the $4+$ oxidation state, there is a break at Tb^{4+} with $4f^7$ electronic configuration. The Slater integral, F_2 , which corresponds to Racah parameter is plotted in Figure 16. The trend of F_2 in Ln^{4+} follows the trend in Ln^{3+} with breaks at $4f^7$ and $4f^8$ electron configurations.³⁶⁸ Following this trend, the SOC parameter and F_2 values could potentially be extrapolated to other lanthanides in the tetravalent oxidation and hence serve as a guideline to assigning different transitions in the optical spectra.

Hoefdraad reported charge transfer spectra of Ce^{4+} , Pr^{4+} , and Tb^{4+} doped in several diamagnetic oxide lattices. When the lanthanides are in an octahedral O environment, two absorption bands are observed for Pr^{4+} and Tb^{4+} around 400 nm (25000 cm^{-1}) and 333.3 nm (30000 cm^{-1}) and one absorption band for Ce^{4+} at higher energies 312.5 nm (32000 cm^{-1}).³³¹ When the lanthanides are surrounded by eight O^{2-} ions, three absorption bands are observed for Pr^{4+} and Tb^{4+} around 500 nm (20000 cm^{-1}), 434.7 nm (23000 cm^{-1}) and 333.3 nm (30000 cm^{-1}).

and one absorption band for Ce^{4+} at 317.4 nm (31500 cm^{-1}). These absorption bands for both six and eight coordination number were found to be red-shifted when compared to their corresponding trivalent counterparts. The red-shift of the first absorption band between six and eight coordination number in tetravalent lanthanides has been attributed to the degree of perturbation of the energy levels of $4f$ and $5d$ orbitals by the surrounding O atoms.

Aqueous, molecular UV/vis studies are similar to the aforementioned optical spectroscopy studies in extended solids in which new transitions are observed upon oxidation to the tetravalent oxidation state. In Hobart and Peterson's UV/vis studies of aqueous Pr, in high concentrations of carbonate and hydroxide, show that upon oxidation, either electrolytically or chemically, the fine $f-f$ transitions are bleached and a very broad band is introduced, which is most likely attributable to a charge transfer event. This broad feature at 283 nm (35335 cm^{-1}) was estimated to have an extinction coefficient $>1000 \text{ cm}^{-1}\text{M}^{-1}$. In a similar vein, oxidation of Tb results in decreases in the absorbance features characteristic for the trivalent ion, and an increase in the intensity of a broad band spanning 250–650 nm ($40000\text{--}15385 \text{ cm}^{-1}$) with a peak maximum at 365 nm (27397 cm^{-1}). This absorbance feature is estimated to have a molar absorptivity greater than a $1000 \text{ cm}^{-1}\text{M}^{-1}$ by correlating the decrease in absorbance of the Tb^{3+} features and increase in absorbance of the Tb^{4+} feature.

The UV/vis/NIR electronic absorption spectra for the three isolated tetravalent Tb complexes are best described as single broad absorption features with extinction coefficients between $3000\text{--}4500 \text{ cm}^{-1}\text{M}^{-1}$. These absorption spectra are consistent with early work by Hobart and Peterson.²³⁴ The absorption spectrum for the deep indigo complex, **10**, spans 375–1100 nm ($26667\text{--}9091 \text{ cm}^{-1}$) with an extinction coefficient of $3700 \text{ cm}^{-1}\text{M}^{-1}$ in THF consistent with a charge transfer transition.²⁷³ This is in stark contrast with the Tb^{3+} complex, **9**, which has no observable transitions in the UV/visible/NIR in THF. For the siloxide complexes, the absorption spectra span a much smaller range and the absorption maxima are shifted higher in energy, likely due to the more electronegative O donors in comparison to N. For the orange Tb^{4+} complex **12**,²⁶⁰ the absorption spectrum spans 275–570 nm ($36364\text{--}17544 \text{ cm}^{-1}$) with an extinction coefficient of $4200 \text{ cm}^{-1}\text{M}^{-1}$ at 371 nm (26954 cm^{-1}) in toluene while the orange Tb^{4+} complex, **14**,²⁶¹ spans 275–650 nm ($36364\text{--}15385 \text{ cm}^{-1}$) with an extinction coefficient of $3000 \text{ cm}^{-1}\text{M}^{-1}$ at 386 nm (25907 cm^{-1}) in THF, both of which are consistent with a charge transfer transition.

In line with the work by Hoefdraad, the broad features seen in the three Tb^{4+} complexes can be assigned to charge transfer bands. While multiple charge transfer bands were observed for Tb^{4+} with both six and eight oxygen coordination numbers in the solid state, only one broad charge transfer band is observed for all Tb^{4+} complexes. In the solid state, the charge transfer bands are higher in energy compared to the molecular Tb^{4+} complexes and this can be attributed to the different degrees of delocalization of $4f/5d$ orbitals depending on the extent of interaction with different ligand fields. As expected from the

solid state, no f - f / f - d transitions were observed in the Tb⁴⁺ complexes.

The UV/vis/NIR absorption spectrum of the brown Pr⁴⁺ complex, **16**, spans 275 – 700 nm (36364 – 14286 cm⁻¹) with a molar absorptivity coefficient of 3800 cm⁻¹M⁻¹ at 363 nm (27548 cm⁻¹) in THF.²⁶² The molar absorptivity of this feature is consistent with that of a charge transfer transition. This spectrum is more asymmetric than those of the Tb siloxides. These results on Pr are also in line with the aqueous studies of Pr⁴⁺ by Hobart and Peterson. The absorption spectrum for **16** is in line with absorption spectra reported for Pr⁴⁺ doped in different diamagnetic lattices, which also contained a charge transfer feature. Within the energy range measured, no f - f transitions were observed, in line with the optical spectra of BaPrO₃ where all five f - f transitions were observed in the far IR region between 1500 nm (6667 cm⁻¹) – 4900 nm (2041 cm⁻¹).³⁶⁹ The f - d transitions are likely too high in energy to be observed.

10. Magnetic Properties

The only magnetic data available for Ln⁴⁺ ions are Pr⁴⁺ and Tb⁴⁺. Pr and Tb in the tetravalent oxidation state have electronic configurations of 4f¹ and 4f⁷, respectively. Due to their characteristic paramagnetism, magnetic studies can be used to assign oxidation state and understand the electronic structure of tetravalent lanthanides complexes and extended solids. Lanthanides exhibit significant SOC, and optical spectroscopy measurements have shown that SOC is further enhanced in the tetravalent oxidation state compared to the trivalent oxidation state (*vide supra*).

Lanthanide anisotropy results from unquenched orbital moments, hence making J a good quantum number to describe the trivalent lanthanides. This model is in contrast to that for transition metals (mainly first and second row) where S is a good quantum number since these elements exhibit quenched orbital moments. Hence all three empirical Hund's rule plays a critical role in determining the ground state of trivalent lanthanides while the first two empirical rules are sufficient to describe the ground state of first and second row transition metals. The trivalent lanthanides are best described in the Russell-Saunders (L - S coupling) scheme. Extending the same conceptualization of ground states to tetravalent lanthanides, the electronic structure of Pr⁴⁺ and Tb⁴⁺ can be explained using ground states ²F_{5/2} and ⁸S_{7/2}, respectively. The expected room temperature magnetic moments for pure ²F_{5/2} and ⁸S_{7/2} ground states are 2.54 μ_B and 7.94 μ_B respectively assuming the ground state is completely populated at room temperature.

DC-susceptibility measurements were performed on all three tetravalent terbium complexes and their trivalent counterparts. The expected magnetic moment at room temperature for a 4f⁸ Tb³⁺ ion is 9.72 μ_B in contrast to the lowered moment for the 4f⁷ Tb⁴⁺ ion, which is 7.94 μ_B. For **10**, the magnetic moment was 8.27 μ_B while the Tb³⁺ precursor, **9**, was 10.7 μ_B.²⁷³ Both values are higher than the expected moments but clearly demonstrate a change in oxidation state from Tb³⁺ to Tb⁴⁺. In addition to the Tb³⁺ and Tb⁴⁺ complexes, Mazzanti and co-workers synthesized the isoelectronic 4f⁷ Gd³⁺ equivalent to the *tert*-butoxy siloxide Tb⁴⁺ complex. The

complex [K][Gd³⁺(OSi(O^tBu)₃)₄] had a magnetic moment of 7.88 μ_B and the Tb⁴⁺ complex, **12**, of 7.89 μ_B, confirming the 4f⁷ configuration.²⁶⁰ The Tb³⁺ complex, **11**, had a magnetic moment of 9.46 μ_B, which although slightly lower than the predicted value, confirms the change in oxidation state between the two Tb complexes. For the Tb⁴⁺ phenyl siloxide, **14**, the magnetic moment was consistent with the previous tetravalent complex at 7.91 μ_B.²⁶¹ The Tb³⁺ complex's, **13**, magnetic moment was 9.12 μ_B, significantly lower than the predicted value. These moments are consistent with values obtained for extended solid state Tb⁴⁺ compounds (Table 2).^{95, 151, 155}

Similar trends were seen for magnetic studies of molecular Pr. The expected magnetic moment at room temperature for the 4f² Pr³⁺ ion is 3.58 μ_B, larger than that of the 4f¹ Pr⁴⁺ ion at 2.54 μ_B. Additionally, Mazzanti and co-workers synthesized a Ce³⁺ complex for comparison to the isoelectronic Pr⁴⁺ complex. For [K][Ce³⁺(OSiPh₃)₄(THF)] the magnetic moment was 2.08 μ_B while for **16** it was 2.23 μ_B, below the predicted value but consistent with the assignment of a 4f¹ ion.²⁶² Likewise, the magnetic moment for the Pr³⁺ complex, **15**, is higher at 3.46 μ_B and consistent with a 4f² ion. These magnetic studies are in contrast with extended solid systems of Pr⁴⁺.

The shape of the DC susceptibility vs T plot for **16** is in reasonable agreement with that of [K][Ce³⁺(OSiPh₃)₄(THF)]. In both complexes, $\chi_{\text{m}}T$ monotonously decreases from room temperature down to the lowest temperature measured, which can be attributed to thermal depopulation of low-lying Kramer's doublets. The ²F_{5/2} ground state J multiplet in the Ce³⁺ and Pr⁴⁺ complexes are split by the crystal field into three Kramer's doublets with $|J, M_J\rangle = |5/2, \pm 1/2\rangle$, $|5/2, \pm 3/2\rangle$, and $|5/2, \pm 5/2\rangle$.³⁷² Mazzanti and co-workers report the absence of an EPR spectrum at 5 K for both the Ce³⁺ and Pr⁴⁺ complexes (*vide infra*). Assuming only the ground state doublet is populated at 5 K, the absence of an EPR spectrum rules out the possibility of a $|5/2, \pm 1/2\rangle$ ground state with XY anisotropy ($g_{\parallel} = 0.86$, $g_{\perp} = 2.57$) in both complexes.³⁷²

The observed results for [K][Ce³⁺(OSiPh₃)₄(THF)] and **16**²⁶² indicate that the ground states could be comprised of either the $|5/2, \pm 3/2\rangle$ doublet with $g_{\parallel} = 2.57$, $g_{\perp} = 0$ and an expected magnetic moment of 1.28 μ_B or $|5/2, \pm 5/2\rangle$ doublet with $g_{\parallel} = 4.29$, $g_{\perp} = 0$ and expected magnetic moment of 2.14 μ_B (both Kramer's doublets exhibit Ising anisotropy).³⁷² However, the possibility of a quartet ground state cannot be ruled out (although unlikely in lower symmetry complexes). The observed magnetic moment at 5 K for the Ce³⁺ complex is ~1.25 μ_B is in reasonable agreement with the $|5/2, \pm 3/2\rangle$ ground state doublet and for the Pr⁴⁺ complex with ~1 μ_B is less than the expected value for either a pure $|5/2, \pm 3/2\rangle$ or $|5/2, \pm 5/2\rangle$ doublet and hence making the ground state assignment difficult.

Mixing the ground state with excited states in the same J manifold could potentially explain the reduced moment of Pr⁴⁺ complex with a ground state of the form $a|5/2, \pm 3/2\rangle + b|5/2, \pm 5/2\rangle + c|5/2, \pm 1/2\rangle$, $a^2 + b^2 + c^2 = 1$. The room temperature magnetic moments of the Ce³⁺ and Pr⁴⁺ complexes are less than the expected value for a f^1 , indicative of the ²F_{5/2}

ground state not being completely populated at room temperature.

However, the above explanation is valid only when assuming that the electronic structures of the Pr^{4+} and Ce^{3+} complexes are alike. The observed room temperature magnetic moment of Pr^{4+} complex is in contrast to observed magnetic moments for Pr^{4+} extended solids which exhibit reduced moments ($0.5 - 1.5\mu_B$).^{95, 96} From the CEF scheme established in the solid-state section for f^1 systems, the first excited state of Pr^{4+} in BaPrO_3 (260 meV) is an order of magnitude greater than for Ce^{3+} in $\text{Ce}_2\text{Sn}_2\text{O}_7$ (55 meV) and Pr^{3+} in $\text{Pr}_2\text{Zr}_2\text{O}_7$ (9.53 meV) shown in Figure 17.^{198, 373, 374} When the crystal field splitting is comparable to SOC, the $J = 7/2$ manifold mixes into the $J = 5/2$ manifold. The energy splitting diagram for a f^1 ion in an O_h point symmetry based on the relative interaction energy between SOC and the crystal field is shown in Figure 18. Extending the same conceptualization to molecular complexes, one might expect the first excited state for the Pr^{4+} complex, **16**, to be significantly greater than in the Ce^{3+} complex. This can be addressed by considering mixing the $J = 7/2$ manifold with the ground state $J = 5/2$ manifold with a more likely ground state of the form $a|5/2, \pm 3/2\rangle + b|7/2, \pm 3/2\rangle$, $a^2 + b^2 = 1$. The exact splitting diagram for **16** is complicated considering the lower point group symmetry at the metal center. Simply, this initial result on Pr^{4+} in **16** is exciting.²⁶² Further work will be helpful to understand ligand effects on ground state electronic structure in Pr^{4+} .

11. EPR Spectroscopy

Tetravalent Pr and Tb are the only tetravalent ions to-date interrogated by EPR. This limitation is due to the chemical inaccessibility of other paramagnetic Ln^{4+} ions such as the non-Kramers ions Nd^{4+} and Dy^{4+} .³⁷⁵ Analysis of their electronic structure is based on their electronic configurations, Pr^{4+} , $4f^1$ and, Tb^{4+} , $4f^7$, (both Kramers ions) using SOC and crystal field interactions as the major considerations. In the case of the trivalent lanthanides, SOC constants are typically significant ($640 - 2800 \text{ cm}^{-1}$) in contrast to first and second row transition metals. These effects are much larger than the observed crystal field effects, which is on the order of 100 cm^{-1} for Ln^{3+} .³⁷⁶ However, in tetravalent lanthanides, the crystal field effects are at least a magnitude greater than the corresponding trivalent lanthanides (on the order of 1000 cm^{-1}) as established in the solid-state section via INS.¹⁹⁸

¹⁴¹Pr (100% abundance) is expected to have a characteristic six absorption lines in its tetravalent state, attributable to the hyperfine interaction of the sole f -electron with its nuclear spin ($I = 5/2$) as shown in Figure 19. Since SOC and CEF are of comparable energy scales in Pr^{4+} , resulting in competing interactions, the traditional models of $4f^1$ (Ce^{3+}) systems with L - S coupling limits might not be the obvious choice resulting in intermediate coupling limits. Following the CEF scheme established in the solid-state section for PrO_2 and BaPrO_3 , the energy splitting diagram for Pr^{4+} in an octahedral crystal field is shown in Figure 18. This splitting is similar to the energy splitting diagram for $5f^1$ systems, Pa^{4+} , U^{5+} and Np^{6+} , which deviate from the L - S coupling limits, but SOC and CEF are both of greater

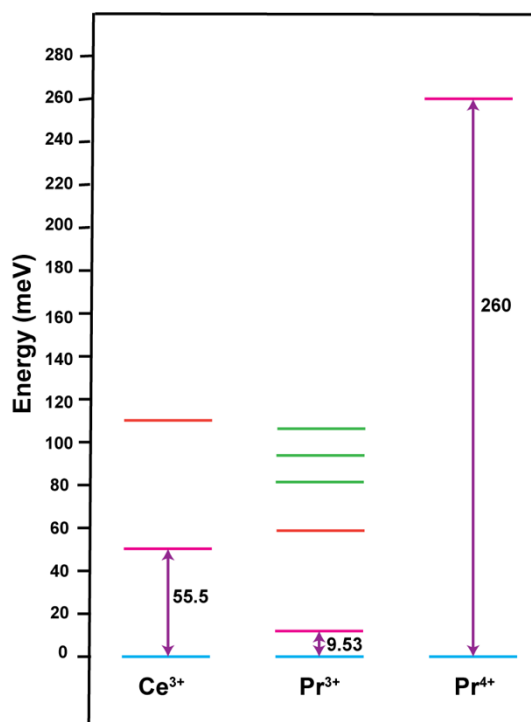


Figure 17. CEF energy diagram for Ce^{3+} in $\text{Ce}_2\text{Sn}_2\text{O}_7$ (D_{3d} point group symmetry), Pr^{3+} in $\text{Pr}_2\text{Zr}_2\text{O}_7$ (D_{3d} point group symmetry) and Pr^{4+} in BaPrO_3 (O_h point group symmetry). The ground states are indicated by yellow lines, the first excited states by pink, the second excited states by red and further excited states by green. The purple lines indicate the energy separation between the first excited state and the ground state. Data from references 198, 373, and 374.

magnitude for the actinides. The solid-state section briefly describes the splitting of $J = 5/2$ manifold in an octahedral crystal field. However, for the best description of intermediate coupling, crystal field splitting of the excited state $J = 7/2$ manifold is crucial. The ${}^2F_{7/2}$ excited state is split by the O_h crystal field to a Γ_7' quartet, Γ_8' doublet, and a Γ_6 doublet as shown in Figure 18.³⁷⁷

The g values for an f electron in the Γ_7 doublet (perturbed by the octahedral crystal field) have been calculated to be $-10/7$ and for an f electron in Γ_2 (with no SOC) is 2. Hence the value of g for f^1 should lie between $-10/7$ and 2 depending on the ratio of the crystal field parameter and the SOC parameter.³⁷⁷ With increasing crystal field, the g value increases from $-10/7$.

The hyperfine structure of Pr^{4+} has been studied through its doping into various host materials.³⁷⁸ Direct observation of the hyperfine structure of Pr^{4+} in phase-pure systems was not possible due to strong spin orbit interactions. All measurements were carried out at 4.2 K. The EPR absorption lines became significantly weaker in intensity with increase in temperature. When doped into BaCeO_3 , the six expected allowed transitions were observed along with five forbidden ones.³⁷⁸ These forbidden transitions are diminished as the Pr^{4+} is further diluted. The nuclear spin of Pr^{4+} ($I = 5/2$) couples with $S = 1/2$ to generate $F = I + S$ states. In the absence of a magnetic field, $F = 2$ (when $S = -1/2$) and $F = 3$ (when $S = +1/2$) states are split by $3A$, where A is the hyperfine coupling constant.³⁷⁷ In the presence of a magnetic field, the $F = 2$ states are split into five $|2, \pm m_F\rangle$ states by Zeeman interactions while $F = 3$ states are split into

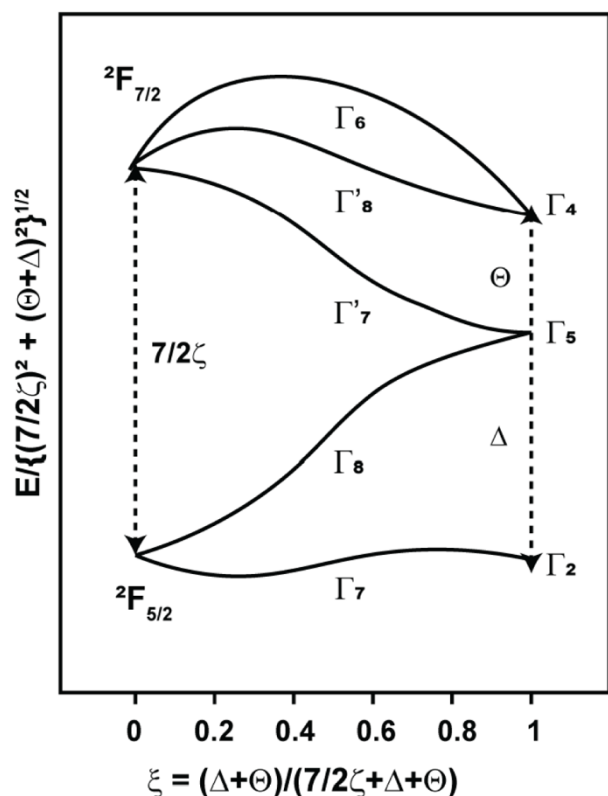


Figure 18. Energy splitting of a f^n system as a function of ξ determined by the relative magnitudes of crystal field splitting parameters (Δ and Θ) and SOC parameter (ζ). $\xi = 1$ corresponds to a strong crystal field limit with SOC parameter (ζ) = 0 and $\xi = 0$ corresponds to a weak crystal field limit with crystal field parameters $\Delta + \Theta = 0$. Figure adapted from reference 377.

seven $|3, \pm m_F\rangle$ states. The six allowed transitions follow the selection rule $\Delta F = \pm 1$, $\Delta m_F = \pm 1$ as shown in Figure 19. The five observed forbidden transitions were assigned as $\Delta F = \pm 1$ and $\Delta m_F = \pm 0$. The forbidden transitions were not observed in any other Pr^{4+} doped host lattices. In very dilute, Pr doped zirconium and tin perovskites (Pr^{4+} : BaZrO_3 , BaSnO_3), very distinct hyperfine lines broader than in BaCeO_3 (hence masking the forbidden transitions) are observed and, in some cases, only five lines are observed.³⁷⁹ Calculations demonstrated that the sixth line is expected at a higher field that was not instrumentally accessible.

Pr^{4+} doped in different diamagnetic oxide lattices has also been studied. It should be noted here that the number of observed allowed transitions varies anywhere between 4 – 12 depending on the lattice and the accessible scan window of the instrument. All these EPR spectra were fit to the following Hamiltonian by Hinatsu in Equation 7:³⁸⁰

$$H = g\beta H \cdot S + AS \cdot I - g'_N \beta H \cdot I \quad (7)$$

where g is the value corresponding to spin, g'_N is the value corresponding to Pr nucleus, A is the hyperfine coupling constant, I is the nuclear spin, H is the magnetic field applied and β is the Bohr magneton. The best fit parameters with g values and hyperfine coupling constant (A) are summarized in Table 6 along with values determined for isoelectronic Pa^{4+} , U^{5+}

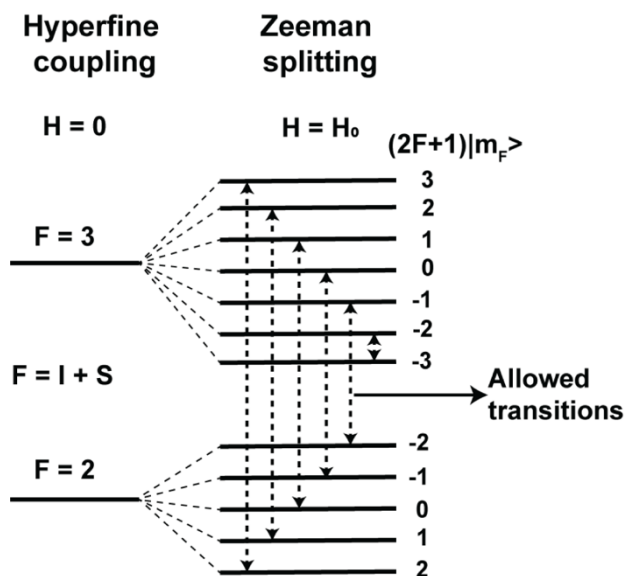


Figure 19. Energy level splitting diagram for hyperfine coupled term of Pr^{4+} with $F = I + S$, where $I = 5/2$ is the nuclear spin and $S = \pm 1/2$ is the electron spin in the presence and absence of a magnetic field. The absence of the magnetic field is represented by $H = 0$ and the presence of magnetic field by $H = H_0$. Dotted arrows indicate allowed transitions. It should be noted here that the Zeeman splitting levels are equally space only for clarity.

and Np^{6+} .³⁸¹⁻³⁸⁵ The EPR spectrum for Pr^{4+} : $\text{La}_2\text{Sn}_2\text{O}_7$ has been simulated using EasySpin³⁸⁶ with the parameters provided by Hinatsu *et al.*,³⁸⁰ and plotted in Figure 20. When Pr^{4+} is doped in Ce^{4+} based lattices (SrCeO_3 and Sr_2CeO_4) there are twelve observed transitions. These transitions in Pr^{4+} : Sr_2CeO_4 can be separated into two different groups each consisting of six transitions and has been attributed to significant anisotropy of hyperfine interaction between the nuclear spin and electron spin parallel and perpendicular to the crystallographic c -axis due to the axial symmetry ($|g_{\parallel}| > |g_{\perp}|$).³⁸⁷ In Pr^{4+} : SrCeO_3 , a spatially anisotropic g tensor with $|g_x| > |g_y| > |g_z|$ was used to fit the spectrum.³⁷⁹ The fit parameter with corresponding anisotropic values are provided in Table 6. The EPR spectrum for Pr^{4+} : SrCeO_3 has been simulated using in EasySpin with the parameters provided by Hinatsu *et al.*³⁷⁹ and has been plotted in Figure 20.

While all of the host lattices described above include Pr^{4+} in a pseudo O_h environment, studies have been carried out by Parker and Harris, where Pr^{4+} doped in ZrSiO_4 single crystals is coordinated to eight O atoms, thereby reducing the point group symmetry at Pr^{4+} compared to previous studies.³⁸⁸ The corresponding A and g values are listed in Table 6. At 4.2 K, six widely spread hyperfine lines were observed with significantly small anisotropy along and normal to c -axis (z -direction parallel to c -axis).

It should be noted that in all the studies discussed above, a first order approximation of an O_h crystal field was assumed irrespective of the point group symmetry at Pr^{4+} . The above studies do not provide the sign of the g value. However, by creating an analogy to isoelectronic $5f^n$ systems – Pa^{4+} , U^{5+} and Np^{6+} , Hinatsu and Edelstein assigned a negative sign to the g value of Pr^{4+} .³⁸⁵ Based on these tabulated g values, it has been

concluded that as crystal field increase, the $|g|$ value decreases. Hinatsu and Edelstein have argued, based on the values in Table 6, the $|g|$ values for Pr^{4+} (except $\text{La}_2\text{Sn}_2\text{O}_7$ and $\text{La}_2\text{Zr}_2\text{O}_7$) are comparable to the $|g|$ value of Np^{6+} meaning, the ratio of crystal field to SOC experienced by Pr^{4+} is comparable to that experienced by Np^{6+} .³⁷⁷

Table 6. Summary of different f^1 systems studied via EPR in different host materials with corresponding g and hyperfine coupling constant values (A).

Doped ion	Host material	$ g $	Hyperfine coupling constant A (cm^{-1})	
Pr^{4+}	Ba_2SnO_4 ³⁸⁹	0.6460	0.0605	
	Sr_2SnO_4 ³⁸⁹	0.6150	0.0605	
	Sr_2CeO_4 ^{387a}		1.1690,	0.0703,
			0.9660	0.0669
	$\text{La}_2\text{Sn}_2\text{O}_7$ ³⁸⁰	1.2620	0.0752	
	$\text{La}_2\text{Zr}_2\text{O}_7$ ³⁸⁰	1.2700	0.0768	
	BaSnO_3 ³⁷⁸	0.5830	0.0589	
	BaZrO_3 ³⁷⁸	0.6480	0.0597	
	BaCeO_3 ^{377b}		0.7410	0.0609
		BaHfO_3 ³⁹⁰	0.6190	0.0589
	SrCeO_3 ^{379a}		0.8750,	0.0712,
			0.7900,	0.0643,
			0.7550	0.0614
	$\text{Ba}_3\text{Sn}_2\text{O}_7$ ³⁹¹	0.6060	0.0608	
Li_8CeO_6 ¹³³	0.5500	0.0610		
ZrSiO_4 ^{388a}		1.0038,	0.0604,	
		1.0384	0.0638	
Pa^{4+}	Cs_2ZrCl_6 ³⁸⁵	1.1420	0.0526	
	LiUF_6 ³⁸²	0.7680	-----	
U^{5+}	UCl_6 ³⁸¹	1.1200	-----	
	UBr_6 ³⁸²	1.2100	-----	
Np^{6+}	NpF_6 ³⁸⁴	0.6040	0.1100	

^a Fit parameters includes anisotropic g and A values because of the presence of 12 transitions.

^b Pr^{4+} : BaCeO_3 is the only system that shows forbidden transitions.

Extending the analogy of ground states for f^1 systems from the magnetism section, the ground state of Pr^{4+} ions (Γ_7 doublet) in the solid-state under a pseudo O_h crystal field has predominantly $|5/2, \pm 1/2\rangle$ character. However, the possibility of mixing from the excited state cannot be ruled out since the magnetic moment observed in some of the doped systems is significantly lower ($0.503 \mu_B$ in Li_8PrO_6 , $0.68 \mu_B$ in BaPrO_3) than expected for a $|5/2, \pm 1/2\rangle$ ground state ($1.35 \mu_B$).^{133, 392} This discrepancy can be attributed to the small g values observed in the EPR spectra of Pr^{4+} solid-state systems. Such reduced g values can be obtained by accommodating significant mixing from within the same J manifold or from excited state J manifold as described in the magnetism section. Mazzanti and co-workers reported the absence of an X-band EPR spectrum for the molecular Pr^{4+} complex, **16**, at 5 K in frozen solutions of toluene or THF. As explained in the magnetism section, the absence of EPR spectrum is indicative, though not definitive proof, of a ground state different from $|5/2, \pm 1/2\rangle$.

Tetravalent Tb is like Pr^{4+} in that the trivalent Tb is a non-Kramer ion while the tetravalent state, is a Kramer ion. The

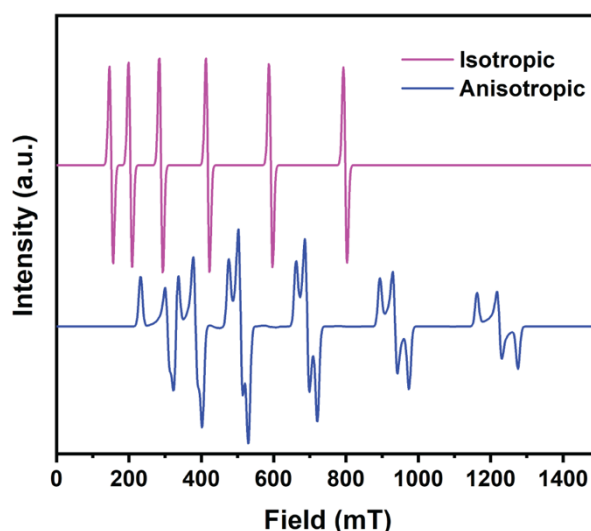


Figure 20. Simulated EPR spectra for Pr^{4+} doped in $\text{La}_2\text{Sn}_2\text{O}_7$ (pink trace) and SrCeO_3 (yellow trace) using parameters obtained from reference 379 and 380. The EPR spectra were simulated using the EasySpin software package incorporated in Matlab (Ref. 386). The EPR spectrum for Pr^{4+} : $\text{La}_2\text{Sn}_2\text{O}_7$ was simulated using isotropic $|g| = 1.262$; $A = 0.0752 \text{ cm}^{-1}$ obtained from reference 380. EPR spectrum for Pr^{4+} : SrCeO_3 was simulated using anisotropic $|g_x| = 0.875$, $|g_y| = 0.790$, $|g_z| = 0.755$; $A_x = 0.0712 \text{ cm}^{-1}$, $A_y = 0.0643 \text{ cm}^{-1}$, $A_z = 0.0614 \text{ cm}^{-1}$ obtained from reference 379. Both EPR spectra were simulated using 100% ^{143}Pr nuclei with $I = 5/2$, $S = 1/2$ and frequency = 9.091 GHz (obtained from the paper). “Pepper” function in EasySpin was used and 10mT line broadening was applied to both EPR simulated spectra.

ground state of Tb^{4+} with $4f^7$ electronic configuration is predominately $^8S_{7/2}$, J manifold similar to Gd^{3+} and Eu^{2+} . When the $^8S_{7/2}$ manifold is completely populated, the expected g value (2.00232) is isotropic and close to the value of a free spin.³⁷² However, in the presence of a crystal field, the g value decreases. For a pure S ground state, the ion should not exhibit either hyperfine interaction or Stark splitting. However, in real systems, the ground state is often perturbed by mixing with excited states. EPR studies on Eu^{2+} and Gd^{3+} in different host lattices estimate a g value of 1.991.³⁷² However, EPR studies carried out by Hurrell and Baker on Tb^{4+} doped in ThO_2 single crystals reveal a g value of 2.0146, greater than the free spin value.³⁹³ The study also reveals that Tb^{4+} exhibits crystal field splitting 15 times greater than in Gd^{3+} and Eu^{2+} .³⁷² Tb^{4+} also has shorter spin lattice relaxation times than other S state ions.³⁹³ Hurrell and Baker collected $\text{Tb}^{4+}:\text{ThO}_2$ spectra at 20K. Four absorption lines were observed with sharp lines at low field and broad lines at high field due to anisotropy. Electron nuclear double resonance (ENDOR) measurements on Tb^{4+} doped ThO_2 further revealed three more transitions in the intermediate and high field region.

The Hamiltonian to best describe the Tb^{4+} spectra includes, Zeeman interactions, crystal field, and hyper fine interaction. The crystal field Hamiltonian in a cubic field is given in Equation 4. From Equation 4, the sign of $B_4 = V_4\beta$ is determined by the ratio of intensities of transitions in the high field region. For $\text{Tb}^{4+}:\text{ThO}_2$, B_4 appears to have a negative sign. However, the magnitude of B_4 is in contrast to values calculated from simple point charge models (which provide a reasonable approximation for Gd^{3+} and Eu^{2+}). The authors argue that the

unusually large value of B_4 in Tb^{4+} compared to Gd^{3+} and Eu^{2+} is indicative of covalent bonding effects.³⁷² The anomalously large g value can be explained by higher order perturbations distorting the spherical symmetry of Tb^{4+} resulting in a small anisotropy or by mixing the ${}^6P_{7/2}$ excited state into the ground state. The magnetic hyperfine coupling in Tb^{4+} was found to be significantly smaller than in Eu^{2+} and Gd^{3+} , which is indicative increased covalency in Tb^{4+} .³⁹³

The EPR spectrum of Tb^{4+} in zircon (a non-cubic crystal field) by Milne and Hutton have similar findings to the above discussion.³⁹⁴ The crystal field Hamiltonian in a non-cubic crystal field requires the use of higher order operators as shown below in Equation 8:

$$H_{CEF} = B_2O_2 + B_4O_4 + B_6O_6 + B_6^6O_6^6 \quad (8)$$

The B_2 value in the crystal field Hamiltonian determined for Tb^{4+} in zircon is 20 times greater than for Gd^{3+} in the same host lattice indicative of increased covalency. In a paper by Fielding and co-workers, hyperfine coupling to Tb ($l = 3/2$) is resolved in Tb^{4+} doped in zircon single-crystals. The hyperfine coupling is measured to be $A_{\perp} = 94.7(9)$ MHz and $A_{\parallel} = 101.2(9)$ MHz at 50 K. The authors also note the significant zero field splitting of Tb^{4+} in comparison to Gd^{3+} .³⁹⁵ Heidepreim and Ehrst observed EPR spectra for Tb^{4+} and Eu^{2+} in fluoride phosphate glasses with $g = 5.0$ for Tb^{4+} and g values of 2.0, 2.8 and 6.0 for Eu^{2+} . The difference in the spectra has been attributed to higher crystal field strength for Tb^{4+} in comparison to Eu^{2+} .³⁹⁶

Perovskites of tetravalent Tb as well as diamagnetic perovskites doped with Tb have been synthesized and studied through EPR experiments by Hinatsu. The EPR spectrum of $BaTbO_3$ shows a very broad linewidth, spanning over 1100 G. The g -value was estimated to be 2.00. Crystal field effects play a notable role the magnetic properties of tetravalent Tb . During the perovskite studies, it was noted that distortion from ideal perovskite structure, as was the case in $SrTbO_3$, resulted in a decrease in g -value from 2.00 to 1.97.¹⁵⁴ However, EPR studies by Lanzi on $SrTbO_3$ reveal a g value of 2.012, greater than the free spin value in line with the observation by Baker and Hurrell. The increased g value was again attributed to increased covalency in the $Tb-O$ bond.³⁹⁷ Lithium-rich oxides of Tb have also been studied through EPR. After doping with diamagnetic Li_8CeO_6 , a very broad line width of approximately 3000 G is observed along with a complicated structure due to hyperfine interaction with the Tb nucleus.¹³³ No g value was estimated. It should be noted here that these measurement by Hinatsu were carried out at room temperature and the observation of broad features rather than fine structure as in Tb^{4+} doped in ThO_2 can most likely be attributed to temperature effects.

All three tetravalent Tb complexes were characterized via EPR and their spectra differ significantly from those obtained in the solid-state. Spectra were collected at 4 K in toluene for **10**²⁷³ and 20 K for **14**²⁶¹ and **12**²⁶⁰ which were in Et_2O/THF and toluene, respectively. Signals for **10** were dampened at 77 K and completely attenuated at room temperature. The temperature dependence nature of the signal in the two siloxide complexes is unreported. A number of factors may contribute to the

convoluted spectra including zero field splitting, potential hyperfine coupling to the $l = +3/2$ Tb nucleus, g -strain, and rhombicity, $|D/E|$. Disentangling these contributions to provide a cohesive and detailed model requires the investigation of these complexes via high-field and frequency EPR techniques.

12. Summary

While the isolation of tetravalent Pr and Tb molecular complexes had been a long-standing challenge in coordination chemistry, these recent results are based on the considerable progress that had been made in extended solid phases and in the gas-phase to identify and characterize tetravalent lanthanide ions. These synthetic and spectroscopic results, detailed in the above sections, map out areas where further discoveries are possible and suggest areas for the development and application of advanced spectroscopies. Outstanding challenges include definitive evidence for Dy^{4+} in oxide lattices and the potential to prepare Sm^{4+} or Ho^{4+} in fluoride or oxide lattices. However, revisiting the synthetic approaches of Hoppe to prepare the A_3LnF_7 materials (condensed, pressurized F_2) is daunting. The thermochemistry and electronic structure of Pr^{4+} in oxides indicates that further unusual magnetic phenomena can be realized as synthetic chemistry is developed. Additionally, it is clear from the characterization of extant tetravalent lanthanides that the CEF is increased in comparison to their trivalent counterparts. This phenomenon is an opportunity for the application of advanced synchrotron techniques including RIXS to map higher lying crystal field states in systems that include strong neutron absorbers.³⁹⁸⁻⁴⁰⁴

Synthetic molecular chemistry has many avenues for further development. The prospect of pentavalent Pr complexes, established in gas-phase experiments, should provide significant impetus for the further exploration of the reactivity of early lanthanide coordination complexes. The evidence from in aqueous chemistry in strongly complexing solutions and the recent isolations of molecular tetravalent complexes suggest that stable Pr^{4+} and Tb^{4+} may be accessible in aqueous phases via further ligand development. This technology could have significant implications for redox-based separation processes. Additionally, the dramatic shifts in the observed the redox couples based on the coordination sphere for **7** and **9** suggest that a wealth of Pr^{4+} and Tb^{4+} coordination chemistry and reactivity is available to be explored. Given the very negative potentials accessible with the ligands developed to stabilize Tb^{4+} and Pr^{4+} , there may even be the possibility to isolate other tetravalent lanthanide ions in molecular complexes.

Synchrotron spectroscopies are an efficient and powerful tool to evaluate oxidation state in the lanthanides. However, there are a number of open questions including the physical basis of the observed multipeak feature in tetravalent spectra in L-edge and M-edge XAS spectra. The expanding coordination chemistry of these systems presents the opportunity for the application of HERFD-XANES and CASSCF methodologies to the identification of ligand parameters involved in the observed multiconfigurational behavior and other complicating physical

phenomena.^{277, 306-312} Ligand K-edge studies have demonstrated the increased covalency in tetravalent lanthanides and will remain an essential technique to evaluate bonding as synthetic chemistry expands the known analytes. The continued development of synthetic chemistry is essential to increase the number of known tetravalent analytes in pure form in the condensed phase. These analytes are essential to fully mapping the physical and chemical properties of tetravalent lanthanides, and will drive the continued development of optical, spectroscopic, magnetic, and EPR characterization methodologies to understanding the electronic structure of the tetravalent lanthanide ions.

Acknowledgements

This work was supported by the School of Chemistry and Biochemistry at the Georgia Institute of Technology and the Department of Energy, Heavy Element Chemistry Program (DE-SC0019385).

References

1. F. H. Spedding, A. F. Voigt, E. M. Gladrow and N. R. Sleight, *J. Am. Chem. Soc.*, 1947, **69**, 2777-2781.
2. F. H. Spedding, A. F. Voigt, E. M. Gladrow, N. R. Sleight, J. E. Powell, J. M. Wright, T. A. Butler and P. Figard, *J. Am. Chem. Soc.*, 1947, **69**, 2786-2792.
3. F. H. Spedding, E. I. Fulmer, T. A. Butler, E. M. Gladrow, M. Gobush, P. E. Porter, J. E. Powell and J. M. Wright, *J. Am. Chem. Soc.*, 1947, **69**, 2812-2818.
4. F. H. Spedding, E. I. Fulmer, T. A. Butler and J. E. Powell, *J. Am. Chem. Soc.*, 1950, **72**, 2349-2354.
5. F. H. Spedding, E. I. Fulmer, J. E. Powell and T. A. Butler, *J. Am. Chem. Soc.*, 1950, **72**, 2354-2361.
6. F. H. Spedding and A. H. Daane, *J. Am. Chem. Soc.*, 1952, **74**, 2783-2785.
7. F. H. Spedding, *Discuss. Faraday Soc.*, 1949, **7**, 214-231.
8. *US Pat.*, US2539282, 1951.
9. *US Pat.*, US2798789, 1957.
10. W. Klemm, *Z. Anorg. Allg. Chem.*, 1929, **184**, 345-351.
11. G. Meyer, *J. Solid State Chem.*, 2019, **270**, 324-334.
12. G. Meyer, *Angew. Chem. Int. Edit.*, 2014, **53**, 3550-3551.
13. A. Pol, T. R. M. Barends, A. Dietl, A. F. Khadem, J. Eygensteyn, M. S. M. Jetten and H. J. M. Op den Camp, *Environ. Microbiol.*, 2014, **16**, 255-264.
14. J. T. Keltjens, A. Pol, J. Reimann and H. J. M. Op den Camp, *Appl. Microbiol. Biot.*, 2014, **98**, 6163-6183.
15. N. C. Martinez-Gomez, H. N. Vu and E. Skovran, *Inorg. Chem.*, 2016, **55**, 10083-10089.
16. H. Lumpe, A. Pol, H. J. M. Op den Camp and L. J. Daumann, *Dalton Trans.*, 2018, **47**, 10463-10472.
17. L. J. Daumann, *Angew. Chem. Int. Edit.*, 2019, **58**, 12795-12802.
18. J. A. Bogart, A. J. Lewis and E. J. Schelter, *Chem-Eur J*, 2015, **21**, 1743-1748.
19. W. L. Dorfner, P. J. Carroll and E. J. Schelter, *Org. Lett.*, 2015, **17**, 1850-1853.
20. J. A. Cotruvo, *ACS Cent. Sci.*, 2019, **5**, 1496-1506.
21. L. F. Druding, J. D. Corbett and B. N. Ramsey, *Inorg. Chem.*, 1963, **2**, 869-871.
22. R. A. Sallach and J. D. Corbett, *Inorg. Chem.*, 1963, **2**, 457-459.
23. L. F. Druding and J. D. Corbett, *J. Am. Chem. Soc.*, 1959, **81**, 5512-5512.
24. J. D. Corbett and B. C. McCollum, *Inorg. Chem.*, 1966, **5**, 938-940.
25. D. A. Lokken and J. D. Corbett, *Inorg. Chem.*, 1973, **12**, 556-559.
26. U. Loechner and J. D. Corbett, *Inorg. Chem.*, 1975, **14**, 426-428.
27. G. Meyer, *Chem. Rev.*, 1988, **88**, 93-107.
28. T. Schleid and G. Meyer, *Inorg. Chim. Acta*, 1987, **140**, 113-116.
29. G. Meyer, *Prog. Solid State Ch.*, 1982, **14**, 141-219.
30. S. Hammerich, I. Pantenburg and G. Meyer, *Z. Anorg. Allg. Chem.*, 2006, **632**, 2181-2183.
31. S. Hammerich, I. Pantenburg and G. Meyer, *Z. Anorg. Allg. Chem.*, 2006, **632**, 1487-1490.
32. G. Meyer and H. J. Meyer, *Chem. Mater.*, 1992, **4**, 1157-1168.
33. C. Felser, K. Ahn, R. K. Kremer, R. Seshadri and A. Simon, *J. Solid State Chem.*, 1999, **147**, 19-25.
34. F. G. N. Cloke, *Chem. Soc. Rev.*, 1993, **22**, 17-24.
35. J. G. Brennan, F. G. N. Cloke, A. A. Sameh and A. Zalkin, *J. Chem. Soc. Chem. Comm.*, 1987, 1668-1669.
36. D. M. Anderson, F. G. N. Cloke, P. A. Cox, N. Edelstein, J. C. Green, T. Pang, A. A. Sameh and G. Shalimoff, *J. Chem. Soc. Chem. Comm.*, 1989, 53-55.
37. F. G. N. Cloke, K. Khan and R. N. Perutz, *J. Chem. Soc. Chem. Comm.*, 1991, 1372-1373.
38. P. L. Arnold, F. Geoffrey N. Cloke and P. B. Hitchcock, *Chem. Commun.*, 1997, 481-482.
39. P. L. Arnold, M. A. Petrukhina, V. E. Bochenkov, T. I. Shabatina, V. V. Zagorskii, G. B. Sergeev and F. G. N. Cloke, *J. Organomet. Chem.*, 2003, **688**, 49-55.
40. M. N. Bochkarev, I. L. Fedushkin, A. A. Fagin, T. V. Petrovskaya, J. W. Ziller, R. N. R. Broomhall-Dillard and W. J. Evans, *Angew. Chem. Int. Edit.*, 1997, **36**, 133-135.
41. W. J. Evans, N. T. Allen and J. W. Ziller, *J. Am. Chem. Soc.*, 2000, **122**, 11749-11750.
42. M. N. Bochkarev, I. L. Fedushkin, S. Dechert, A. A. Fagin and H. Schumann, *Angew. Chem. Int. Edit.*, 2001, **40**, 3176-3178.
43. M. N. Bochkarev and A. A. Fagin, *Chem-Eur J*, 1999, **5**, 2990-2992.
44. P. L. Arnold, F. Geoffrey N. Cloke and J. F. Nixon, *Chem. Commun.*, 1998, 797-798.
45. P. B. Hitchcock, M. F. Lappert, L. Maron and A. V. Protchenko, *Angew. Chem. Int. Edit.*, 2008, **47**, 1488-1491.
46. M. R. MacDonald, J. W. Ziller and W. J. Evans, *J. Am. Chem. Soc.*, 2011, **133**, 15914-15917.
47. M. R. MacDonald, J. E. Bates, J. W. Ziller, F. Furche and W. J. Evans, *J. Am. Chem. Soc.*, 2013, **135**, 9857-9868.
48. M. R. MacDonald, M. E. Fieser, J. E. Bates, J. W. Ziller, F. Furche and W. J. Evans, *J. Am. Chem. Soc.*, 2013, **135**, 13310-13313.
49. R. R. Langeslay, M. E. Fieser, J. W. Ziller, F. Furche and W. J. Evans, *Chem. Sci.*, 2015, **6**, 517-521.
50. M. E. Fieser, M. R. MacDonald, B. T. Krull, J. E. Bates, J. W. Ziller, F. Furche and W. J. Evans, *J. Am. Chem. Soc.*, 2015, **137**, 369-382.

51. K. R. Meihaus, M. E. Fieser, J. F. Corbey, W. J. Evans and J. R. Long, *J. Am. Chem. Soc.*, 2015, **137**, 9855-9860.
52. C. J. Windorff, M. R. MacDonald, K. R. Meihaus, J. W. Ziller, J. R. Long and W. J. Evans, *Chem-Eur J*, 2016, **22**, 772-782.
53. D. H. Woen, G. P. Chen, J. W. Ziller, T. J. Boyle, F. Furche and W. J. Evans, *Angew. Chem. Int. Edit.*, 2017, **56**, 2050-2053.
54. C. J. Windorff, G. P. Chen, J. N. Cross, W. J. Evans, F. Furche, A. J. Gaunt, M. T. Janicke, S. A. Kozimor and B. L. Scott, *J. Am. Chem. Soc.*, 2017, **139**, 3970-3973.
55. M. E. Fieser, M. G. Ferrier, J. Su, E. Batista, S. K. Cary, J. W. Engle, W. J. Evans, J. S. Lezama Pacheco, S. A. Kozimor, A. C. Olson, A. J. Ryan, B. W. Stein, G. L. Wagner, D. H. Woen, T. Vitova and P. Yang, *Chem. Sci.*, 2017, **8**, 6076-6091.
56. M. E. Fieser, C. T. Palumbo, H. S. La Pierre, D. P. Halter, V. K. Voora, J. W. Ziller, F. Furche, K. Meyer and W. J. Evans, *Chem. Sci.*, 2017, **8**, 7424-7433.
57. D. N. Huh, L. E. Darago, J. W. Ziller and W. J. Evans, *Inorg. Chem.*, 2018, **57**, 2096-2102.
58. A. J. Ryan, L. E. Darago, S. G. Balasubramani, G. P. Chen, J. W. Ziller, F. Furche, J. R. Long and W. J. Evans, *Chem-Eur J*, 2018, **24**, 7702-7709.
59. J. Su, C. J. Windorff, E. R. Batista, W. J. Evans, A. J. Gaunt, M. T. Janicke, S. A. Kozimor, B. L. Scott, D. H. Woen and P. Yang, *J. Am. Chem. Soc.*, 2018, **140**, 7425-7428.
60. D. H. Woen, D. N. Huh, J. W. Ziller and W. J. Evans, *Organometallics*, 2018, **37**, 3055-3063.
61. D. N. Huh, J. W. Ziller and W. J. Evans, *Inorg. Chem.*, 2018, **57**, 11809-11814.
62. C. T. Palumbo, D. P. Halter, V. K. Voora, G. P. Chen, J. W. Ziller, M. Gembicky, A. L. Rheingold, F. Furche, K. Meyer and W. J. Evans, *Inorg. Chem.*, 2018, **57**, 12876-12884.
63. T. F. Jenkins, D. H. Woen, L. N. Mohanam, J. W. Ziller, F. Furche and W. J. Evans, *Organometallics*, 2018, **37**, 3863-3873.
64. S. A. Moehring, M. J. Beltrán-Leiva, D. Páez-Hernández, R. Arratia-Pérez, J. W. Ziller and W. J. Evans, *Chem-Eur J*, 2018, **24**, 18059-18067.
65. D. N. Huh, J. W. Ziller and W. J. Evans, *Dalton Trans.*, 2018, **47**, 17285-17290.
66. A. J. Ryan, M. A. Angadol, J. W. Ziller and W. J. Evans, *Chem. Commun.*, 2019, **55**, 2325-2327.
67. M. A. Angadol, D. H. Woen, C. J. Windorff, J. W. Ziller and W. J. Evans, *Organometallics*, 2019, **38**, 1151-1158.
68. S. A. Moehring and W. J. Evans, *Chem-Eur J*, 2020, **26**, 1530-1534.
69. S. A. Moehring, M. Miehlich, C. J. Hoerger, K. Meyer, J. W. Ziller and W. J. Evans, *Inorg. Chem.*, 2020, **59**, 3207-3214.
70. H. S. La Pierre, H. Kameo, D. P. Halter, F. W. Heinemann and K. Meyer, *Angew. Chem. Int. Edit.*, 2014, **53**, 7154-7157.
71. H. S. La Pierre, A. Scheurer, F. W. Heinemann, W. Hieringer and K. Meyer, *Angew. Chem. Int. Edit.*, 2014, **53**, 7158-7162.
72. B. S. Billow, B. N. Livesay, C. C. Mokhtarzadeh, J. McCracken, M. P. Shores, J. M. Boncella and A. L. Odom, *J. Am. Chem. Soc.*, 2018, **140**, 17369-17373.
73. R. P. Kelly, L. Maron, R. Scopelliti and M. Mazzanti, *Angew. Chem. Int. Edit.*, 2017, **56**, 15663-15666.
74. C. A. Gould, K. R. McClain, J. M. Yu, T. J. Groshens, F. Furche, B. G. Harvey and J. R. Long, *J. Am. Chem. Soc.*, 2019, **141**, 12967-12973.
75. F.-S. Guo, N. Tsoureas, G.-Z. Huang, M.-L. Tong, A. Mansikkamäki and R. A. Layfield, *Angew. Chem. Int. Edit.*, 2020, **59**, 2299-2303.
76. J. D. Martin and J. D. Corbett, *Angew. Chem. Int. Edit.*, 1995, **34**, 233-235.
77. P. L. Arnold, F. G. N. Cloke, P. B. Hitchcock and J. F. Nixon, *J. Am. Chem. Soc.*, 1996, **118**, 7630-7631.
78. N. A. Piro, J. R. Robinson, P. J. Walsh and E. J. Schelter, *Coordin. Chem. Rev.*, 2014, **260**, 21-36.
79. D. Schädle and R. Anwander, *Chem. Soc. Rev.*, 2019, **48**, 5752-5805.
80. L. R. Morss, *Chem. Rev.*, 1976, **76**, 827-841.
81. S. Bratsch and H. B. Silber, *Inorg. Chim. Acta*, 1982, **65**, L53-L55.
82. E. J. Huber and C. E. Holley, *J. Am. Chem. Soc.*, 1953, **75**, 5645-5647.
83. F. B. Baker and C. E. Holley, *J. Chem. Eng. Data.*, 1968, **13**, 405-407.
84. F. A. Kuznetsov, T. N. Rezykhina and A. N. Gobulenko, *Russ. J. Phys. Chem.*, 1960, **34**, 1010.
85. F. A. Kuznetsov, V. I. Belyi, T. N. Rezykhina and Y. I. Gerasimov, *Dokl. Akad. Nauk SSSR*, 1961, **139**, 1405.
86. L. R. Morss and R. J. M. Konings, in *Binary Rare Earth Oxides*, eds. G. Adachi, N. Imanaka and Z. C. Kang, Springer Netherlands, Dordrecht, 2004, pp. 163-188.
87. R. J. M. Konings, O. Beneš, A. Kovács, D. Manara, D. Sedmidubský, L. Gorokhov, V. S. Iorish, V. Yungman, E. Shenyavskaya and E. Osina, *J. Phys. Chem. Ref. Data.*, 2014, **43**, 013101.
88. L. Eyring, H. R. Lohr and B. B. Cunningham, *J. Am. Chem. Soc.*, 1952, **74**, 1186-1190.
89. S. A. Gramsch and L. R. Morss, *J. Chem. Thermodyn.*, 1995, **27**, 551-560.
90. G. C. Fitzgibbon and C. E. Holley, *J. Chem. Eng. Data.*, 1968, **13**, 63-65.
91. C. T. Stubblefield, H. Eick and L. Eyring, *J. Am. Chem. Soc.*, 1956, **78**, 3877-3879.
92. J. K. Gibson and R. G. Haire, *J. Solid State Chem.*, 1988, **73**, 524-530.
93. J. K. Gibson and R. G. Haire, *Thermochim. Acta*, 1988, **133**, 241-246.
94. G. Beskow, *Geologiska Föreningen i Stockholm Förhandlingar*, 1924, **46**, 738-743.
95. Y. Hinatsu and Y. Doi, *J. Alloy. Compd.*, 2006, **418**, 155-160.
96. J. E. Fiscus and H.-C. zur Loye, *J. Alloy. Compd.*, 2000, **306**, 141-145.
97. Y. Hinatsu, M. Itoh and N. Edelstein, *J. Solid State Chem.*, 1997, **132**, 337-341.
98. K. Fulle, L. D. Sanjeewa, C. D. McMillen, Y. Wen, A. C. Rajamanthrilage, J. N. Anker, G. Chumanov and J. W. Kolis, *Inorg. Chem.*, 2017, **56**, 6044-6047.
99. J. D. McCullough, *J. Am. Chem. Soc.*, 1950, **72**, 1386-1390.
100. K. Momma and F. Izumi, *Journal of Applied Crystallography*, 2008, **41**, 653-658.
101. M. Hellenbrandt, *Crystallography Reviews*, 2004, **10**, 17-22.
102. S. G. Minasian, J. M. Keith, E. R. Batista, K. S. Boland, J. A. Bradley, S. R. Daly, S. A. Kozimor, W. W. Lukens, R. L.

- Martin, D. Nordlund, G. T. Seidler, D. K. Shuh, D. Sokaras, T. Tyliszczak, G. L. Wagner, T.-C. Weng and P. Yang, *J. Am. Chem. Soc.*, 2013, **135**, 1864-1871.
103. S. V. Ushakov, J. Cheng, A. Navrotsky, J. R. Wu and S. M. Haile, *MRS Proceedings*, 2002, **718**, D7.17.
104. E. H. P. Cordfunke, A. S. Booiij and M. E. Huntelaar, *J. Chem. Thermodyn.*, 1998, **30**, 437-447.
105. J. Goudiakas, R. G. Haire and J. Fuger, *J. Chem. Thermodyn.*, 1990, **22**, 577-587.
106. T. Matsui, *Thermochim. Acta*, 1995, **253**, 155-165.
107. P. Santini, S. Carretta, G. Amoretti, R. Caciuffo, N. Magnani and G. H. Lander, *Rev. Mod. Phys.*, 2009, **81**, 807-863.
108. L. Zhou, X. Li, Z. Yao, Z. Chen, M. Hong, R. Zhu, Y. Liang and J. Zhao, *Sci. Rep-UK*, 2016, **6**, 23900.
109. T. Montini, M. Melchionna, M. Monai and P. Fornasiero, *Chem. Rev.*, 2016, **116**, 5987-6041.
110. P. Xiao, R. C. Davis, X. Ouyang, J. Li, A. Thomas, S. L. Scott and J. Zhu, *Catal. Commun.*, 2014, **50**, 69-72.
111. D. C. Grinter, S. D. Senanayake and J. I. Flége, *Appl. Catal. B-Environ*, 2016, **197**, 286-298.
112. C. Ratnasamy and J. P. Wagner, *Catal. Rev.*, 2009, **51**, 325-440.
113. W. Klemm and P. Henkel, *Z. Anorg. Allg. Chem.*, 1934, **220**, 180-182.
114. H. von Wartenberg, *Z. Anorg. Allg. Chem.*, 1940, **244**, 337-347.
115. B. B. Cunningham, D. C. Feay and M. A. Rollier, *J. Am. Chem. Soc.*, 1954, **76**, 3361-3363.
116. V. I. Spitzin, L. I. Martynenko and J. U. M. Kiselew, *Z. Anorg. Allg. Chem.*, 1982, **495**, 39-51.
117. E. W. Kaiser, W. A. Sunder and W. E. Falconer, *J. Less Common Met.*, 1972, **27**, 383-387.
118. T. P. Perros and C. R. Naeser, *J. Am. Chem. Soc.*, 1952, **74**, 3694-3695.
119. A. I. Popov and G. Glockler, *J. Am. Chem. Soc.*, 1952, **74**, 1357-1358.
120. J. Soriano, M. Givon and J. Shamir, *Inorg. Nucl. Chem. Lett.*, 1966, **2**, 13-14.
121. Z. Mazej, *J. Fluorine Chem.*, 2002, **118**, 127-129.
122. G. Meyer and L. R. Morss, *Synthesis of Lanthanide and Actinide Compounds*, Springer Netherlands.
123. H. A. Pagel and P. H. M. P. Brinton, *J. Am. Chem. Soc.*, 1929, **51**, 42-54.
124. D. M. Gruen, W. C. Koehler and J. J. Katz, *J. Am. Chem. Soc.*, 1951, **73**, 1475-1479.
125. R. Wolf and R. Hoppe, *Z. Anorg. Allg. Chem.*, 1988, **556**, 97-108.
126. G. Cao, T. Yuen, P. Pernambuco-Wise, J. E. Crow, J. W. O'Reilly, M. V. Kuric, R. P. Guertin, N. Rosov and J. W. Lynn, *J. Appl. Phys.*, 1991, **70**, 6332-6334.
127. D. J. Goossens, R. A. Robinson and M. T. F. Telling, *Physica B*, 2004, **352**, 105-110.
128. B. C. Tofield, A. J. Jacobson and B. E. F. Fender, *J. Phys. C Solid State*, 1972, **5**, 2887-2895.
129. C. S. Knee, A. Magrasó, T. Norby and R. I. Smith, *J. Mater. Chem.*, 2009, **19**, 3238-3247.
130. M. Bickel, G. L. Goodman, L. Soderholm and B. Kanellakopulos, *J. Solid State Chem.*, 1988, **76**, 178-185.
131. S. Majumdar, M. R. Lees, G. Balakrishnan and D. M. Paul, *J. Phys-Condens. Mat.*, 2003, **15**, 7585-7590.
132. J. Hernández-Velasco, *J. Magn. Magn. Mater.*, 2007, **310**, 1669-1671.
133. Y. Hinatsu, *J. Solid State Chem.*, 1997, **128**, 228-232.
134. R. Wolf and R. Hoppe, *Z. Anorg. Allg. Chem.*, 1985, **522**, 39-47.
135. H. Brunn and R. Hoppe, *Z. Anorg. Allg. Chem.*, 1977, **430**, 144-154.
136. E. Paletta and R. Hoppe, *Naturwissenschaften*, 1966, **53**, 611-612.
137. H. Brunn and R. Hoppe, *Z. Anorg. Allg. Chem.*, 1977, **433**, 189-199.
138. L. B. Asprey and T. K. Keenan, *J. Inorg. Nucl. Chem.*, 1961, **16**, 260-262.
139. A. Oudahmane, M. El-Ghozzi, L. Jouffret and D. Avignant, *J. Solid State Chem.*, 2015, **232**, 73-78.
140. R. Hoppe and W. Liebe, *Z. Anorg. Allg. Chem.*, 1961, **313**, 221-227.
141. R. Hoppe, in *Inorganic Solid Fluorides*, ed. P. Hagemuller, Academic Press, 1985, pp. 275-307.
142. L. B. Asprey, J. S. Coleman and M. J. Reisfeld, in *Lanthanide/Actinide Chemistry*, American Chemical Society, 1967, vol. 71, ch. 9, pp. 122-126.
143. T. P. Perros, T. R. Munson and C. R. Naeser, *Journal of Chemical Education*, 1953, **30**, 402.
144. V. I. Spitsyn, Y. M. Kiselev, L. I. Martynenko, V. N. Prusakov and V. B. Sokolov, *Doklady Akademii Nauk SSSR*, 1974, **219**, 621-624.
145. R. Hoppe, *Angew. Chem. Int. Edit.*, 1981, **20**, 63-87.
146. S. Voigt and R. Hoppe, *J. Less Common Met.*, 1989, **156**, 97-104.
147. R. L. N. Sastry, P. N. Mehrotra and C. N. R. Rao, *J. Inorg. Nucl. Chem.*, 1966, **28**, 2167-2173.
148. M. Gasgnier, G. Schiffmacher, L. Albert, P. E. Caro, H. Dexpert, J. M. Esteva, C. Blancard and R. C. Karnatak, *J. Less Common Met.*, 1989, **156**, 59-73.
149. L. Eyring, in *Handbook on the Physics and Chemistry of Rare Earths*, Elsevier, 1979, vol. 3, pp. 337-399.
150. W. Prandtl and G. Rieder, *Z. Anorg. Allg. Chem.*, 1938, **238**, 225-235.
151. Y. Doi, K. Ninomiya, Y. Hinatsu and K. Ohoyama, *J. Phys-Condens. Mat.*, 2005, **17**, 4393-4401.
152. R. Hoppe and W. Lidecke, *Naturwissenschaften*, 1962, **49**, 255-255.
153. R. Hoppe and K. Seeger, *Naturwissenschaften*, 1968, **55**, 297-297.
154. Y. Hinatsu, *J. Solid State Chem.*, 1992, **100**, 136-140.
155. Y. Hinatsu, *J. Alloy. Compd.*, 1993, **193**, 113-115.
156. M. Guillot, M. El Ghozzi, D. Avignant and G. Ferey, *Cr. Acad. Sci. II*, 1991, **313**, 1141-1147.
157. M. Guillot, M. El-Ghozzi, D. Avignant and G. Ferey, *J. Solid State Chem.*, 1992, **97**, 400-404.
158. M. Josse, M. El-Ghozzi, D. Avignant, G. André and F. Bourée, *J. Solid State Chem.*, 2007, **180**, 1623-1635.
159. Y. Lalignant, A. Le Bail, G. Ferey, D. Avignant and J. C. Cousseins, *Eur. J. Sol. State Inorg.*, 1988, **25**, 551-563.
160. M. El-Ghozzi, D. Avignant and J. C. Cousseins, *Eur. J. Sol. State Inorg.*, 1992, **29**, 981-992.
161. M. Josse, M. El-Ghozzi, D. Avignant, G. André, F. Bourée and O. Isnard, *J. Solid State Chem.*, 2012, **185**, 229-237.
162. M. Josse, M. Dubois, M. El-Ghozzi, J. Cellier and D. Avignant, *Acta Crystallogr. B*, 2005, **61**, 1-10.

163. E. Largeau and M. El-Ghozzi, *J. Fluorine. Chem.*, 1998, **89**, 223-228.
164. M. Josse, M. El-Ghozzi, M. Dubois, D. Avignant, G. André and F. Bourée, *Physica B*, 2004, **350**, E43-E45.
165. V. Gaumet and D. Avignant, *Acta Crystallogr. C*, 1997, **53**, 1176-1178.
166. A. V. Vologzhanina, D. V. Pushkin and V. N. Serezhkin, *Russ. J. Inorg. Chem.*, 2006, **51**, 747-758.
167. M. El-Ghozzi and D. Avignant, *J. Fluorine. Chem.*, 2001, **107**, 229-233.
168. Y. Ying and Y. Ru-Dong, *Polyhedron*, 1992, **11**, 963-966.
169. R. Wolf and R. Hoppe, *Z. Anorg. Allg. Chem.*, 1986, **539**, 127-140.
170. S. Voigt, R. Werthmann and R. Hoppe, *Z. Anorg. Allg. Chem.*, 1989, **574**, 65-78.
171. S. Quezel-Ambrunaz and E. F. Bertaut, *Solid State Commun.*, 1972, **11**, 605-610.
172. J. K. Marsh, *J. Chem. Soc.*, 1946, 15-17.
173. D. Avignant, E. Largeau, V. Gaumet, P. Dugat and M. El-Ghozzi, *J. Alloy. Compd.*, 1998, **275-277**, 1-5.
174. R. Hoppe, *Angewandte Chemie*, 1959, **71**, 457-457.
175. V. Gaumet, E. Largeau and D. Avignant, *Eur. J. Sol. State Inorg.*, 1997, **34**, 1075-1084.
176. R. Hoppe and K.-M. Rödder, *Z. Anorg. Allg. Chem.*, 1961, **312**, 277-281.
177. M. Josse, M. Dubois, M. El-Ghozzi, D. Avignant, G. André, F. Bourée and M. Guillot, *J. Alloy. Compd.*, 2004, **374**, 207-212.
178. M. Guillot, M. El-Ghozzi, D. Avignant and G. Ferey, *J. Appl. Phys.*, 1993, **73**, 5389-5390.
179. J. H. Burns, H. A. Levy and O. L. Keller, *Acta. Cryst.*, 1968, **B24**, 1675.
180. J.-P. Laval and R. Mayet, *Acta Crystallogr. C*, 2018, **74**, 229-235.
181. J.-P. Laval and R. Mayet, *Acta Crystallogr. C*, 2018, **74**, 229-235.
182. E. Largeau, V. Gaumet, M. El-Ghozzi, D. Avignant and J. C. Cousseins, *J. Mater. Chem.*, 1997, **7**, 1881-1885.
183. P. Kroeschell, R. Wolf and R. Hoppe, *Z. Anorg. Allg. Chem.*, 1986, **536**, 81-91.
184. A. J. Jacobson, B. C. Tofield and B. E. F. Fender, *Acta Crystallogr. B-Stru*, 1972, **28**, 956-961.
185. E. Banks, S. J. La Placa, W. Kunmann, L. M. Corliss and J. M. Hastings, *Acta Crystallogr. B*, 1972, **28**, 3429-3430.
186. K. Tezuka, Y. Hinatsu, Y. Shimojo and Y. Morii, *J. Phys-Condens. Mat.*, 1998, **10**, 11703-11712.
187. W. T. Fu, D. Visser and D. J. W. Ijdo, *J. Solid State Chem.*, 2002, **165**, 393-396.
188. W. T. Fu, D. Visser, K. S. Knight and D. J. W. Ijdo, *J. Solid State Chem.*, 2004, **177**, 1667-1671.
189. K. S. Knight, *Solid State Ionics*, 1994, **74**, 109-117.
190. R. Horyń, M. Wołczyrz and Z. Bukowski, *J. Solid State Chem.*, 1996, **124**, 176-181.
191. E. Danielson, M. Devenney, D. M. Giaquinta, J. H. Golden, R. C. Haushalter, E. W. McFarland, D. M. Poojary, C. M. Reaves, W. H. Weinberg and X. D. Wu, *Journal of Molecular Structure*, 1998, **470**, 229-235.
192. G. Morrison, N. R. Spagnuolo, S. G. Karakalos and H.-C. zur Loye, *Inorg. Chem.*, 2019, **58**, 8702-8709.
193. Z. Hu, G. Kaindl, D. Vandr e, R. Hoppe and G. Wortmann, *J. Alloy. Compd.*, 1994, **205**, 263-269.
194. G. Brauer and H. Kristen, *Z. Anorg. Allg. Chem.*, 1980, **462**, 35-41.
195. L. Soderholm, L. R. Morss and M. F. Mohar, *J. Less Common Met.*, 1987, **127**, 131-135.
196. D. Han, T. Uda, Y. Nose, T. Okajima, H. Murata, I. Tanaka and K. Shinoda, *Adv. Mater.*, 2012, **24**, 2051-2053.
197. N. Rosov, J. W. Lynn, Q. Lin, G. Cao, J. W. O'Reilly, P. Pernambuco-Wise and J. E. Crow, *Phys. Rev. B*, 1992, **45**, 982-986.
198. S. Kern, C. K. Loong and G. H. Lander, *Phys. Rev. B*, 1985, **32**, 3051-3057.
199. A. Kebede, C. S. Jee, J. Schwegler, J. E. Crow, T. Mihalisin, G. H. Myer, R. E. Salomon, P. Schlottmann, M. V. Kuric, S. H. Bloom and R. P. Guertin, *Phys. Rev. B*, 1989, **40**, 4453-4462.
200. Y. Dalichaouch, M. S. Torikachvili, E. A. Early, B. W. Lee, C. L. Seaman, K. N. Yang, H. Zhou and M. B. Maple, *Solid State Commun.*, 1988, **65**, 1001-1006.
201. E. E. Alp, L. Soderholm, G. K. Shenoy, D. G. Hinks, B. W. Veal and P. A. Montano, *Physica B & C*, 1988, **150**, 74-79.
202. L. Soderholm and G. L. Goodman, *J. Solid State Chem.*, 1989, **81**, 121-128.
203. L. Soderholm, C. K. Loong, G. L. Goodman and B. D. Dabrowski, *Phys. Rev. B*, 1991, **43**, 7923-7935.
204. U. Staub, L. Soderholm, S. R. Wasserman, A. G. O. Conner, M. J. Kramer, B. D. Patterson, M. Shi and M. Knapp, *Phys. Rev. B*, 2000, **61**, 1548-1554.
205. S. Kern, C. K. Loong, J. Faber and G. H. Lander, *Solid State Commun.*, 1984, **49**, 295-298.
206. C. H. Gardiner, A. T. Boothroyd, P. Pattison, M. J. McKelvy, G. J. McIntyre and S. J. S. Lister, *Phys. Rev. B*, 2004, **70**, 024415.
207. C. H. Gardiner, A. T. Boothroyd, M. J. McKelvy, G. J. McIntyre and K. Prokeř, *Phys. Rev. B*, 2004, **70**, 024416.
208. C. H. Webster, L. M. Helme, A. T. Boothroyd, D. F. McMorrow, S. B. Wilkins, C. Detlefs, B. Detlefs, R. I. Bewley and M. J. McKelvy, *Phys. Rev. B*, 2007, **76**, 134419.
209. K. C. Turberfield, L. Passell, R. J. Birgeneau and E. Bucher, *J. Appl. Phys.*, 1971, **42**, 1746-1754.
210. G. Bevilacqua, D. Ippolito and L. Martinelli, *Phys. Rev. B*, 2004, **69**, 155208.
211. J. Jensen, *Phys. Rev. B*, 2007, **76**, 144428.
212. N. Magnani, P. Santini, G. Amoretti, R. Caciuffo, P. Javorsk y, F. Wastin, J. Rebizant and G. H. Lander, *Physica B*, 2005, **359-361**, 1087-1089.
213. N. Magnani, P. Santini, G. Amoretti and R. Caciuffo, *Phys. Rev. B*, 2005, **71**, 054405.
214. T. Vent-Schmidt and S. Riedel, *Inorg. Chem.*, 2015, **54**, 11114-11120.
215. T. Vent-Schmidt, Z. Fang, Z. Lee, D. Dixon and S. Riedel, *Chem-Eur J*, 2016, **22**, 2406-2416.
216. X. Wang, L. Andrews, Z. Fang, K. S. Thanthirawatte, M. Chen and D. A. Dixon, *J. Phys. Chem. A*, 2017, **121**, 1779-1796.
217. T. Mikulas, M. Chen, D. A. Dixon, K. A. Peterson, Y. Gong and L. Andrews, *Inorg. Chem.*, 2014, **53**, 446-456.
218. A. F. Lucena, C. Lourenço, M. C. Michelini, P. X. Rutkowski, J. M. Carretas, N. Zorz, L. Berthon, A. Dias, M. Conceio Oliveira, J. K. Gibson and J. Maralo, *Phys. Chem. Chem. Phys.*, 2015, **17**, 9942-9950.
219. S. P. Willson and L. Andrews, *J. Phys. Chem. A*, 1999, **103**, 3171-3183.

ARTICLE

Journal Name

220. J. Su, S. Hu, W. Huang, M. Zhou and J. Li, *Sci. China Chem.*, 2016, **59**, 442-451.
221. P. D. Dau, M. Vasiliu, K. A. Peterson, D. A. Dixon and J. K. Gibson, *Chem-Eur J*, 2017, **23**, 17369-17378.
222. B. Monteiro, N. A. G. Bandeira, C. Lourenço, A. F. Lucena, J. M. Carretas, J. K. Gibson and J. Marçalo, *Chem. Commun.*, 2019, **55**, 14139-14142.
223. A. Kovács, P. D. Dau, J. Marçalo and J. K. Gibson, *Inorg. Chem.*, 2018, **57**, 9453-9467.
224. S.-X. Hu, J. Jian, J. Su, X. Wu, J. Li and M. Zhou, *Chem. Sci.*, 2017, **8**, 4035-4043.
225. H. L. Conley, *USAEC UCRL-9332*, 1960, **46**.
226. W. M. Latimer, *Oxidation Potentials*, Prentice Hall, New Jersey, 1952.
227. L. B. Asprey and B. B. Cunningham, *Prog. Inorg. Chem.*, 1960, **2**, 267.
228. B. B. Cunningham, *Comparative Chemistry of the Lanthanide and Actinide Elements pp. 64-81*, 1959, Paper presented at the XVII International Congress of Pure and Applied Chemistry, Munich
229. L. J. Nugent, R. D. Baybarz, J. L. Burnett and J. L. Ryan, *J. Inorg. Nucl. Chem.*, 1971, **33**, 2503-2530.
230. S. Pajakoff, *Monatsh. Chem. Verw. Tl.*, 1963, **94**, 482-496.
231. N. G. Bogdanovic, N. I. Pechurova, V. I. Spitsyn and L. I. Martynenko, *Zh. Neorg. Kim.*, 1970, **15**, 2145.
232. B. F. Myasoedov, I. A. Lebedev, V. M. Mikhailiv and V. Y. Frenkel, *Radiochem. Radioanal. Lett.*, 1974, **17**, 359.
233. D. E. Hobart, PhD Thesis, University of Tennessee, 1981.
234. D. E. Hobart, K. Samhoun, J. P. Young, V. E. Norvell, G. Mamantov and J. R. Peterson, *Inorg. Nucl. Chem. Lett.*, 1980, **16**, 321-328.
235. P. G. Varlashkin, G. M. Begun and J. R. Peterson, *J. Less Common Met.*, 1985, **109**, 123-134.
236. H. D. E, S. K and P. J. R, *Radiochimica Acta*, 1982, **31**, 139-146.
237. G. F. Payne and J. R. Peterson, *J. Less Common Met.*, 1986, **126**, 371-377.
238. X. Li, W. Dong, Y. Qi, D. Wang and R. Yang, *Polyhedron*, 1991, **10**, 1479-1483.
239. X. Li and R. Yang, *Acta Chim. Sinica*, 1987, **45**, 432-438.
240. W. Dong and R. Yang, *Acta Chim. Sinica*, 1986, **44**, 563-567.
241. R. D. Yang, J. M. Liu and T. R. Ma, *Chem. J. Chin. Univ.*, 1982, **153**.
242. A. S. Saprykin, V. I. Spitsyn and N. N. Krot, *Dokl. Akad. Nauk SSSR*, 1976, **231**, 150.
243. S. M. Hua and R. D. Yang, *Chem. J. Chin. Univ.*, 1980, **573**.
244. S. R. Sofen, S. R. Cooper and K. N. Raymond, *Inorg. Chem.*, 1979, **18**, 1611-1616.
245. G. J. P. Deblonde, M. Sturzbecher-Hoehne and R. J. Abergel, *Inorg. Chem.*, 2013, **52**, 8805-8811.
246. G. J. P. Deblonde, M. Sturzbecher-Hoehne, P. B. Rupert, D. D. An, M.-C. Illy, C. Y. Ralston, J. Brabec, W. A. de Jong, R. K. Strong and R. J. Abergel, *Nat. Chem.*, 2017, **9**, 843-849.
247. G. J. P. Deblonde, A. Ricano and R. J. Abergel, *Nat. Commun.*, 2019, **10**, 2438.
248. T. A. Pham, A. B. Altman, S. C. E. Stieber, C. H. Booth, S. A. Kozimor, W. W. Lukens, D. T. Olive, T. Tyliczszak, J. Wang, S. G. Minasian and K. N. Raymond, *Inorg. Chem.*, 2016, **55**, 9989-10002.
249. L. R. Morss and J. Fuger, *J. Inorg. Nucl. Chem.*, 1981, **43**, 2059-2064.
250. J. E. Kim, J. A. Bogart, P. J. Carroll and E. J. Schelter, *Inorg. Chem.*, 2016, **55**, 775-784.
251. M. Gregson, E. Lu, D. P. Mills, F. Tuna, E. J. L. McInnes, C. Hennig, A. C. Scheinost, J. McMaster, W. Lewis, A. J. Blake, A. Kerridge and S. T. Liddle, *Nat. Commun.*, 2017, **8**, 14137.
252. W. Noh and G. S. Girolami, *Polyhedron*, 2007, **26**, 3865-3870.
253. N. M. Edelstein, P. G. Allen, J. J. Bucher, D. K. Shuh, C. D. Soffield, N. Kaltsoyannis, G. H. Maunder, M. R. Russo and A. Sella, *J. Am. Chem. Soc.*, 1996, **118**, 13115-13116.
254. M. D. Walter, C. H. Booth, W. W. Lukens and R. A. Andersen, *Organometallics*, 2009, **28**, 698-707.
255. C. Apostolidis, O. Walter, J. Vogt, P. Liebing, L. Maron and F. T. Edelman, *Angew. Chem. Int. Edit.*, 2017, **56**, 5066-5070.
256. A. Streitwieser and U. Mueller-Westerhoff, *J. Am. Chem. Soc.*, 1968, **90**, 7364-7364.
257. A. Zalkin and K. N. Raymond, *J. Am. Chem. Soc.*, 1969, **91**, 5667-5668.
258. V. Lorenz, P. Liebing, M. Böhme, A. Buchholz, W. Plass, N. Geue, L. Hilfert, S. Busse, F. Engelhardt, C. G. Hrib and F. T. Edelman, *Eur. J. Inorg. Chem.*, 2017, **2017**, 4840-4849.
259. N. T. Rice, I. A. Popov, D. R. Russo, T. P. Gomba, A. Ramanathan, J. Bacsá, E. R. Batista, P. Yang and H. S. La Pierre, *Chem. Sci.*, 2020, DOI: 10.1039/D1030SC01414A.
260. C. T. Palumbo, I. Zivkovic, R. Scopelliti and M. Mazzanti, *J. Am. Chem. Soc.*, 2019, **141**, 9827-9831.
261. A. R. Willauer, C. T. Palumbo, R. Scopelliti, I. Zivkovic, I. Douair, L. Maron and M. Mazzanti, *Angew. Chem. Int. Edit.*, 2020, **59**, 3549-3553.
262. A. R. Willauer, C. T. Palumbo, F. Fadaei-Tirani, I. Zivkovic, I. Douair, L. Maron and M. Mazzanti, *J. Am. Chem. Soc.*, 2020, **142**, 5538-5542.
263. M. K. Assefa, D.-C. Sergentu, L. A. Seaman, G. Wu, J. Autschbach and T. W. Hayton, *Inorg. Chem.*, 2019, **58**, 12654-12661.
264. E. M. Broderick, P. S. Thuy-Boun, N. Guo, C. S. Vogel, J. Sutter, J. T. Miller, K. Meyer and P. L. Diaconescu, *Inorg. Chem.*, 2011, **50**, 2870-2877.
265. J. A. Bogart, A. J. Lewis, S. A. Medling, N. A. Piro, P. J. Carroll, C. H. Booth and E. J. Schelter, *Inorg. Chem.*, 2013, **52**, 11600-11607.
266. L. A. Solola, T. Cheisson, Q. Yang, P. J. Carroll and E. J. Schelter, *Inorg. Chem.*, 2018, **57**, 10543-10547.
267. U. J. Williams, B. D. Mahoney, A. J. Lewis, P. T. DeGregorio, P. J. Carroll and E. J. Schelter, *Inorg. Chem.*, 2013, **52**, 4142-4144.
268. J. Xu, E. Radkov, M. Ziegler and K. N. Raymond, *Inorg. Chem.*, 2000, **39**, 4156-4164.
269. N. G. Connelly and W. E. Geiger, *Chem. Rev.*, 1996, **96**, 877-910.
270. J. R. Levin, W. L. Dorfner, P. J. Carroll and E. J. Schelter, *Chem. Sci.*, 2015, **6**, 6925-6934.
271. N. T. Rice, J. Su, T. P. Gomba, D. R. Russo, J. Telsler, L. Palatinus, J. Bacsá, P. Yang, E. R. Batista and H. S. La Pierre, *Inorg. Chem.*, 2019, **58**, 5289-5304.
272. R. Shannon, *Acta Crystallogr. A*, 1976, **32**, 751-767.
273. N. T. Rice, I. A. Popov, D. R. Russo, J. Bacsá, E. R. Batista, P. Yang, J. Telsler and H. S. La Pierre, *J. Am. Chem. Soc.*, 2019, **141**, 13222-13233.

274. V. A. Blatov *, *Crystallography Reviews*, 2004, **10**, 249-318.
275. V. A. Blatov, A. P. Shevchenko and V. N. Serenzhkin, *Acta Crystallogr. A*, 1995, **51**, 909-916.
276. M. W. Löble, J. M. Keith, A. B. Altman, S. C. E. Stieber, E. R. Batista, K. S. Boland, S. D. Conradson, D. L. Clark, J. Lezama Pacheco, S. A. Kozimor, R. L. Martin, S. G. Minasian, A. C. Olson, B. L. Scott, D. K. Shuh, T. Tyliczszak, M. P. Wilkerson and R. A. Zehnder, *J. Am. Chem. Soc.*, 2015, **137**, 2506-2523.
277. R. L. Halbach, G. Nocton, J. I. Amaro-Estrada, L. Maron, C. H. Booth and R. A. Andersen, *Inorg. Chem.*, 2019, **58**, 12083-12098.
278. C. H. Booth, M. D. Walter, M. Daniel, W. W. Lukens and R. A. Andersen, *Phys. Rev. Lett.*, 2005, **95**, 267202.
279. A. M. Shahin, F. Grandjean, G. J. Long and T. P. Schuman, *Chem. Mater.*, 2005, **17**, 315-321.
280. A. Kotani, K. O. Kvashnina, S. M. Butorin and P. Glatzel, *J. Electron Spectrosc.*, 2011, **184**, 210-215.
281. K. O. Kvashnina, S. M. Butorin and P. Glatzel, *Journal of Analytical Atomic Spectrometry*, 2011, **26**, 1265-1272.
282. G. Kaindl, G. K. Wertheim, G. Schmiester and E. V. Sampathkumaran, *Phys. Rev. Lett.*, 1987, **58**, 606-609.
283. A. Kotani, K. Okada and M. Okada, *Solid State Commun.*, 1987, **64**, 1479-1482.
284. G. Kaindl, G. Schmiester, E. V. Sampathkumaran and P. Wachter, *Phys. Rev. B*, 1988, **38**, 10174-10177.
285. A. Bianconi, A. Marcelli, M. Tomellini and I. Davoli, *J. Magn. Magn. Mater.*, 1985, **47-48**, 209-211.
286. A. Bianconi, A. Marcelli, H. Dexpert, R. Karnatak, A. Kotani, T. Jo and J. Petiau, *Phys. Rev. B*, 1987, **35**, 806-812.
287. T. Jo and A. Kotani, *Solid State Commun.*, 1985, **54**, 451-456.
288. D. Malterre, *Phys. Rev. B*, 1991, **43**, 1391-1398.
289. F. Grandjean, G. J. Long, R. Cortes, D. T. Morelli and G. P. Meisner, *Phys. Rev. B*, 2000, **62**, 12569-12572.
290. D. R. Modeshia, C. S. Wright, J. L. Payne, G. Sankar, S. G. Fiddy and R. I. Walton, *J. Phys. Chem. C*, 2007, **111**, 14035-14039.
291. J. P. Itié, F. Baudalet, A. Congeduti, B. Couzinet, F. Farges and A. Polian, *J. Phys-Condens. Mat.*, 2005, **17**, S883-S888.
292. Y. Takahashi, H. Sakami and M. Nomura, *Anal. Chim. Acta*, 2002, **468**, 345-354.
293. Z. Hu, G. Kaindl and B. G. Müller, *J. Alloy. Compd.*, 1997, **246**, 177-185.
294. G. Kalkowski, G. Kaindl, G. Wortmann, D. Lentz and S. Krause, *Phys. Rev. B*, 1988, **37**, 1376-1382.
295. H. Dexpert, R. C. Karnatak, J. M. Esteva, J. P. Connerade, M. Gasgnier, P. E. Caro and L. Albert, *Phys. Rev. B*, 1987, **36**, 1750-1753.
296. S. G. Minasian, E. R. Batista, C. H. Booth, D. L. Clark, J. M. Keith, S. A. Kozimor, W. W. Lukens, R. L. Martin, D. K. Shuh, S. C. E. Stieber, T. Tyliczszak and X.-d. Wen, *J. Am. Chem. Soc.*, 2017, **139**, 18052-18064.
297. Z. Hu, S. Bertram and G. Kaindl, *Phys. Rev. B*, 1994, **49**, 39-43.
298. Z. Hu, E.-J. Cho, G. Kaindl and B. G. Müller, *Phys. Rev. B*, 1995, **51**, 7514-7520.
299. R. L. Halbach, G. Nocton, C. H. Booth, L. Maron and R. A. Andersen, *Inorg. Chem.*, 2018, **57**, 7290-7298.
300. J. A. Bogart, A. J. Lewis, M. A. Boreen, H. B. Lee, S. A. Medling, P. J. Carroll, C. H. Booth and E. J. Schelter, *Inorg. Chem.*, 2015, **54**, 2830-2837.
301. J. R. Robinson, Z. Gordon, C. H. Booth, P. J. Carroll, P. J. Walsh and E. J. Schelter, *J. Am. Chem. Soc.*, 2013, **135**, 19016-19024.
302. D. E. Smiles, E. R. Batista, C. H. Booth, D. L. Clark, J. M. Keith, S. A. Kozimor, R. L. Martin, S. G. Minasian, D. K. Shuh, S. C. E. Stieber and T. Tyliczszak, *Chem. Sci.*, 2020, **11**, 2796-2809.
303. G. Ganguly, D.-C. Sergentu and J. Autschbach, *Chem-Eur J*, 2020, **26**, 1776-1788.
304. A. Kerridge and N. Kaltsoyannis, *J. Phys. Chem. A*, 2009, **113**, 8737-8745.
305. W. Liu, M. Dolg and P. Fulde, *Inorg. Chem.*, 1998, **37**, 1067-1072.
306. P. L. Arnold, K. Wang, S. J. Gray, L. M. Moreau, C. H. Booth, M. Curcio, J. A. L. Wells and A. M. Z. Slawin, *Dalton Trans.*, 2020, **49**, 877-884.
307. Y. Yu, P. Karayaylali, S. H. Nowak, L. Giordano, M. Gauthier, W. Hong, R. Kou, Q. Li, J. Vinson, T. Kroll, D. Sokaras, C.-J. Sun, N. Charles, F. Maglia, R. Jung and Y. Shao-Horn, *Chem. Mater.*, 2019, **31**, 7864-7876.
308. J. Kolorenč and K. O. Kvashnina, *MRS Advances*, 2018, **3**, 3143-3148.
309. S. M. Butorin, A. Modin, J. R. Vegelius, K. O. Kvashnina and D. K. Shuh, *J. Phys. Chem. C*, 2016, **120**, 29397-29404.
310. S. M. Butorin, K. O. Kvashnina, J. R. Vegelius, D. Meyer and D. K. Shuh, *Proceedings of the National Academy of Sciences*, 2016, **113**, 8093.
311. M. Zegke, X. Zhang, I. Pidchenko, J. A. Hlina, R. M. Lord, J. Purkis, G. S. Nichol, N. Magnani, G. Schreckenbach, T. Vitova, J. B. Love and P. L. Arnold, *Chem. Sci.*, 2019, **10**, 9740-9751.
312. T. Vitova, I. Pidchenko, D. Fellhauer, T. Pruessmann, S. Bahl, K. Dardenne, T. Yokosawa, B. Schimmelpfennig, M. Altmaier, M. Denecke, J. Rothe and H. Geckeis, *Chem. Commun.*, 2018, **54**, 12824-12827.
313. J. C. Fuggle, F. U. Hillebrecht, J. M. Esteva, R. C. Karnatak, O. Gunnarsson and K. Schönhammer, *Phys. Rev. B*, 1983, **27**, 4637-4643.
314. J. A. Bradley, K. T. Moore, M. J. Lipp, B. A. Mattern, J. I. Pacold, G. T. Seidler, P. Chow, E. Rod, Y. Xiao and W. J. Evans, *Phys. Rev. B*, 2012, **85**, 100102.
315. Z. Hu, G. Kaindl and G. Meyer, *J. Alloy. Compd.*, 1997, **246**, 186-192.
316. C. H. Lee, H. Oyanagi, C. Sekine, I. Shirovani and M. Ishii, *Phys. Rev. B*, 1999, **60**, 13253-13256.
317. D. E. Bugaris, R. Copping, T. Tyliczszak, D. K. Shuh and J. A. Ibers, *Inorg. Chem.*, 2010, **49**, 2568-2575.
318. R. A. Gordon, G. T. Seidler, T. T. Fister and K. P. Nagle, *J. Electron Spectrosc.*, 2011, **184**, 220-223.
319. J. H. Richter, B. J. Ruck, M. Simpson, F. Natali, N. O. V. Plank, M. Azeem, H. J. Trodahl, A. R. H. Preston, B. Chen, J. McNulty, K. E. Smith, A. Tadich, B. Cowie, A. Svane, M. van Schilfgarde and W. R. L. Lambrecht, *Phys. Rev. B*, 2011, **84**, 235120.
320. J. A. Bradley, K. T. Moore, G. van der Laan, J. P. Bradley and R. A. Gordon, *Phys. Rev. B*, 2011, **84**, 205105.
321. G. Kaindl, W. D. Brewer, G. Kalkowski and F. Holtzberg, *Phys. Rev. Lett.*, 1983, **51**, 2056-2059.

322. T. Manoubi, C. Colliex and P. Rez, *J. Electron Spectrosc.*, 1990, **50**, 1-18.
323. B. T. Thole, G. van der Laan, J. C. Fuggle, G. A. Sawatzky, R. C. Karnatak and J. M. Esteve, *Phys. Rev. B*, 1985, **32**, 5107-5118.
324. G. Kaindl, G. Kalkowski, W. D. Brewer, B. Perscheid and F. Holtzberg, *J. Appl. Phys.*, 1984, **55**, 1910-1915.
325. T. Jo and A. Kotani, *Phys. Rev. B*, 1988, **38**, 830-833.
326. P. Ayala, R. Kitaura, R. Nakanishi, H. Shiozawa, D. Ogawa, P. Hoffmann, H. Shinohara and T. Pichler, *Phys. Rev. B*, 2011, **83**, 085407.
327. T. Nakamura, T. Hirono, T. Kinoshita, Y. Narumi, M. Hayashi, H. Nojiri, A. Mitsuda, H. Wada, K. Kodama, K. Kindo and A. Kotani, *J. Phys. Soc. Jpn.*, 2012, **81**, 103705.
328. K. R. Meihaus, S. G. Minasian, W. W. Lukens, S. A. Kozimor, D. K. Shuh, T. Tyliczszak and J. R. Long, *J. Am. Chem. Soc.*, 2014, **136**, 6056-6068.
329. A. B. Altman, J. I. Pacold, J. Wang, W. W. Lukens and S. G. Minasian, *Dalton Trans.*, 2016, **45**, 9948-9961.
330. C. A. Hogarth and Z. T. Al-Dhhan, *Phys. Status Solidi B*, 1986, **137**, K157-K160.
331. H. E. Hoefdraad, *J. Inorg. Nucl. Chem.*, 1975, **37**, 1917-1921.
332. G. Kaindl, G. Kalkowski, W. D. Brewer, E. V. Sampathkumaran, F. Holtzberg and A. S. v. Wittenau, *J. Magn. Magn. Mater.*, 1985, **47-48**, 181-189.
333. G. Strasser and F. P. Netzer, *J. Vac. Sci. Technol. A*, 1984, **2**, 826-830.
334. E. Wuilloud, B. Delley, W. D. Schneider and Y. Baer, *Phys. Rev. Lett.*, 1984, **53**, 202-205.
335. B. Hedman, K. O. Hodgson and E. I. Solomon, *J. Am. Chem. Soc.*, 1990, **112**, 1643-1645.
336. S. E. Shadle, J. E. Penner-Hahn, H. J. Schugar, B. Hedman, K. O. Hodgson and E. I. Solomon, *J. Am. Chem. Soc.*, 1993, **115**, 767-776.
337. S. E. Shadle, B. Hedman, K. O. Hodgson and E. I. Solomon, *J. Am. Chem. Soc.*, 1995, **117**, 2259-2272.
338. T. Glaser, B. Hedman, K. O. Hodgson and E. I. Solomon, *Accounts Chem. Res.*, 2000, **33**, 859-868.
339. E. I. Solomon, B. Hedman, K. O. Hodgson, A. Dey and R. K. Szilagy, *Coordin. Chem. Rev.*, 2005, **249**, 97-129.
340. S. DeBeer George, P. Brant and E. I. Solomon, *J. Am. Chem. Soc.*, 2005, **127**, 667-674.
341. R. Sarangi, L. Yang, S. G. Winikoff, L. Gagliardi, C. J. Cramer, W. B. Tolman and E. I. Solomon, *J. Am. Chem. Soc.*, 2011, **133**, 17180-17191.
342. S. Sproules, T. Weyhermüller, R. Goddard and K. Wieghardt, *Inorg. Chem.*, 2011, **50**, 12623-12631.
343. L. Liu, C. A. Burnyeat, R. S. Lepsenyi, I. O. Nwabuko and T. L. Kelly, *Chem. Mater.*, 2013, **25**, 4206-4214.
344. M. S. Queen, B. D. Towey, K. A. Murray, B. S. Veldkamp, H. J. Byker and R. K. Szilagy, *Coordin. Chem. Rev.*, 2013, **257**, 564-578.
345. S. A. Kozimor, P. Yang, E. R. Batista, K. S. Boland, C. J. Burns, C. N. Christensen, D. L. Clark, S. D. Conradson, P. J. Hay, J. S. Lezama, R. L. Martin, D. E. Schwarz, M. P. Wilkerson and L. E. Wolfsberg, *Inorg. Chem.*, 2008, **47**, 5365-5371.
346. S. A. Kozimor, P. Yang, E. R. Batista, K. S. Boland, C. J. Burns, D. L. Clark, S. D. Conradson, R. L. Martin, M. P. Wilkerson and L. E. Wolfsberg, *J. Am. Chem. Soc.*, 2009, **131**, 12125-12136.
347. S. G. Minasian, J. M. Keith, E. R. Batista, K. S. Boland, D. L. Clark, S. D. Conradson, S. A. Kozimor, R. L. Martin, D. E. Schwarz, D. K. Shuh, G. L. Wagner, M. P. Wilkerson, L. E. Wolfsberg and P. Yang, *J. Am. Chem. Soc.*, 2012, **134**, 5586-5597.
348. S. G. Minasian, J. M. Keith, E. R. Batista, K. S. Boland, D. L. Clark, S. A. Kozimor, R. L. Martin, D. K. Shuh and T. Tyliczszak, *Chem. Sci.*, 2014, **5**, 351-359.
349. J. Suntivich, W. T. Hong, Y.-L. Lee, J. M. Rondinelli, W. Yang, J. B. Goodenough, B. Dabrowski, J. W. Freeland and Y. Shao-Horn, *J. Phys. Chem. C*, 2014, **118**, 1856-1863.
350. F. Frati, M. O. J. Y. Hunault and F. M. F. de Groot, *Chem. Rev.*, 2020.
351. R. Sarangi, S. DeBeer George, D. J. Rudd, R. K. Szilagy, X. Ribas, C. Rovira, M. Almeida, K. O. Hodgson, B. Hedman and E. I. Solomon, *J. Am. Chem. Soc.*, 2007, **129**, 2316-2326.
352. S. G. Minasian, J. M. Keith, E. R. Batista, K. S. Boland, S. A. Kozimor, R. L. Martin, D. K. Shuh, T. Tyliczszak and L. J. Vernon, *J. Am. Chem. Soc.*, 2013, **135**, 14731-14740.
353. J. T. Lukens, I. M. DiMucci, T. Kurogi, D. J. Mindiola and K. M. Lancaster, *Chem. Sci.*, 2019, **10**, 5044-5055.
354. J. N. Cross, J. Su, E. R. Batista, S. K. Cary, W. J. Evans, S. A. Kozimor, V. Mocko, B. L. Scott, B. W. Stein, C. J. Windorff and P. Yang, *J. Am. Chem. Soc.*, 2017, **139**, 8667-8677.
355. S. R. Daly, J. M. Keith, E. R. Batista, K. S. Boland, D. L. Clark, S. A. Kozimor and R. L. Martin, *J. Am. Chem. Soc.*, 2012, **134**, 14408-14422.
356. S. E. Shadle, B. Hedman, K. O. Hodgson and E. I. Solomon, *Inorg. Chem.*, 1994, **33**, 4235-4244.
357. T. Dumas, D. Guillaumont, C. Fillaux, A. Scheinost, P. Moisy, S. Petit, D. K. Shuh, T. Tyliczszak and C. D. Auwer, *Phys. Chem. Chem. Phys.*, 2016, **18**, 2887-2895.
358. C. D. Pemmaraju, R. Copping, S. Wang, M. Janousch, S. J. Teat, T. Tyliczszak, A. Canning, D. K. Shuh and D. Prendergast, *Inorg. Chem.*, 2014, **53**, 11415-11425.
359. H. M. Crosswhite, H. Crosswhite, W. T. Carnall and A. P. Paszek, *J. Chem. Phys.*, 1980, **72**, 5103-5117.
360. T. R. Cundari and W. J. Stevens, *J. Chem. Phys.*, 1993, **98**, 5555-5565.
361. G. Hong, F. Schautz and M. Dolg, *J. Am. Chem. Soc.*, 1999, **121**, 1502-1512.
362. L. Maron and O. Eisenstein, *J. Phys. Chem. A*, 2000, **104**, 7140-7143.
363. V. Vetere, P. Maldivi and C. Adamo, *J. Comput. Chem.*, 2003, **24**, 850.
364. M. Atanasov, C. Daul, H. U. Güdel, T. A. Wesolowski and M. Zbiri, *Inorg. Chem.*, 2005, **44**, 2954-2963.
365. L. Brewer, *J. Opt. Soc. Am.*, 1971, **61**, 1666-1682.
366. J. S. Parry, Cloke, S. J. Coles and M. B. Hursthouse, *J. Am. Chem. Soc.*, 1999, **121**, 6867-6871.
367. L. P. Varga and L. B. Asprey, *J. Chem. Phys.*, 1968, **49**, 4674-4679.
368. L. P. Varga and L. B. Asprey, *J. Chem. Phys.*, 1968, **48**, 139-146.
369. M. N. Popova, S. A. Klimin, S. A. Golubchik, G. Cao and J. Crow, *Phys. Lett. A*, 1996, **211**, 242-246.
370. M. N. Popova, S. A. Klimin, B. Z. Malkin, L. A. Kasatkina, G. Cao and J. Crow, *Phys. Lett. A*, 1996, **223**, 308-312.
371. W. C. Martin, L. Hagan and R. Zalubas, *Atomic energy levels—the rare-earth elements: the spectra of lanthanum, cerium, praseodymium, neodymium, promethium,*

372. samarium, europium, gadolinium, terbium, dysprosium, holmium, erbium, thulium, ytterbium, and lutetium, U.S. Dept. of Commerce, National Bureau of Standards : for sale by the Supt. of Docs., U.S. Govt. Print. Off., [Washington], 1978.
373. A. Abragam and B. Bleaney, *Electron Paramagnetic Resonance of Transition Ions*, Oxford University Press, Oxford, 1992.
374. B. Gao, T. Chen, D. W. Tam, C.-L. Huang, K. Sasmal, D. T. Adroja, F. Ye, H. Cao, G. Sala, M. B. Stone, C. Baines, J. A. T. Verezhak, H. Hu, J.-H. Chung, X. Xu, S.-W. Cheong, M. Nallaiyan, S. Spagna, M. B. Maple, A. H. Nevidomskyy, E. Morosan, G. Chen and P. Dai, *Nat. Phys.*, 2019, **15**, 1052-1057.
375. K. Kimura, S. Nakatsuji, J. J. Wen, C. Broholm, M. B. Stone, E. Nishibori and H. Sawa, *Nat. Commun.*, 2013, **4**, 1934.
376. H. A. Kramers, *Proc. Acad. Amst*, 1930, **33**.
377. S. T. Liddle, *Angew. Chem. Int. Edit.*, 2015, **54**, 8604-8641.
378. Y. Hinatsu and N. Edelstein, *J. Solid State Chem.*, 1994, **112**, 53-57.
379. Y. Hinatsu, *J. Solid State Chem.*, 1996, **122**, 384-389.
380. Y. Hinatsu and N. Edelstein, *J. Alloy. Compd.*, 1997, **250**, 400-404.
381. K. Tezuka and Y. Hinatsu, *J. Solid State Chem.*, 1999, **143**, 140-143.
382. J. Selbin, C. J. Ballhausen and D. G. Durrett, *Inorg. Chem.*, 1972, **11**, 510-515.
383. A. F. Leung and Y.-M. Poon, *Can. J. Phys.*, 1977, **55**, 937-942.
384. P. Rigny, A. J. Dianoux and P. Plurien, *J. Phys. Chem. Solids*, 1971, **32**, 1175-1180.
385. C. A. Hutchison and B. Weinstock, *J. Chem. Phys.*, 1960, **32**, 56-61.
386. J. D. Axe, H. J. Stapleton and C. D. Jeffries, *Phys. Rev.*, 1961, **121**, 1630-1637.
387. S. Stoll and A. Schweiger, *Journal of Magnetic Resonance*, 2006, **178**, 42-55.
388. Y. Hinatsu, M. Wakeshima, N. Edelstein and I. Craig, *J. Solid State Chem.*, 1999, **144**, 20-24.
389. E. A. Harris, J. H. Mellor and S. Parke, *Phys. Status Solidi B*, 1984, **122**, 757-760.
390. Y. Hinatsu, *J. Solid State Chem.*, 1997, **130**, 250-253.
391. K. Tezuka and Y. Hinatsu, *J. Solid State Chem.*, 2001, **156**, 203-206.
392. Y. Hinatsu and K. Tezuka, *J. Solid State Chem.*, 1998, **138**, 329-333.
393. Y. Hinatsu, *J. Solid State Chem.*, 1993, **102**, 362-367.
394. J. M. Baker, J. R. Chadwick, G. Garton, J. P. Hurrell and B. Bleaney, *Philos. Tr. R. Soc. S-A*, 1965, **286**, 352-365.
395. D. R. Hutton and R. J. Milne, *J. Phys. C Solid State*, 1969, **2**, 2297-2300.
396. S. Hansen, B. D. Mosel, W. Müller-Warmuth and P. E. Fielding, *Z. Naturforsch. A*, 1996, **51**, 885-894.
397. H. Ebendorff-Heidepriem and D. Ehrtr, *J. Phys-Condens. Mat.*, 1999, **11**, 7627-7634.
398. C. B. Azzoni, G. L. D. Nero and G. Lanzi, *Lettere Al Nuovo Cimento*, 1977, **19**, 369-372.
399. J. J. Gallet, J. M. Mariot, L. Journel, C. F. Hague, A. Rogalev, H. Ogasawara, A. Kotani and M. Sacchi, *Phys. Rev. B*, 1999, **60**, 14128-14131.
400. A. Amorese, O. Stockert, K. Kummer, N. B. Brookes, D.-J. Kim, Z. Fisk, M. W. Haverkort, P. Thalmeier, L. H. Tjeng and A. Severing, *Phys. Rev. B*, 2019, **100**, 241107.
401. A. Amorese, N. Caroca-Canales, S. Seiro, C. Krellner, G. Ghiringhelli, N. Brookes, D. Vyalikh, C. Geibel and K. Kummer, 2018.
402. Y.-J. Kim, J. Clancy, H. Gretarsson, G. Cao, Y. Singh, J. Kim, M. Upton, D. Casa and T. Gog, *Probing electronic excitations in iridates with resonant inelastic x-ray scattering and emission spectroscopy techniques*, 2018.
403. H. Gretarsson, J. P. Clancy, X. Liu, J. P. Hill, E. Bozin, Y. Singh, S. Manni, P. Gegenwart, J. Kim, A. H. Said, D. Casa, T. Gog, M. H. Upton, H.-S. Kim, J. Yu, V. M. Katukuri, L. Hozoi, J. van den Brink and Y.-J. Kim, *Phys. Rev. Lett.*, 2013, **110**, 076402.
404. C. Monney, K. Zhou, V. Strocov, T. Schmitt, V. Bisogni, R. Kraus and J. Geck, *Ver. Deut. Phys. Gesell.*, 2011, **1**.
405. J. Dvorak, I. Jarrige, V. Bisogni, S. Coburn and W. Leonhardt, *Rev. Sci. Instrum.*, 2016, **87**, 115109.

ARTICLE

TOC Graphic:

La	Ce	Pr	Nd	Pm*	Sm	Eu	Gd
0+ 1+	Tb	Dy		Ho	Er	Tm	Yb
2+ 3+							Lu
4+ 5+							

The thermochemistry, descriptive chemistry, spectroscopy (optical, core-level, and EPR) and physical properties of the tetravalent lanthanides (Pr, Nd, Tb and Dy) in extended phases, gas phase, solution, and as isolable molecular complexes is presented.

Author Biographies:



Natalie T. Rice received her Bachelor of Science in Chemistry from North Carolina State University. She is currently a graduate student in the La Pierre group at Georgia Institute of Technology. Her research focuses on the high-valent chemistry of lanthanide and actinide complexes.



Arun Ramanathan was born in Coimbatore, India at the foothills of the Western Ghats in 1994. He received his Bachelor's degree in Metallurgical Engineering from PSG College of Technology in 2011 and Master's degree in Materials science and Engineering at the University of Illinois Urbana Champaign in 2016. During his course of stay at UIUC, he conducted research with Professor Daniel Shoemaker. He then interned for six months at the Los Alamos National Laboratory in the LANSCE division. He is currently a graduate student in the La Pierre group at Georgia Institute of Technology. His research focuses on solid-state synthesis of lanthanide chalcogenides and the spectroscopy and magnetism of high oxidation state lanthanide materials.



Thaige P. Gompa received his Bachelor of Science in Chemical Engineering from Mississippi State University where his research was primarily focused on magnetic nanomaterials. He joined the La Pierre Group at Georgia Institute of Technology in 2016 and his research is focused on f-block coordination complexes with unique oxidation states, magnetic properties, and metal-metal interactions.



Henry, also known by his nickname, Pete, was born in St. Louis, MO. During his undergraduate studies at Harvard University, he worked with Prof. Jared Shaw at the Broad Institute on the synthesis of antibiotics and with Prof. Masahiro Murakami at Kyoto University on main group organometallics. His graduate work, with Professors John Arnold, Robert Bergman, and Dean Toste at UC-Berkeley, focused on the development of a Z-selective alkyne semihydrogenation catalyst. Following graduation, he studied ligand control of reactive low- and high-valent uranium complexes as a postdoctoral scholar with Prof. Karsten Meyer at FAU Erlangen-Nuremberg. He also worked as a Director's Postdoctoral Fellow at Los Alamos National Laboratory (LANL) with Dr. Stosh Kozimor on ligand K-edge XAS of transuranic complexes. Since 2016, he has been an assistant professor at the Georgia Institute of Technology. His group is broadly interested in the synthesis and spectroscopy of lanthanide and actinide complexes and materials.